THE UNIVERSITY OF HULL

Comparison of calculated and measured temperature fields in laser-heated thin film systems

being a Thesis submitted for the Degree of
Master of Science
in the University of Hull

by

Andrew James Clarke (BSc)

August 2017

Acknowledgements

I would like to thank both of my supervisors, Dr Chris Walton and Dr Howard Snelling, for their guidance and support throughout this work. Together we had many insightful discussions that helped to direct my research and bring it towards a conclusion. I am also grateful to Jack Eden, who I worked alongside for much of this work, for his assistance carrying out many of the laser-based experiments.

This work was conducted as part of the INFINITY project and would not have been possible without the funding from the European Union's Horizon 2020 research and innovation programme under grant agreement number 641927. I would like to acknowledge all the collaborating partners involved in the INFINITY project who I had the pleasure of working alongside. Special thanks go to Dr Thiago M. Amaral and Dr Sabine Heusing at the Leibniz Institut für Neue Materialien for their assistance with several analytical measurements and for providing the samples that were used throughout my experiments.

I would also like to thank all my friends in Hull, including everyone in the postgraduate physics office, who made my time here such an enjoyable experience. Finally, a special thanks to Cray for being so entertaining over the last year.

List of symbols

Symbol	Definition	Units
x, y, z	Cartesian coordinates	m
r, z, θ	Cylindrical coordinates	m, m, °
α	Absorption coefficient	m^{-1}
α_p	Thermal expansion coefficient	K^{-1}
A_f	Absorbed fraction	
B	Variable used in El-Adawi model	
c	Specific heat capacity	$J \cdot kg^{-1} \cdot K^{-1}$
d	Thickness	m
D	Thermal diffusivity	$m^2 \cdot s^{-1}$
ε	Emissivity	
ε_0	Permittivity of free space	$F \cdot m^{-1}$
ε_r	Relative permittivity	
$\mathbf{E}$	Electric field	$V \cdot m^{-1}$
E	Energy	J
$\dot{E}$	Rate of energy generation	W
F	Fluence	$J \cdot m^{-2}$
h	Heat transfer coefficient	$W \cdot m^{-2} \cdot K^{-1}$
I	Irradiance	$W \cdot m^{-2}$
I_0	Peak intensity of light	$W \cdot m^{-2}$
κ	Thermal conductivity	$W \cdot m^{-1} \cdot K^{-1}$
k	Imaginary part of refractive index	
L_0	Lorenz number	$W \cdot \Omega \cdot K^{-2}$
L	Plate diameter (area/perimeter)	m
L	Thermal diffusion length	m
μ	Dynamic viscosity	Pa·s
m	Mass	kg
$\bar{n}$	Complex refractive index	
n	Real part of refractive index	
$\mathbf{n}$	Surface normal vector	m

P	Beam power	W
ϕ	Volume fraction	
q''	Heat flux	$W \cdot m^{-2}$
q	Heating rate	W
Q	Rate of energy generation per unit volume	$W \cdot m^{-3}$
ρ	Density	$kg \cdot m^{-3}$
ρ	Electrical resistivity	$\Omega \cdot m$
$\mathbf{r}$	Radial vector	m
r	Radius	m
Ra_L	Rayleigh number	
R	Reflectivity	
σ_{SB}	Stefan-Boltzmann constant	$W \cdot m^{-2} \cdot K^{-4}$
τ	Pulse duration	s
t	Time	s
T_{ext}	External temperature	K
T	Temperature	K
T	Transmission	%
u	Internal energy per unit mass	$J \cdot kg^{-1}$
v	Velocity	$m \cdot s^{-1}$
ω	Angular frequency	$rad \cdot s^{-1}$

Abstract

Thermal modelling of the laser processing of nanoparticulate ITO films has been carried out with models of varying complexity. The results from a simple semi-analytical 1D model and numerical 1D, 2D and 2D-axisymmetric models are reported for continuous wave HeCd laser and nanosecond pulsed XeCl laser irradiation. These results are compared to thermal camera measurements to determine the validity of the models under the different laser regimes.

For continuous wave laser heating, it is shown that heat flow out of the laser irradiated volume significantly affects the predicted peak temperature rise. Models with fewer dimensions overestimate the temperature change, by a factor of over 100 times in the worst cases, due to the lack of lateral heat conduction. Consequently, meaningful temperatures are only calculated with 2D-axisymmetric or 3D models. When considering nanosecond pulsed lasers, the energy absorbed does not have enough time during the pulse to diffuse away from the volume in which it was deposited. Because of this, lateral heat flow is less important during heating and all the numerical models converge to the same predicted peak temperature rise. This allows much less computationally taxing models to be solved whilst obtaining the same result.

The optical properties of the film are shown to be significant in determining the rate of laser induced heating and resultant temperature rise. However, for continuous wave irradiation, the models were insensitive to changes in the thermal parameters of the film and the peak temperature is controlled by the thermal parameters of the substrate. The opposite is true for the nanosecond pulsed lasers, with the thermal parameters of the film drastically affecting the temperature rise and the substrate parameters only contributing to the cooling

which occurred over longer timescales. The differing sensitivity of the models to these parameters has been attributed to the rates of heating under the different laser regimes.

Contents

1. Introduction

Transparent conductive oxides (TCOs) are a vital component in many devices where both an electrical current is required together with the transmission of light. This includes solar cells and almost all modern display technologies which are ubiquitous throughout modern society. TCOs consist of doped metal oxides with their band gap greater than approximately 3.0 eV in order to maintain transparency in the visible region.[1] Most TCOs are n-type semiconductors, and these will be the focus of this work. The n-type doping provides free electrons within the conduction band which allows high conductivities to be achieved. It is important that the doping levels are not too high as this leads to a blue shifting of the plasma edge which could lead to absorption within the visible part of the spectrum and a loss of transparency.[1,2] Typical carrier concentrations for high performance TCOs are around 10^{20}-10^{21} cm^{-3}.[1] High electron mobilities must also be achieved in order to produce high conductivities. This can be enhanced by minimising electron scattering mechanisms within the TCO coatings. Some of the most important scattering mechanisms include grain boundary scattering, and ionised impurity scattering.[1–3] The effects of grain boundary scattering can be minimised by reducing the number of grain boundaries present by growing fewer larger grains. With regards to ionised impurity scattering, limiting the dopant concentration is important.[1,3] High concentrations of dopant atoms creates more free charge carriers but also leads to more charge scattering sites which can limit the conductivity rather than enhancing it. High dopant concentrations can also disrupt the lattice due to their different lattice parameters, size and charge density.

The most commonly used TCO material is tin-doped indium oxide (ITO) due to its superior performance over many other alternative candidates. There are some

downsides of ITO however. In particular, indium is a scarce element with limited resources that are largely controlled by the Chinese market.[4,5] This means that it is very expensive, prices can be volatile and access to the material could become limited or prohibitively expensive as the resources dwindle. Most of the indium that ends up in devices is not recycled which only exacerbates the issue; this is particularly a problem in devices that are frequently disposed of such as smartphones and other display technologies.[5] To produce high quality ITO films, sputtering is used which requires a high vacuum which is not ideal for mass-manufacture and leads to expensive start-up costs for manufacturers. Sputtering can also be problematic when working with flexible polymer substrates due to their low melting temperatures. In addition to this, the sputtering process wastes a large amount of material during deposition and an additional chemical or laser etching step is required post-deposition to pattern the ITO leading to further the material wastage.[6]

The work has been conducted as part of the INFINITY (indium-free innovative technology) project which is part of the Horizon 2020 programme. INFINITY aims to address many the concerns discussed previously by developing alternative, cheaper, more sustainable TCO materials that are compatible with solution processing on flexible polymer substrates. This would allow low cost, scalable production of TCOs using sustainable materials and by being able to print onto polymers there would be the opportunity to use these materials in flexible devices. The initial focus of this project was on ITO based systems to identify whether it was possible to create a printable ink which could be laser treated to produce TCO tracks and films on glass and polymer substrates. Such films have been printed and these will be the focus of this work with the aim of applying the outcomes to the other materials that are developed later in the project. Beyond

this, the overall aim of INFINITY is to move to TiO_2:Nb or ZnO:Si based systems which have already showed promise as viable TCO candidates.[7–21] The idea is to produce the TCO material via a sol-gel route with nanoparticles incorporated into the solution to encourage film growth with minimal film shrinkage. This should help to prevent the cracking of the film that is often experienced with sol-gel based coatings whilst producing continuous conductive pathways which can be a problem when using solely nanoparticle-based inks. However, to form the crystalline films, as required for a high conductivity, high temperature post-deposition processing of the sol-gel coatings is required. This is conventionally done in a furnace and is unfortunately not compatible with flexible polymer substrates due to their low upper working temperatures. It was proposed that by using short pulsed lasers, rapid temperature rises could be generated within the thin film coatings which could prevent substrate damage. This could allow the removal of unwanted organics from the film whilst allowing nucleation and growth processes to occur, aided by the already-crystalline nanoparticles present in the films. The substrate damage could be prevented because the upper working temperature of polymers that apply during conventional furnace treatment can be exceeded for short durations due to the rate limited nature of polymer decomposition. The substrate damage could be prevented because the upper working temperature of polymers that apply during conventional furnace treatment can be exceeded for short durations due to the rate limited nature of polymer decomposition.

The aim of this work is to investigate whether accurate temperature profiles can be predicted for different laser processes in such thin film coatings via computational modelling. The advantage of being able to validate these models is that they can then be applied to different systems where direct measurement

of the temperature is not possible; for example, this could include the use of IR lasers which could damage the sensors in thermal imaging cameras or low emissivity materials which are very difficult to accurately measure with IR thermography. It also allows the prediction of temperature rises induced by short pulsed lasers where the rate of temperature change is much faster than the response time of current IR detectors. However, the methods utilised in this work require pulse durations larger than the electron-lattice thermalisation time which is typically on the order of picoseconds.[22]

In this thesis, I will begin by giving a brief overview of the most relevant physics involved during laser heating of thin film systems is given and this is followed by a review of existing literature in this area.

The various modelling methods used within this work are then discussed including a simple semi-analytical model as well as more complex models which solve the heat diffusion equation using numerical methods. The limitations of these models are discussed and insight into the necessary level of model complexity to produce reliable predictions to guide experimental work is given.

Chapter 4 discusses the materials that were used throughout this work. The work was carried out on coatings based on an ITO based ink which was comparable to the inks under development. This consisted of ITO nanoparticles (10-50 nm) dispersed in a UV-polymerisable binder, 3-methacryloxypropy-trimethoxsilane (MPTS), and isopropoxyethanol. The purpose of the binder was to aid adhesion and film compaction. These films were dried to evaporate most of the solvent and pre-UV treated so that the binder was already polymerised, and only thermal effects were being observed. Working with such materials is a challenge from a thermal modelling perspective as none of the physical properties of the coating

are characterised and can depend on many different variables during various experimental steps required to produce the ink and deposit the coatings. Details of the optical measurements that were performed and theoretical estimations of the thermal properties of these composite films are discussed in this section alongside the substrate parameters.

The modelling work in chapter 5 initially focusses on continuous wave (CW) lasers. The validation of the models was carried out using a thermal camera alongside a HeCd laser with a wavelength of 325 nm (UV). Unfortunately, IR wavelengths which can typically produce much higher power outputs could not be used as even scattered light from such high intensity sources could damage the camera. Visible laser wavelengths were not considered as the films were designed to be transparent in this region.

This is followed by the work with a nanosecond pulsed 308 nm XeCl laser with consideration of single and multiple pulses. Attempts have been made to validate these models, but only residual temperature rises could be measured with the IR camera due to the very rapid heating and cooling rates.

Finally, concluding marks are made with regards to the accuracy of the various models under different laser heating regimes. The required accuracy of the material parameters used within the models is also discussed.

2. Background theory and literature review

Heat transport describes how thermal energy travels through materials and is locally stored. There are three main methods in which heat can be transferred in a system: conduction, convection and radiation. Depending on the type of system some of these processes will be more dominant than others.

Conduction describes the diffusion of heat within a body or between two bodies in physical contact. Classically, in gases and liquids at an atomic level this occurs via particles colliding with one another with more energetic particles transferring energy to less energetic ones. As temperature is directly related to the kinetic energy of a system this results in a change in the temperature distribution. In a solid, atoms are held closely packed together in a lattice and rather than colliding into one another, heat is transferred via lattice vibrations or, in good conductors, via electronic motion through the solid. The conduction of heat can be described by Fourier's law (Equation 1) where q'' is the heat flux, κ, is the thermal conductivity and T the temperature.

$$q'' = -\kappa \nabla T \tag{1}$$

The derivation of the following equations is based on the approach used Incropera et al.[23] The heating rate, q, (units W) is defined by the heat flux multiplied by the area through which the heat is transferred. The heating rates into an infinitesimally small volume element (figure 1) are therefore defined by equation 2.

$$\begin{aligned} q_x &= q''_x \, dy \, dz \\ q_y &= q''_y \, dx \, dz \\ q_z &= q''_z \, dx \, dy \end{aligned} \tag{2}$$

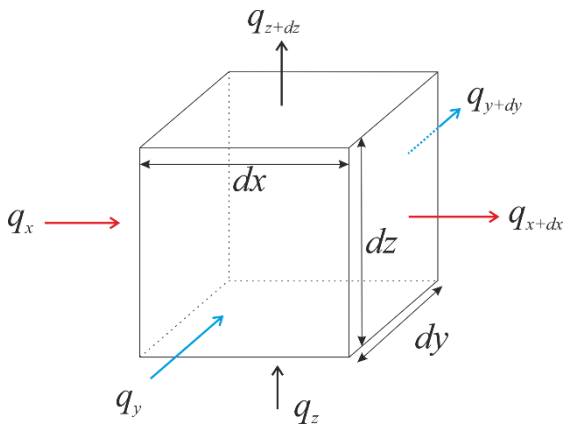

Figure 1 – total heat flow in and out of unit volume $dV=dx\cdot dy\cdot dz$.

By using a Taylor expansion and neglecting higher order terms, it is possible to write all the outward heating rates in terms of the inward heating rates and their derivatives.

$$\begin{aligned} q_{x+dx} &= q_x + \frac{\partial q_x}{\partial x}\cdot dx \\ q_{y+dy} &= q_y + \frac{\partial q_y}{\partial y}\cdot dy \\ q_{z+dz} &= q_z + \frac{\partial q_z}{\partial z}\cdot dz \end{aligned} \tag{3}$$

The net flow of energy in each direction is equal to the inward minus the outward heat flow. If this is applied to all three directions, then the combined net flow of energy into the system is given by equation 4.

$$q_{net} = -\left(\frac{\partial q_x}{\partial x}\cdot dx + \frac{\partial q_y}{\partial y}\cdot dy + \frac{\partial q_z}{\partial z}\cdot dz\right) \tag{4}$$

As well as energy flowing into and out of the system, the system may itself be generating heat, so this must also be considered. The rate of heat generated inside the system is described by equation 5 where Q is the rate of energy generation per unit volume.

$$\dot{E}_{gen} = Q\,dx\,dy\,dz \tag{5}$$

Considering the energy balance, the rate of energy accumulation is equal to the flow of energy into the volume, minus the flow of energy leaving plus the rate of any energy generation within the volume (equation 6). The rate of change in the internal energy per unit mass, $\partial u/\partial t$, is equal to the specific heat capacity multiplied by the rate of change in temperature (equation 7). This can be used to calculate the rate of energy that is being stored in the system, $\dot{E}_{st}$, assuming no phase changes occur.

$$\dot{E}_{st} = \dot{E}_{in} - \dot{E}_{out} + \dot{E}_{gen} \tag{6}$$

$$\frac{\partial u}{\partial t} = c\frac{\partial T}{\partial t} \tag{7}$$

$$m = \rho\, dx\, dy\, dz \tag{8}$$

$$\dot{E}_{st} = m\frac{du}{dt} = m\,c\frac{\partial T}{\partial t} = \rho\, c\frac{\partial T}{\partial t}\, dx\, dy\, dz \tag{9}$$

As $\dot{E}_{in}$-$\dot{E}_{out}$ is defined by equation 4, equations 4, 5 and 9 can be substituted into equation 6 which leads to

$$\dot{E}_{st} = \rho\, c\frac{\partial T}{\partial t}\, dx\, dy\, dz = -\left(\frac{\partial q_x}{\partial x}\cdot dx + \frac{\partial q_y}{\partial y}\cdot dy + \frac{\partial q_z}{\partial z}\cdot dz\right) + Q\, dx\, dy\, dz \tag{10}$$

By applying Fourier's law, the heating rates can be written in terms of temperature gradients.

$$\begin{aligned} q_x &= -\kappa\,(dy\, dz)\frac{\partial T}{\partial x} \\ q_y &= -\kappa\,(dx\, dz)\frac{\partial T}{\partial y} \\ q_z &= -\kappa\,(dx\, dy)\frac{\partial T}{\partial z} \end{aligned} \tag{11}$$

Then by substitution of these terms (11) into equation 10 it follows that

$$\rho\, c\frac{\partial T}{\partial t}\, dx\, dy\, dz = \kappa\, dx\, dy\, dz\left(\frac{\partial^2 T}{\partial x^2} + \frac{\partial^2 T}{\partial y^2} + \frac{\partial^2 T}{\partial z^2}\right) + Q\, dx\, dy\, dz \tag{12}$$

This can be simplified by dividing all the terms by the volume of the control volume ($dx \cdot dy \cdot dz$) to give the heat diffusion equation (13).

$$\rho c \frac{\partial T}{\partial t} = \nabla \cdot (\kappa \nabla T) + Q \tag{13}$$

This equation describes the conduction of heat through materials and by solving this equation, the spatial and temporal temperature profile that results from a volumetric heat source, Q, can be calculated.

As well as conduction, other methods of heat transfer are also important to model heating and cooling realistically. Convection is a method of heat transfer which occurs in gases and liquids. When cool particles of liquid or gas flow past a warm body, energy is transported from the warm body to the fluid via collisions between the two materials. This increases the temperature of the fluid and cools the warm body. As the fluid flows away, it carries the heat with it. Such fluid flow can occur via natural convection or forced convection. Natural convection arises due to the inhomogeneity of the density caused by the temperature gradients within the fluid. The air around a warm object will increase in temperature and, in the case of air and most other fluids, will become less dense. Due to gravity, buoyant forces then act upon this less dense air, forcing it upwards with cooler, more dense air, filling the space. This cooler air will then heat up – cooling the hot object in the process as previously and the cycle continues generating convection currents which transport heat away from the hot object via particle motion. Forced convection is different in that an external source is used to force the flow of fluid past the hot object rather than allowing it to happen naturally. For example, running water over the system or using a nozzle to pass air over the hot object.

Newton suggested a simple law to describe the effects of cooling given by equation 14 where T_{ext} is the external temperature away from the warm object and h is a heat transfer coefficient.[23–25]

$$q'' = h\left(T - T_{ext}\right) \tag{14}$$

Heat transfer coefficients for various types of surfaces and different orientations have been derived to describe convective losses. For the upper surface of a horizontal plate these are given by equations 15 for $T>T_{ext}$ and 16 for $T\leq T_{ext}$.[23,24,26] For a downward-facing surface they are used the opposite way round.[23,24,26]

$$h = \begin{cases} 0.54\dfrac{\kappa}{L}Ra_L^{1/4} & if \quad 10^4 \leq Ra_L \leq 10^7 \\ 0.15\dfrac{\kappa}{L}Ra_L^{1/3} & if \quad 10^7 \leq Ra_L \leq 10^{11} \end{cases} \tag{15}$$

$$h = 0.27\frac{\kappa}{L}Ra_L^{1/4} \quad if \quad 10^5 \leq Ra_L \leq 10^{10} \tag{16}$$

In these equations, κ is the thermal conductivity of the fluid and L is the “plate diameter” (defined as area/perimeter).[24,26] Equation 17 describes the Rayleigh number Ra_L where g is the acceleration due to gravity, α_p is the thermal expansion coefficient and μ is the dynamic viscosity. Temperature dependent material parameters within these calculations are calculated at the mean temperature between the boundary and the external temperature.[24,26]

$$Ra_L = g\frac{\alpha_p \rho^2 c_p \left|T - T_{ext}\right| L^3}{\kappa \mu} \tag{17}$$

This type of boundary condition is an approximation of the process of convection and depending on the convective process an exponent is sometimes necessary on the temperature difference term.[25] In order to explicitly model the effects of convection, mass transfer must be considered. For forced convection (advection) this can be done by adding an additional term into equation 13 to describe the

velocity of the fluid and thus the transport of heat.[25] However, when natural convection is occurring the velocity field within the fluid is unknown and must be calculated via fluid flow simulations which can be coupled with the heat transfer simulation to accurately calculate the temperature distribution and the heat transfer via both conduction and convection. However, this is very computationally taxing and was deemed to be beyond the scope of this project.

All objects above 0 K emit radiation in the form of electromagnetic waves, often called thermal radiation. Due to the conservation of energy, if this radiation is being emitted by an object its temperature will decrease as energy is being transported away. The radiation emitted by a hot object occurs across a distribution of wavelengths with the peak of this distribution dependent on the temperature as described by Wien's displacement law. The total radiated power per unit area across all wavelengths, e, is described by the modified Stefan-Boltzmann law (equation 18).

$$e = \varepsilon \sigma_{SB} T^4 \tag{18}$$

For an ideal surface, the emissivity, ε, is 1, as assumed by the unmodified Stefan-Boltzmann law, however real surfaces do not behave as a perfect blackbody, so the emissivity is used to correct for this. Assuming that none of the emitted radiation is reabsorbed by another object in the system of interest, the heat flux away from a surface can be described by equation 19.[23]

$$q'' = \varepsilon \sigma_{SB} (T^4 - T_{ext}^4) \tag{19}$$

As well as heat transport, it is also important to consider how heat sources are described. As the focus of this work is on laser processing, we need to be able to describe the heat generated via the interaction between the laser light and materials. The complex refractive index allows the surface reflectivity and optical

penetration depth to be calculated. It also allows the heat source that is generated by the absorbed laser light to be calculated via equation 20 assuming all the absorbed light decays non-radiatively. In this equation, α is the absorption coefficient (defined by equation 21) and I is the irradiance of the beam.

$$Q = \alpha I \tag{20}$$

$$\alpha = \frac{4\pi k}{\lambda} \tag{21}$$

To do this, the loss during beam propagation is described by the Beer Lambert law to account for the absorption and multiple reflection losses are considered within the film (equation 22). [See erratum at the end of Appendix A for correction of equation 22.] R_1 is the reflectivity between the air and film and R_2 is the reflectivity between the film and substrate according to the normal incidence Fresnel reflection (equation 23). The film thickness is given by d_f, the absorption coefficients of the film and substrate by α_f and α_s respectively and the incident intensity by I_0. The substrate absorption term is described by equation 24 where multiple reflections are not considered to be important. [See erratum at the end of Appendix A for correction of equation 24.] These equations do not consider the effects of interference as this was determined to be unnecessary due to the well-matched refractive indices between the film and substrate that were required for a high transparency coating. The matched indices led to low reflectivities and minimal interference effects. The derivation of these equations is shown in Appendix A.

$$I_f(z) = I_0(1-R_1)\exp(-\alpha_f z)\left(\frac{\exp(3\alpha_f d_f)+R_2\exp(2\alpha_f z)}{\exp(3\alpha_f d_f)+R_1 R_2}\right) \tag{22}$$

$$R = \left| \frac{\bar{n}_1 - \bar{n}_2}{\bar{n}_1 + \bar{n}_2} \right|^2 \tag{23}$$

$$I_s(z) = I_0 \frac{(1-R_1)(1-R_2)\exp(-\alpha_f d_f)}{1-R_1 R_2 \exp(-3\alpha_f d_f)} \exp(-\alpha_s (z - d_f)) \tag{24}$$

To use these equations, the peak intensity of the beam in space and time must be calculated. For a continuous wave laser, typically the total power of the beam is known whereas for pulsed lasers, this is usually the energy per pulse. The expressions for the peak intensity for each type of laser are given by equations 25 and 26 respectively where *f(x,y)* describes the spatial intensity profile and *g(t)* describes the temporal intensity profile of a single pulse, both normalised to 1. P describes the beam power and E describes the energy of the laser pulse. The surface integrals are carried out over the area of the beam.

$$I_0 = \frac{P}{\int_S f(x,y)\, dS} \tag{25}$$

$$I_0 = \frac{E}{\int_S f(x,y)\, dS} \frac{1}{\int_0^\infty g(t)\, dt} \tag{26}$$

For a general laser, the heat source would be described by equation 27 with *h(z)* given by equation 22 or 24 for the film/substrate respectively (the peak intensity is incorporated in the *h(z)* term). The *h(z)* term describes the laser intensity in the direction of beam propagation.

$$Q = \alpha(z)\, f(x,y)\, g(t)\, h(z) \tag{27}$$

Alongside volumetric loads to describe the heat source, boundary conditions are also required to solve equation 13. There are two main types of boundary condition that are used in these problems, the Dirichlet and Neumann conditions. For a general partial differential equation (PDE) that is being solved for T, these

conditions are given by equations 28 and 29 respectively where $\mathbf{r}$ is the radial vector along the boundary, t is time, and n is the direction normal to the boundary.

$$T = f(\mathbf{r}, t) \tag{28}$$

$$\frac{\partial T}{\partial n} = f(\mathbf{r}, t) \tag{29}$$

The Dirichlet boundary condition is typically used in thermal modelling to set a boundary at a fixed temperature. The Neumann condition is used to define the heat flux at a boundary and can be used in several ways including to apply boundary heat sources, to define thermally insulated boundaries and for radiative cooling and to apply Newton's law of cooling.

By bringing all of this together, it is possible to build a set of mathematical equations which describe the situation that we wish to model. These equations can then be solved to calculate the temperature in space and time of the objects that are being modelled. Much research has been carried out in this area in the past and it continues to this day as heat transfer is vital for many different applications.

Some of the earliest work modelling laser heating began just after the development of the first laser systems and was largely focussed on analytical solutions to the heat equation. All the models rely on solving the heat diffusion equation, the simplest of which make many different assumptions about the sample geometry, optical properties, thermal properties or laser parameters. As the models increase in complexity, some of these assumptions are relaxed. Many of the simpler solutions and others have conveniently been collated in the works of several authors with descriptions of the different conditions in which they are valid and the assumptions that have been made.[27–29]

Prior to the development of the first lasers, Carslaw and Jaeger published many different solutions to the heat equation.[30] These solutions were later applied to laser heating by numerous authors. However, in many cases the solutions presented by Carslaw and Jaeger were still in integral form which required further evaluation either analytically or numerically to evaluate the temperature rise.

Some of the earliest models specific to laser heating were reported by J. F. Ready in the mid-1960s to the early-1970s.[31,32] He provided solutions for three different situations of conduction within a semi-infinite solid which was subject to uniform irradiation across the solid surface.[27,31] The first case described a surface heat source with an irradiance that was constant in time either in the form of continuous irradiation or a rectangular pulse. The second case was similar but included a distributed heat source rather than a surface heat source. The final case gave a solution for a surface heat source with a time dependent irradiance term. Ready also provided solutions to the heat equation for a finite sized Gaussian beam with a surface heat source in a semi-infinite solid with a varying intensity in time.[27,31]

In 1975, Bechtel published details of various solutions to the heat equation within a semi-infinite solid with either surface or volumetric absorption for continuous lasers and pulsed lasers.[33] Many of the general solutions were provided in integral form with a few cases evaluated to produce a complete analytical solution. For the volumetric heat source, the complete analytical form reduced the problem down to a 1D heat flow with uniform spatial irradiation across the sample and a rectangular pulse in time. However, for the case of surface absorption, an analytical solution was given for a spatial and temporal laser pulse which were both Gaussian. The integral expressions were still useful but often required numerical methods to evaluate them.

Two years later, Lax published an analytical solution to the heat diffusion equation for a Gaussian beam with a distributed heat source.[34] More general equations involving integrals were also provided so that other beam shapes could be considered. This solution provided the temperature as a function of time, depth and the radial coordinate within a semi-infinite solid. This was followed by a solution which incorporated a temperature dependent thermal conductivity which was necessary for the modelling of semiconductor laser annealing.[35]

Moving away from the assumption of a semi-infinite substrate where much of the work had been focussed, several authors had considered laser heating of samples consisting of multiple layers of different materials. The earliest solutions of multilayer systems were once again produced prior to the development of lasers with many more laser specific solutions derived in the 1960s and 1970s; several of these early models have been discussed by Duley.[27]

In 1995, El-Adawi et al. published a semi-analytical solution to the heat diffusion equation for a two-layer system of a thin film on a semi-infinite substrate.[36] This was a 1D model and assumed a surface absorption but provided a solution that was relatively easy to evaluate with a computer.

However, by this point computers became more powerful and numerical techniques were being developed which utilised these new technological advancements and it became increasingly less important that an analytical or semi-analytical solution could be reached. Numerical techniques allowed the heat diffusion equation to be solved with fewer assumptions being required meaning the predicted temporal and spatial profiles would better converge to those inferred by experiments. These methods included finite difference and finite element methods and are now commonplace in the analysis of heat transfer. They allow

the effects of radiative and convective losses to be considered without the mathematical complexity that they produce when trying to reach an analytical solution. Temperature dependent parameters can easily be incorporated, and laser pulses of any spatial and temporal shape can be defined. However, despite all these benefits, the major disadvantage of numerical models is that even with the huge advancement in computing power, they can still be very resource hungry and time consuming. Depending on the situation being modelled it may also turn out that an analytical solution to a problem would suffice and could provide just as much insight into a problem in a considerably shorter time.

3. Different approaches to thermal modelling

3.1. Semi-analytical model (1D)

In this work, an ideal computational model would accurately predict the thermal response of the thin film system to laser irradiation whilst having the lowest possible computational requirements. Low computational requirements are highly advantageous as they could allow for rapid screening and optimisation of the laser heating process. Whereas if the models have high computational requirements, their implementation may be both costly and time consuming which would ultimately limit their applications.

Hence, as a starting point for the thermal modelling, a simple case was considered first. A model was sought which accurately described a sample consisting of a thin film on a substrate and made as few assumptions as possible whilst still having a short computation time. It was decided to investigate the semi-analytical solution published by El-Adawi et al.[36] This model describes a two layer system of a thin film, thickness d, on a semi-infinite substrate. The absorbed laser radiation is considered as a surface heat flux at the upper surface of the thin film and multiple reflections are not included. The losses from radiation and convection are neglected and all material parameters are assumed to be temperature independent.

The initial conditions define the initial temperature of the whole sample as 0 and are described by equations 30 and 31. Although along the same axis, distances through the film are given the coordinate, x, and those through the substrate are labelled z.

$$T_f(x, t=0) = 0 \tag{30}$$

$$T_s(z, t=0) = 0 \tag{31}$$

The rate at which energy flows into the film due to the laser source is described by equation 32 where A_f describes the absorbed fraction of laser light and q''_0 is the incident irradiance ($W \cdot m^{-2}$).

$$q''_0 A_f = -k_f \frac{\partial T_f}{\partial x} \tag{32}$$

At the film-substrate interface, the boundary conditions described by equations 33 and 34 are applied.

$$T_f(x = d, t) = T_s(z = 0, t) \tag{33}$$

$$-\kappa_f \frac{\partial T_f(x = d, t)}{\partial x} = -\kappa_s \frac{\partial T_s(z = 0, t)}{\partial z} \tag{34}$$

Finally, for the substrate,

$$T_s(z = \infty, t) = 0 \tag{35}$$

A schematic showing these boundary conditions is shown in figure 2.

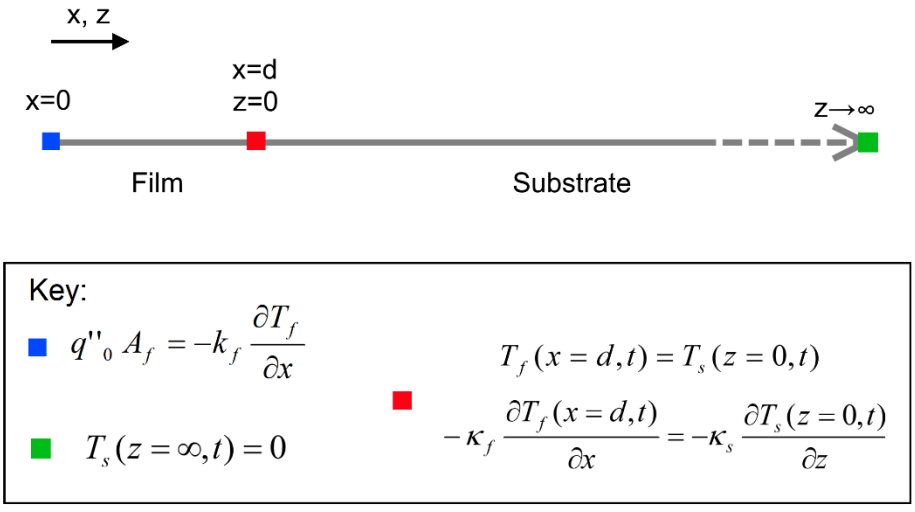

Figure 2 – Schematic showing sample geometry and boundary conditions within the El-Adawi laser heating model.

The details of how this was solved can be found in the paper by El-Adawi et al. but are not described here.[36] The resultant temperature profiles for the film and substrate are given by equations 36 and 37 respectively. Although technically for these to produce the exact solution, the sum to infinity is required, convergence was found after 10 terms which greatly reduced the computation time (typically to a few seconds).

$$\begin{aligned} T_f(x,t) = & \sum_{n=0}^{\infty} \frac{q''_0 A_f}{\kappa_f} B^{n+1} \left(\sqrt{4 D_f t / \pi} \times \exp\left(- \frac{(2d(1+n)-x)^2}{4 D_f t} \right) \right. \\ & \left. - (2d(1+n)-x) \times erfc\left(\frac{2d(1+n)-x}{\sqrt{4 D_f t}} \right) \right) \\ & + \sum_{n=0}^{\infty} \frac{q''_0 A_f}{\kappa_f} B^{n} \left(\sqrt{\frac{4 D_f t}{\pi}} \exp\left(- \frac{(2nd+x)^2}{4 D_f t} \right) \right. \\ & \left. - (2nd+x) \times erfc\left(\frac{2nd+x}{\sqrt{4 D_f t}} \right) \right) \end{aligned} \tag{36}$$

$$\begin{aligned} T_s(z,t) = & \sum_{n=0}^{\infty} \frac{2 q''_0 A_f}{\kappa_f} \frac{B^n}{(1+\varepsilon)} \left(\sqrt{\frac{4 D_t t}{\pi}} \exp\left(- \frac{\left(z\sqrt{D_f / D_s} + (1+2n)d\right)^2}{4 D_f t} \right) \right. \\ & \left. - \left(z\sqrt{D_f / D_s} + (1+2n)d\right) \times erfc\left(\frac{z\sqrt{D_f / D_s} + (1+2n)d}{\sqrt{4 D_f t}} \right) \right) \end{aligned} \tag{37}$$

B is defined by equation 38 where κ is the thermal conductivity and D is the thermal diffusivity with the subscripts indicating either the film or substrate.

$$B = \frac{1 - \dfrac{\kappa_s \sqrt{D_f}}{\kappa_f \sqrt{D_s}}}{1 + \dfrac{\kappa_s \sqrt{D_f}}{\kappa_f \sqrt{D_s}}} \tag{38}$$

These equations provide the temperature profile for continuous irradiation, but a rectangular pulse can be simulated by subtracting a second solution that is displaced in time by an amount equal to the pulse duration, τ.

For continuous irradiation, the temperature profile as a function of space and time is given by equation 39.

$$T(x,t) = \begin{matrix} If\ x \le d & T_f(x,t) \\ If\ x > d & T_s(x,t) \end{matrix} \tag{39}$$

For pulsed irradiation it is given by equation 40 where $T(x,t)$ and $T(x,t-\tau)$ refer to equation 39.

$$T(x,t,\tau) = \begin{matrix} If\ t \le \tau & T(x,t) \\ If\ t > \tau & T(x,t) - T(x,t-\tau) \end{matrix} \tag{40}$$

There are some obvious limitations with this model, in particular that it assumes that all the laser energy is absorbed at the surface. This simplification is only truly valid if the absorption coefficient at the laser wavelength is such that the incident radiation is absorbed in a layer that is thin compared to the film thickness which is not satisfied in many cases. As this is a 1D model, different beam shapes and moving beams cannot be simulated and heat transfer in the plane of the film/substrate is not considered. There are also no other loss mechanisms other than heat transfer via conduction into the substrate due to the extra complications that it would introduce when trying to reach an exact solution. This means that over long timescales where there is enough time for the sample to cool, the solution may become inaccurate. The advantages of this method however are that it is extremely fast to compute a result. However, the assumptions are only valid for short duration, large area uniform beams which are being absorbed very strongly by the film.

3.2. Finite element models (1D, 2D & 3D)

To address some of the limitations of the analytical models, numerical simulations were used to solve the heat diffusion equation (equation 13). They have the advantage that they do not require an exact solution which means that more complex situations can be considered where it would not always be possible to obtain an algebraic solution to the problem. With these models, temperature dependent parameters can be considered as well as different temporal pulse shapes. It is also possible to simulate more layers, which is important when we would like to include the surrounding ambient air which will affect the cooling rate of the system. We are also no longer limited to surface absorption and can use more realistic volumetric heat sources. However, numerical solutions typically take more time to provide a solution as iterative processes must often be used.

The numerical method that was used is known as the finite element method. The finite element method is a powerful numerical technique that can be used to solve problems involving partial differential equations. A detailed description of how this method can be applied to many problems is beyond the scope of this thesis but is covered in many texts.[37–40] Here, we will give a brief overview (based on the work of Burnett[37]) to explain the features salient to this work.

The first step of the finite element method is to define the system of interest and the equations that describe the problem. Next, the whole system being modelled is split up into domains which correspond to the different materials within the system. Then these domains are meshed. This consists of further dividing the domains into subdomains known as elements. The shape of these elements can vary depending on the problem, but quadrilateral and triangular elements are common in 2D and tetrahedra, pentahedra and hexahedra are common in 3D

models. Within each element the governing equations of the model in their variational form are transformed into algebraic equations which approximate the full governing equation (utilising integral approximations). This is done as it is much easier computationally to solve algebraic equations than calculus equations. These equations are typically identical for all elements of the same type. These algebraic equations are then evaluated for each element and the results are assembled into a set consisting of many algebraic equations, called system equations. These equations are written in matrix form and a very sparse matrix results which requires significantly less computational resources to solve as only the values around the diagonal are non-zero. This considers any volumetric loads, such as a volumetric heat source, but the boundary conditions still must be satisfied. These are applied using quite simple operations which add values to or rearrange existing equations. This system of equations is then solved using numerical evaluation techniques. There are many different techniques that can be used, and this is something that should be considered if writing code to perform this as different techniques are more effective for different problems. However, these are typically automatically decided by the program when using commercially available software. Once this is complete, the solution has been reached and can be displayed in graphical or numerical form.

As the finite element method only produces approximate solutions it is important that we are sure that the solution is correct as erroneous results may be produced if the model is poorly designed. If the equations used, correctly describe the physical system, the main factors that affect the accuracy of the solutions are the meshing and time stepping. In areas of rapid change in the dependent variable that is being solved for, it is important that the meshing is fine to be able to accurately follow these variations. Similarly, in areas where the volumetric loads

are being described, such as heat sources in thermal modelling, if these vary over the domains, the meshing must be fine enough to resolve this. There is no set practice on what makes an acceptable mesh and there will be an infinite number of different acceptable meshes. So, to determine if the mesh is good enough trial and error can be used by reducing the mesh size until no significant difference within the solution is observed. It is also good practice to have an idea of what the solution should look like so that any obvious issues with the solution are noticed. The case is similar with time stepping, especially with time dependent loads. Around rapid changes in the load, or for moving sources, small steps should be taken so that no large jumps occur. The acceptability of the time steps can once again be determined by trial and error, creating smaller time steps until the solution no longer significantly differs.

The finite element method in this work was implemented by the commercially available software COMSOL.[41] The final models were all run on version 5.2a. The default solver settings were used for all models for time-dependent heat transfer studies except for the time stepping which was set to “strict”. This forces the program to solve at each of the manually defined individual time steps with the solver taking any necessary intermediate steps. A triangular mesh was used in 2D models.

In all the finite element models in this work the boundary conditions that are applied are the same throughout unless explicitly stated otherwise. Neumann boundary conditions were applied on the upper film surface and lower substrate surface to define the heat flux due to radiative losses (equation 19) and convective losses (equation 14). Further Neumann boundary conditions were applied at the outer boundaries to define zero heat flux at these points. Where possible for large samples where the whole volume is not being modelled, it is

important to ensure that these boundaries are far enough away that the generated heat cannot travel to these boundaries within the modelled time. This distance is typically determined using the characteristic thermal diffusion length given by equation 41 where D is the thermal diffusivity and t is the time, given as the total time the model is computing for.

$$L = \sqrt{Dt} = \sqrt{\frac{\kappa}{\rho c} t} \tag{41}$$

When using temperature dependent variables, it is also important to consider how this will affect the diffusion length. To ensure that the assumption that the thermally insulated (or fixed temperature) boundary conditions are still valid (being far enough away from the heat flow), L, should be maximised by picking the extreme values for κ, ρ, c that produce the largest value of L. It turned out that this was not necessary as it was possible to model the whole sample.

Volumetric heat sources, as defined by equation 27, were used throughout. Material properties were defined by temperature dependent values where possible unless explicitly stated otherwise.

There were three models that were used: 1D, 2D and 2D-axisymmetric. In the 1D model, a semi-infinite system is being considered which is being irradiated with a uniform intensity beam because of the lack of lateral heat flow in all directions. In the 2D case, lateral heat flow is missing in one direction, so the model is describing a sample and beam which is infinitely long in one of the lateral directions whilst explicitly modelling the heat flow in the other lateral direction. The 2D-axisymmetric model was considering the “real” situation. The limitation with the 2D-axisymmetric model is that the beam must remain stationary and have circular symmetry which restricts its applications. 3D models were

unfortunately not possible due to the meshing requirements to produce an accurate solution. The mesh elements had to be small in the film, but the lateral dimensions were over 10,000 times larger than the film thickness as required by the laser spot size; this created an extremely large number of elements within the film and made the computational power required to solve the model too high. The geometries of the models are shown in figure 3.

By utilising the symmetries within the 2D model for stationary beams it is possible to reduce the size and computational requirements. The size was reduced by 50% by splitting it down the centre of the beam. Zero heat flux conditions are applied down all the newly created boundaries where the model has been split.

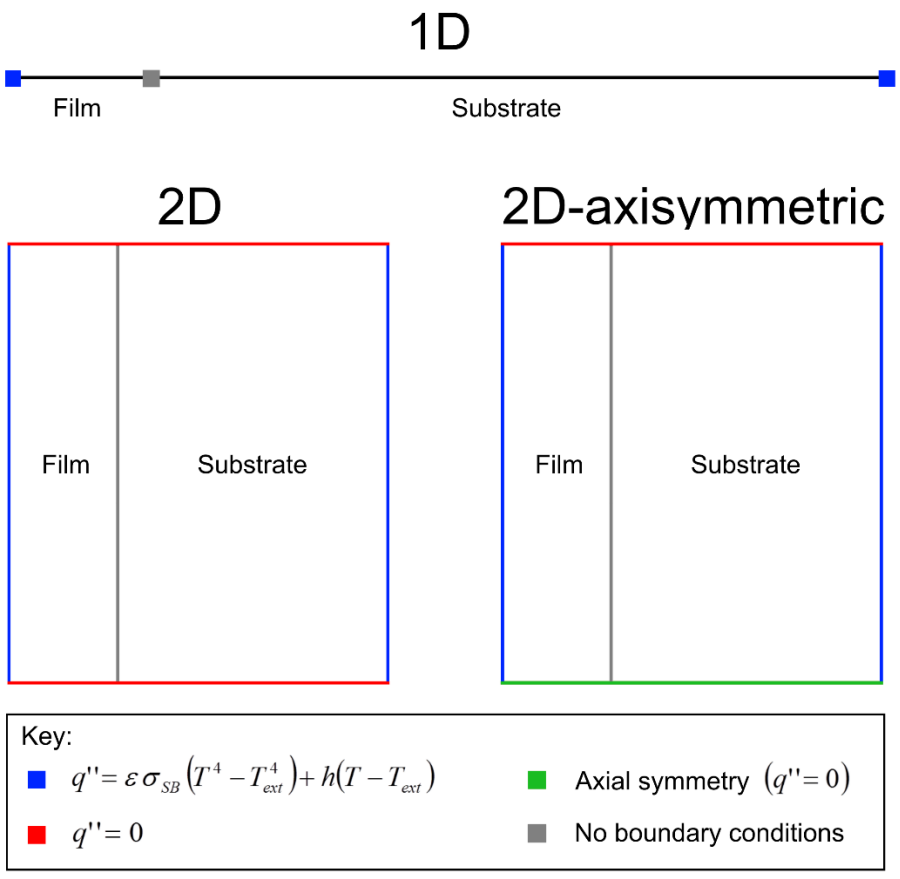

Figure 3 – Geometries of 1D, 2D and 2D-axisymmetric models and their boundary conditions.

4. Material parameters

The samples being considered in this work consisted of Borofloat 33 glass substrates (manufactured by Schott) with a spin-coated ITO ink thin film. The ink was made up of ITO nanoparticles (10-50 nm) dispersed in a UV polymerisable binder, 3-methacryloxypropy-trimethoxsilane (MPTS), and isopropoxyethanol. The purpose of the binder was to aid adhesion and compaction when the polymerisation is activated with UV light. The samples were pre-treated at 70°C for 10 minutes to evaporate remaining solvent and then irradiated with a UV lamp to photo-polymerise the binder. Further processing at high temperatures (550°C) in a furnace significantly reduced the resistivity of such coatings and the aim was to determine the conditions required to replace this step with laser processing.

For the modelling work to be conducted, optical and thermal parameters for both the substrate and ITO film were required. This consisted of the complex refractive index, thermal conductivity, heat capacity, density and emissivity. Additionally, to model convection, the dynamic viscosity and thermal expansion coefficient for air were required to calculate the heat transfer coefficient.

4.1. Air

The material properties of air were taken from the COMSOL 5.2a material library.[41] The refractive index was assumed to be 1 across all the wavelengths of interest with no imaginary component. SI units apply throughout with the temperatures in kelvin. The thermal conductivity was given by equation 42.

$$\kappa(T) = A + BT + CT^2 + DT^3 + ET^4 \tag{42}$$

$$A = -0.00227583562$$
$$B = 1.15480022 \times 10^{-4}$$
$$C = -7.90252856 \times 10^{-8}$$
$$D = 4.11702505 \times 10^{-11}$$
$$E = -7.43864331 \times 10^{-15}$$

The heat capacity was given by equation 43.

$$c(T) = A + BT + CT^2 + DT^3 + ET^4 \tag{43}$$

$$A = 1047.63657$$
$$B = -0.372589265$$
$$C = 9.45304214 \times 10^{-4}$$
$$D = -6.02409443 \times 10^{-7}$$
$$E = 1.2858961 \times 10^{-10}$$

The temperature dependent density was given by equation 44 which was also used by COMSOL to calculate the coefficient of thermal expansion.

$$\rho(T) = \frac{101325 \times 0.02897}{8.314\,T} \tag{44}$$

Finally, the dynamic viscosity for air was given by equation 45.

$$\mu(T) = A + BT + CT^2 + DT^3 + ET^4 \tag{45}$$

$$A = -8.38278 \times 10^{-7}$$
$$B = 8.35717342 \times 10^{-8}$$
$$C = -7.69429583 \times 10^{-11}$$
$$D = 4.6437266 \times 10^{-14}$$
$$E = 1.06585607 \times 10^{-17}$$

4.2. Borofloat 33

Borofloat 33 is a borosilicate glass manufactured by Schott. Its properties were taken from manufacturer's data where possible.[42] For non-constant values the data was digitised from graphs included in the manufacturer's literature. A function which produced a high coefficient of determination, indicating a good fit, was then fitted to provide an analytical equation for use within the models.

The real part of the refractive index was approximately provided by Schott in the range of 365-1015 nm. The Cauchy dispersion relationship (equation 46) was fitted to the given refractive index data; the fit only seemed to significantly deviate towards the IR region where this function is known to become inaccurate. The Cauchy equation also becomes inaccurate towards the UV region due to strong absorption often occurring.

$$n(\lambda) = B + \frac{C}{\lambda^2} \tag{46}$$

A Sellmeier fit (equation 47) was also tested but gave an almost identical result so the simpler Cauchy equation was used.

$$n(\lambda) = 1 + \frac{B_1\lambda^2}{\lambda^2 - C_1} + \frac{B_2\lambda^2}{\lambda^2 - C_2} + \frac{B_3\lambda^2}{\lambda^2 - C_3} \tag{47}$$

In order to determine whether it was appropriate to use the Cauchy relationship to predict a refractive index at 325 nm, transmission measurements were taken on a 2 mm thick Borofloat 33 substrate (inset in figure 4). There was only very minimal absorption observed with less than 1% change in the transmission compared to the visible region of the spectrum. It was therefore determined that the Cauchy equation was appropriate to use to determine the refractive index at 325 nm.

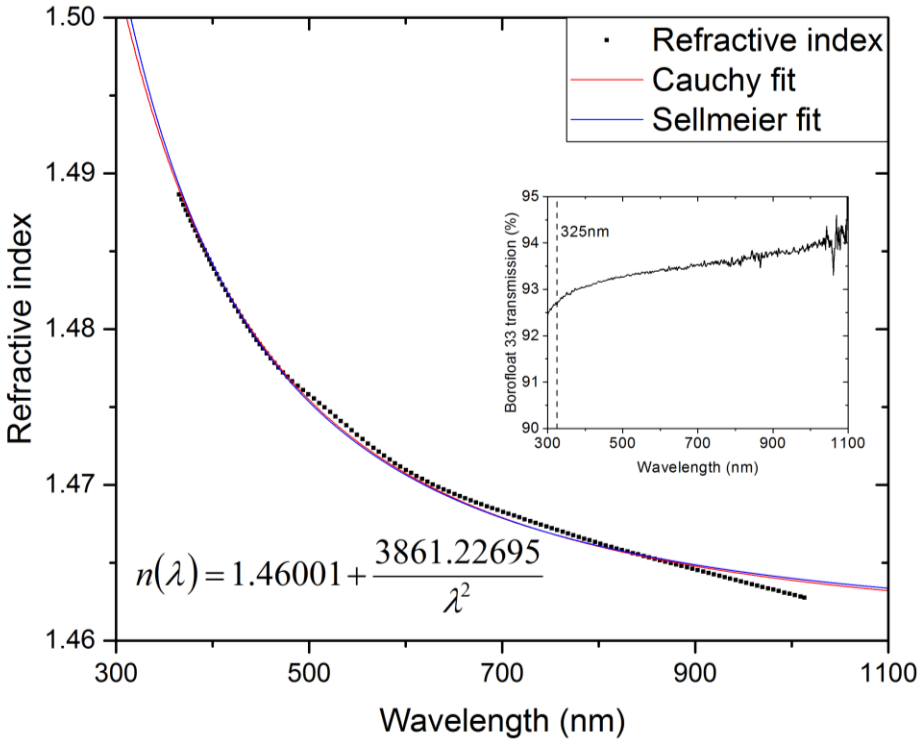

Figure 4 – Refractive index of Borofloat 33 taken from the manufacturer's data[42] *with fitted Cauchy and Sellmeier equations. The inset shows measured Borofloat 33 transmittance.*

The complex part of the refractive index was calculated using the transmission spectrum of an uncoated 2 mm thick Borofloat 33 substrate. This was done by numerically solving equation A11 for α with the f subscripts referring to the substrate rather than the film in this case. [See erratum at the end of Appendix A for correction of equation A11.] The reflectivities were defined explicitly in terms of the real part as well as α from the Fresnel equation. At the two wavelengths of interest, 308 nm and 325 nm, the complex parts of the refractive index were calculated to be 1.37×10^{-6} and 3.91×10^{-7} respectively.

The thermal parameters were also digitised from manufacturer's data; the heat capacity and thermal conductivity are displayed in figures 5 and 6 respectively. Functions have been fitted to the data points to provide an analytical form for use in the models. Outside of the data range supplied by the manufacturer, a constant value has been assumed corresponding to the value at the temperature extremity

provided. It is acknowledged that the thermal conductivity increases linearly within the temperature range provided and the assumption of a constant value above 428.15 K may not be realistic. However due to the uncertainty in how the thermal conductivity would behave at higher temperatures it was decided not to extrapolate the fit. The impact of the thermal parameters of the substrate on the model results are discussed in more detail later in the report.

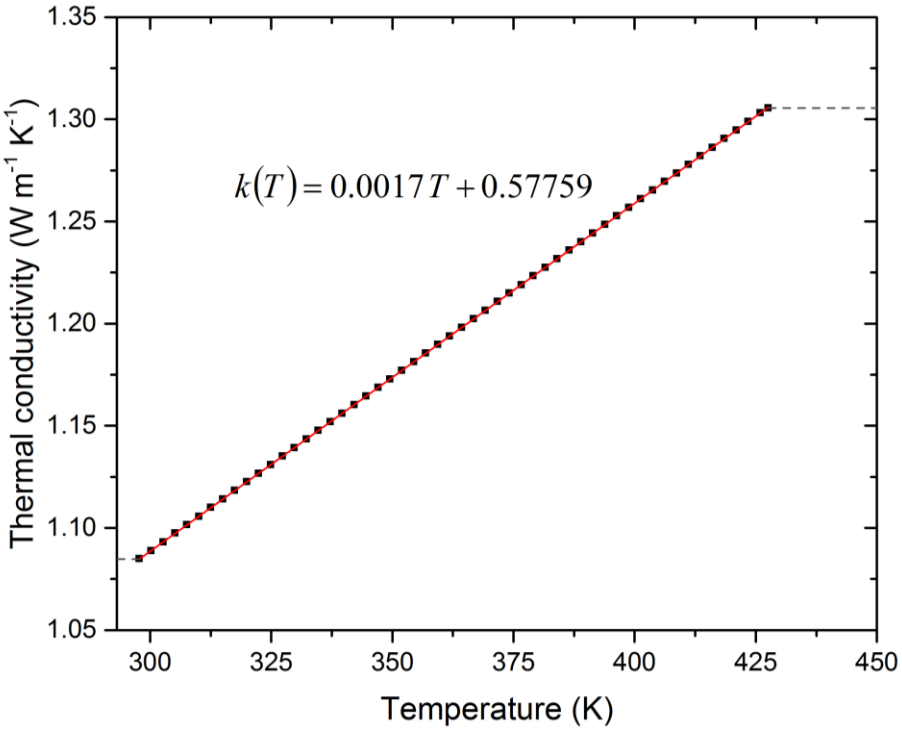

Figure 5 – Temperature dependent thermal conductivity of Borofloat 33 digitised from the manufacturer's data which was provided from 298.15 to 428.15 K.[42] *An analytical function was fitted for use within the models.*

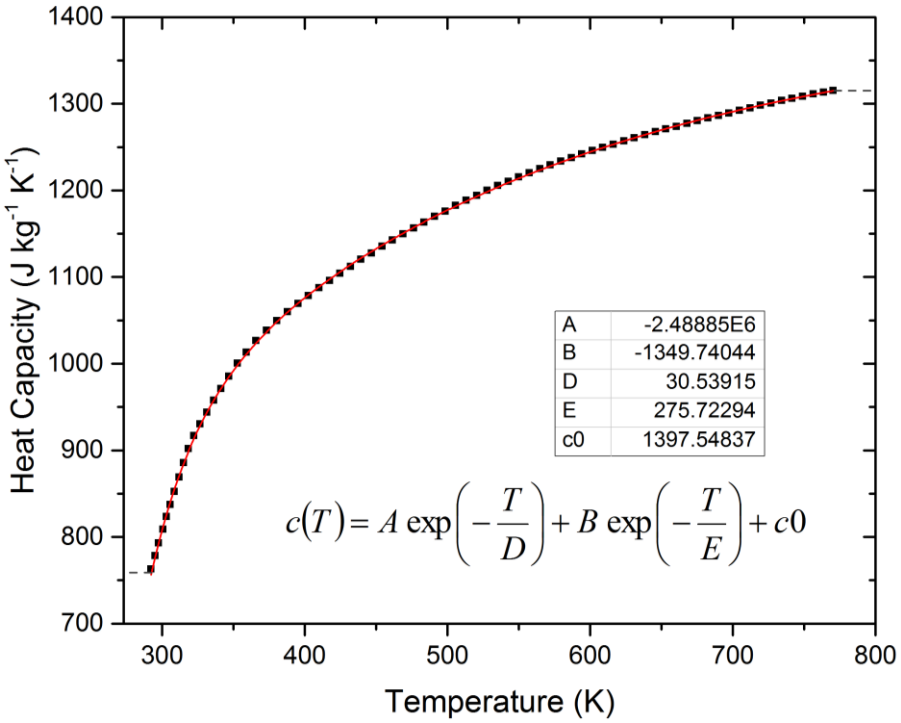

Figure 6 – Temperature dependent heat capacity of Borofloat 33 digitised from the manufacturer's data which was provided from 293.15 to 773.15 K.[42] *An analytical function was fitted for use within the models.*

The density was given as a constant value of 2230 kg·m^{-3}. The emissivity was assumed to be 0.9 as most glasses are located around this value.[43]

4.3. Indium tin oxide

As the ITO ink was a recently developed material, its parameters were not well characterised, and it was not possible to look up these values. There was also the added complexity that the deposited thin films were not a single homogenous material and they could also only be deposited as thin films making the measurement of some of its parameters challenging. Therefore, attempts were made to approximate the values utilising the bulk properties of ITO which are discussed here.

The thermal conductivity of ITO can vary depending on the quality of the material, particularly how electrically conductive it is. It has been reported that the thermal conductivity contribution from phonons for polycrystalline sputtered ITO is almost constant and independent of resistivity with κ_{ph}=3.95 W·m^{-1}·K^{-1} (resistivities of 3.2x10^{-3} to 3.8x10^{-4} Ω·cm were used in this work).[44] The electronic contribution to the thermal conductivity can be estimated using the Wiedemann-Franz law (equation 48) where L_0 is the Lorenz number, T is the temperature and ρ is the electrical resistivity.

$$\kappa_{el} = \frac{L_0 T}{\rho} \tag{48}$$

Whilst this equation is typically used for metals, it is also valid for degenerately doped semiconductors, such as conductive ITO. The Lorenz number can depend on the dopant concentration amongst other parameters, sometimes producing a significantly smaller Lorenz number and a lower contribution to the thermal conductivity.[45,46] A Lorenz value of 2.44x10^{-8} W·Ω·K^{-2} was used in this work. It is not possible to measure the electrical resistivity of a single ITO nanoparticle therefore the electrical resistivity of the ITO nanoparticles within the films were

assumed to be equal to that of the most conductive film produced in previous work using this ink of $1.5x10^{-3}$ Ω·cm.[47] This gave an electronic contribution to the thermal conductivity of 0.47 $W \cdot m^{-1} \cdot K^{-1}$. Adding the electronic and phononic contributions produced a total thermal conductivity for the ITO of 4.42 $W \cdot m^{-1} \cdot K^{-1}$. This assumed the constant phonic value of 3.95 $W \cdot m^{-1} \cdot K^{-1}$ that was determined in reference 44.

The specific heat was taken to be that of the bulk In_2O_3 crystal as has been common practice in the work of several others.[48–50] Data measured by adiabatic calorimetry was taken from 51 and a functional form was fitted in the range of 293.15-1000 K (figure 7).

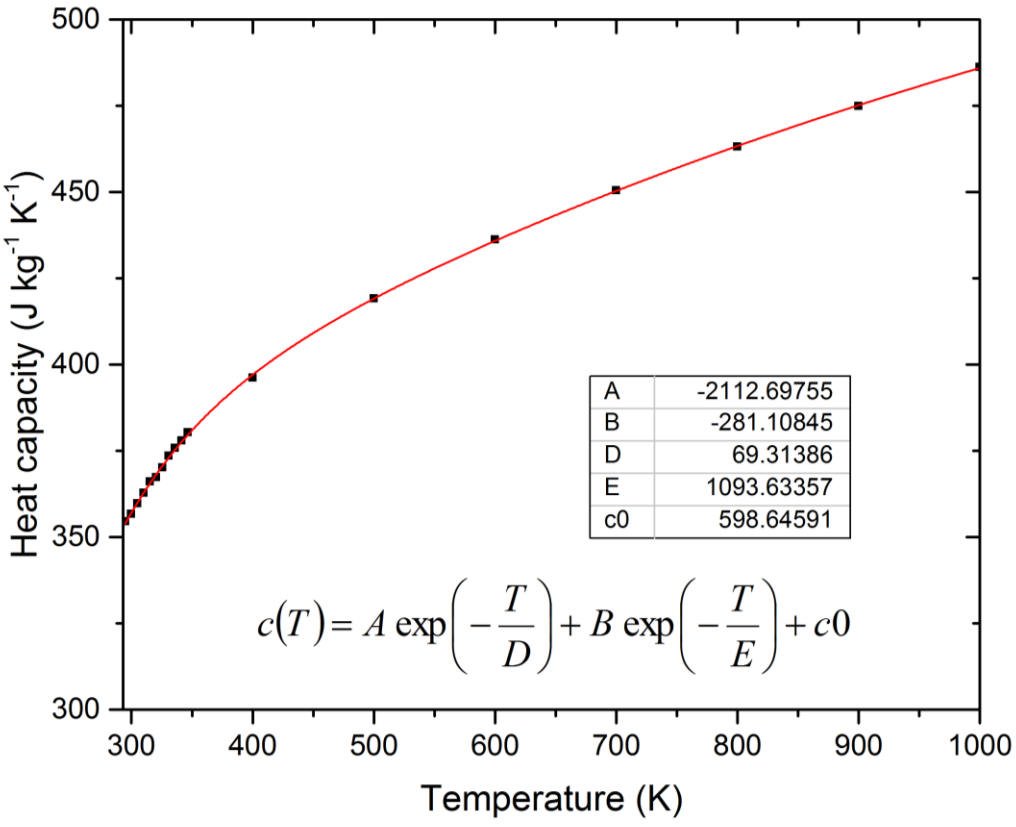

Figure 7 – Temperature dependent heat capacity of In_2O_3 with the data points taken from reference 51 from 293.15 to 1000 K. A function was fitted for use within the models with the functional form and coefficients given in the figure.

The density of the film was assumed to be the same as that of the bulk In_2O_3 crystal, 7120 $kg \cdot m^{-3}$, as the small percentage of SnO_2 (10%) was not expected to drastically affect this.[48,49]

4.4. Composite film properties

4.4.1. Optical parameters

The refractive index for the ITO film was calculated using the method of Swanepoel,[52] which for the real part of the refractive index is the same as that derived by Manifacier et al.[53] These methods use transmission data for thin weakly absorbing films deposited on transparent substrates to calculate the wavelength dependent refractive index of the film. The real part of the refractive index, n, is given by equation 49 where a is described by equation 50, n_s is the refractive index of the substrate and U and L describe the upper and lower bound curves which encapsulate the interference pattern (illustrated in figure 9). The details of how these equations were derived will not be described here but they are given in references 52 and 53.

$$n(\lambda) = \left(a(\lambda) + \left(a(\lambda)^2 - n_s(\lambda)^2 \right)^{0.5} \right)^{0.5} \tag{49}$$

$$a(\lambda) = \frac{2\, n_s(\lambda)\left(U(\lambda) - L(\lambda)\right)}{U(\lambda)L(\lambda)} + \frac{n_s(\lambda)^2 + 1}{2} \tag{50}$$

The optical transmission of a 400 nm thick ITO ink film on Borofloat 33 was measured from 190 nm to 1100 nm with air as a reference as performed in the previously discussed papers (figure 8). The film thickness was measured with a DektakXT surface profiler with a scratch made into the film down to the glass surface.

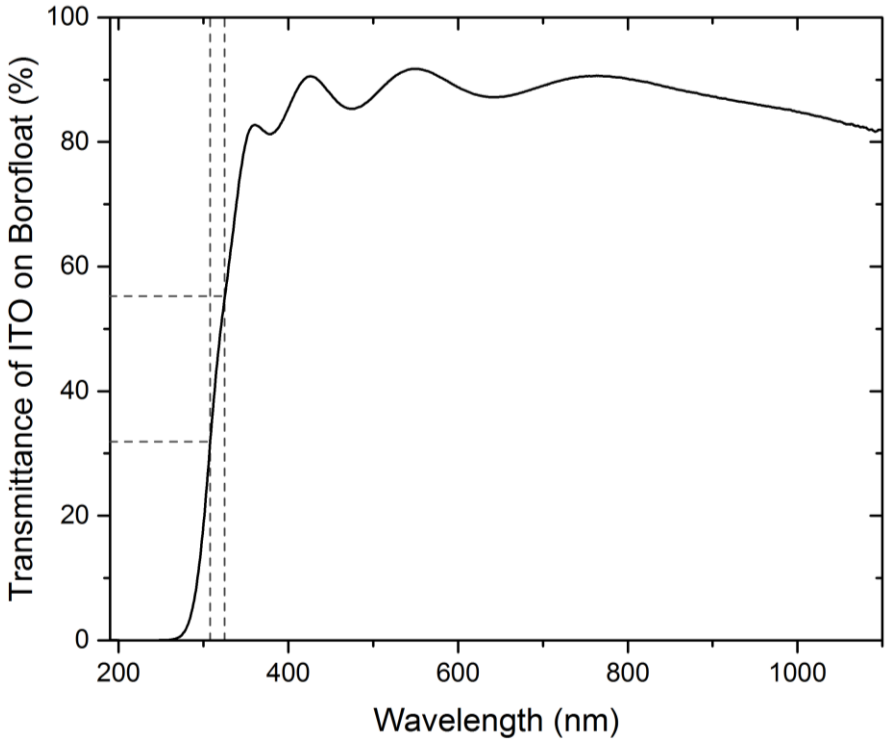

Figure 8 – Transmission spectrum of 400 nm ITO film on Borofloat 33 substrate. The dashed lines indicate the transmittance at the laser wavelengths of interest within this work (308 and 325 nm).

The Swanepoel method requires two functions to be fitted around the transmission data to form an envelope enclosing the data with an upper and lower curve (see figure 9). The only wavelength range that can be considered was where interference fringes were clearly visible, from 350-800 nm in our case. Below 350 nm the film was highly absorbing and could not be treated with this method and beyond 800 nm the spectrophotometer signal began to drop, and no more interference fringes were observed.

The coordinates of the maxima and minima on the transmission curve were determined manually from the dataset. These points were used to generate the upper and lower bounds (the envelope). No analytical function could be found that provided a good fit to the extracted minimum and maximum data points so an interpolating function was used in Mathematica 10.2 instead, as

recommended by the authors of the method.[52] The interpolation fits a polynomial curve between each data point. This caused some problems as there were not many data points available and they were spread quite far apart leading to oscillations between some of the data points due to the interpolation. This did not accurately describe an upper and lower bound so to aid with the fitting, three fictitious data points were manually selected between the peaks for the upper bound curve to aid the interpolation. All of the data points that were used are displayed in figure 9 along with the original transmission data and final upper and lower bound curves.

As the lower bound curve started to deviate from the data at higher wavelengths and there was not another minimum on the spectrum to guide the eye as to how to lower bound curve should look, it was decided that it was not appropriate to insert further data points to extend the curve. Instead, refractive index analysis was only carried out up to 650nm as indicated by the dashed line in figure 9.

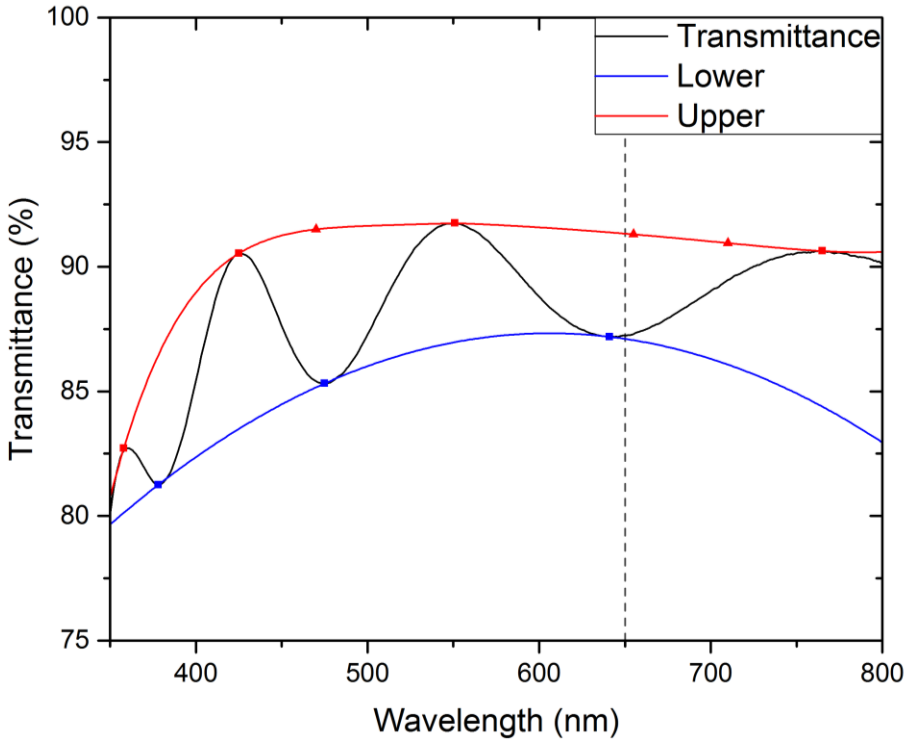

Figure 9 –Transmission spectrum of ITO film on Borofloat 33 substrate with fitted upper and lower bound curves for refractive index analysis. The three fictitious points that were used to aid fitting are indicated by triangles.

With this data and the Cauchy dispersion for the Borofloat 33 (figure 4) it was then possible to calculate a refractive index for the thin film according to equation 49 (figure 10).

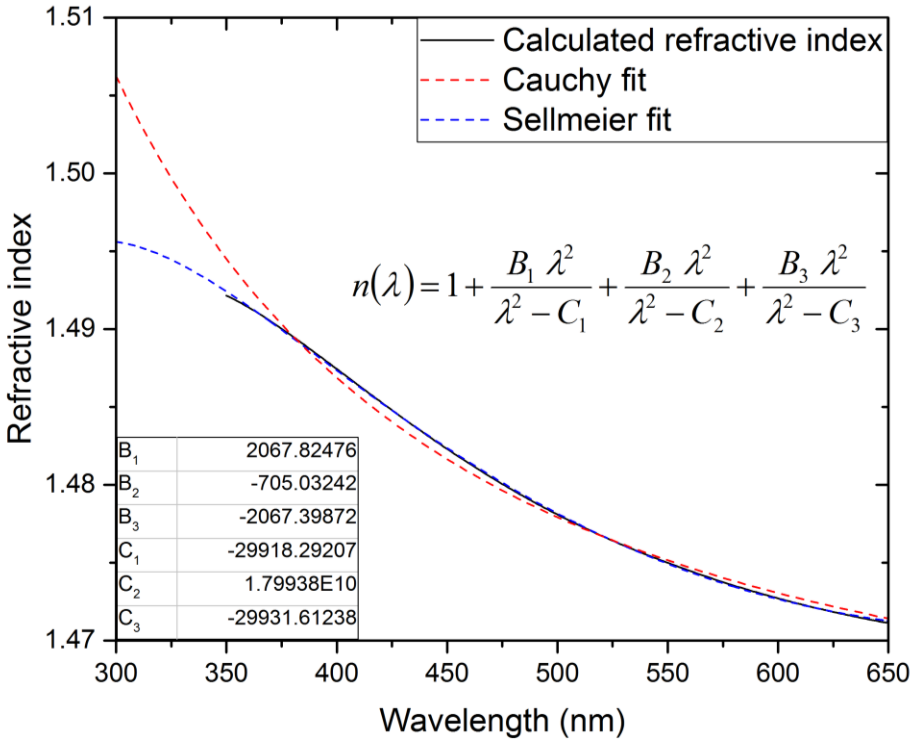

Figure 10 – Calculated refractive index of the ITO film with fitted Cauchy and Sellmeier equations. The Sellmeier equation produced a better fit and its equation and coefficients are included in the figure.

This provided the real part of the refractive index in the visible range, which was fitted with Cauchy and Sellmeier dispersion functions. The Sellmeier function provided a much better fit so was used throughout the rest of this work. As we planned to work with 308 and 325 nm lasers, the data for the refractive index was extrapolated using the Sellmeier fit to this point. This was determined to be an acceptable method as the dispersion over 50 nm was unlikely to be large enough to significantly alter the energy dissipated into the sample.

The imaginary part of the refractive index was also required. However, before determining this, it was decided to investigate whether scattering contributed significantly to the optical extinction within the nanoparticulate film at the wavelengths of interest. Whilst the films were very transparent and had a low

haze in the visible region of the spectrum the UV light could have interacted differently.

Mie theory was used to quantify the amount of light that was scattered and absorbed by the ITO nanoparticles. The extinction, scattering and absorption cross sections were calculated using MiePlot v4.5 at wavelengths of 308 nm and 325 nm for a single spherical ITO nanoparticle (figures 11 and 12).[54] The refractive index was taken from published values and the surroundings were assumed to be air.[55,56]

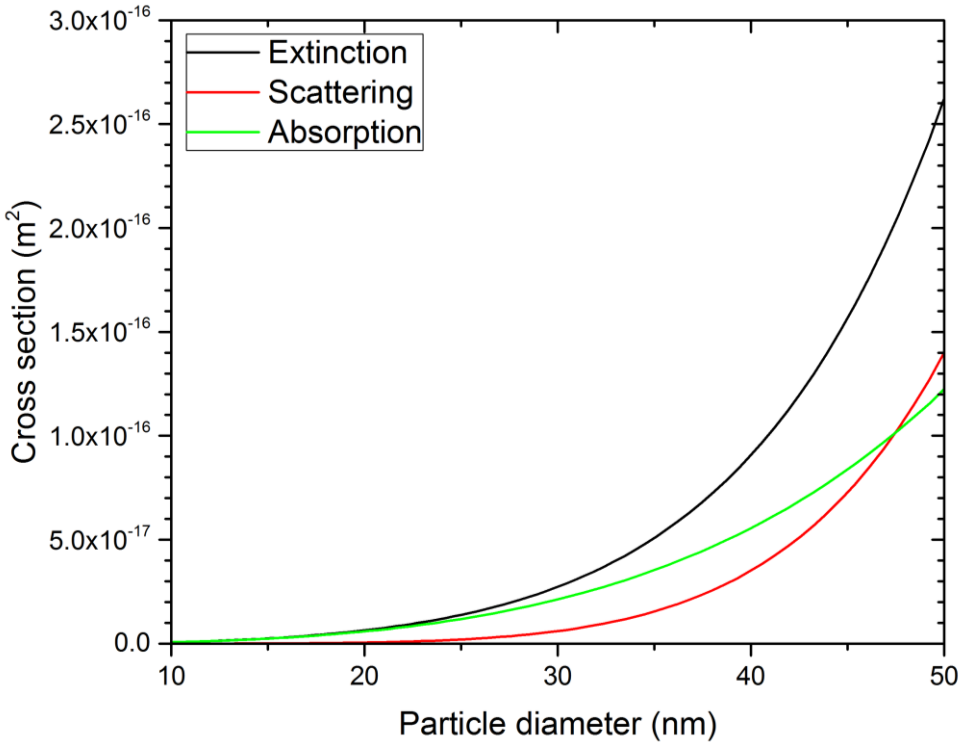

Figure 11 – Extinction, scattering and absorption cross sections calculated using Mie theory for 308 nm light incident on a spherical ITO particle of varying diameter in air. MiePlot v4.5a was used for these calculations[54] with the ITO refractive index taken from published values.[55,56]

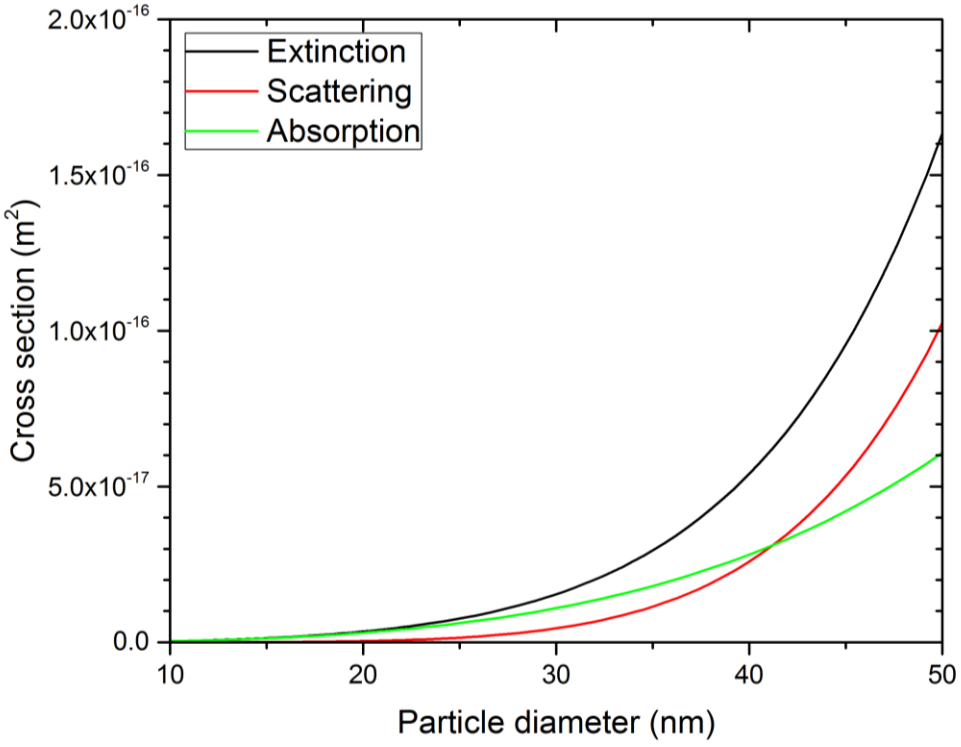

Figure 12 – Extinction, scattering and absorption cross sections calculated using Mie theory for 325 nm light incident on a spherical ITO particle of varying diameter in air. MiePlot v4.5 was used for these calculations[54] *with the ITO refractive index taken from published values.*[55,56]

To determine whether scattering or absorption was dominant, the particle size needed to be known so an SEM image of the sample was taken at the Leibniz Institut für neue Materialien (figure 13).

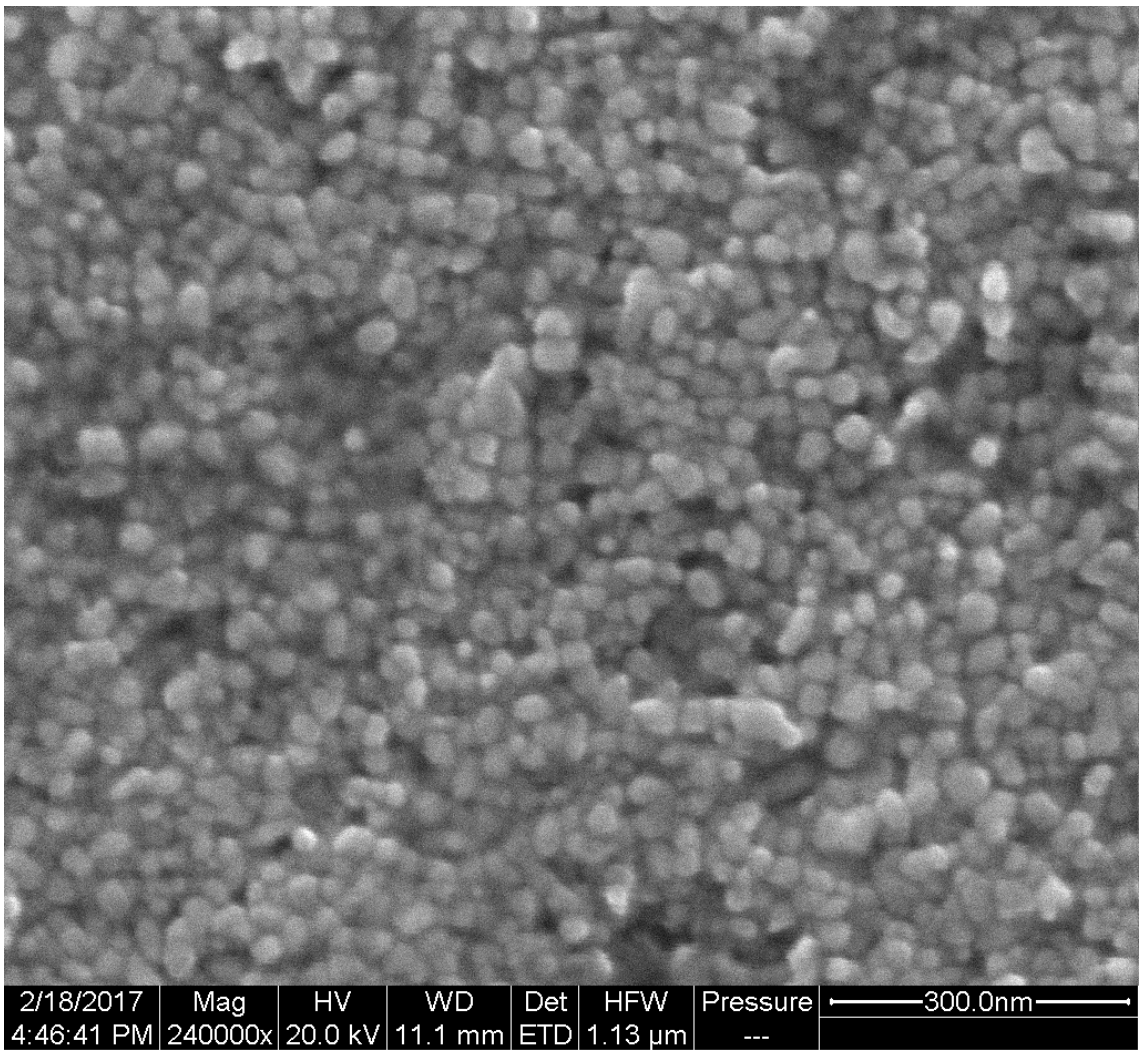

Figure 13 – SEM image of ITO film showing particles of approximately 30 nm in diameter.

Particle size analysis was performed by measuring the size of 250 particles on the SEM image (figure 13) using ImageJ 1.50i.[57] As some of the particles were non-spherical, the elliptical particle tool was used and the average diameter was calculated from the mean of the major and minor diameters. This determined that majority of the particles were between 20 and 50 nm in diameter (figure 14).

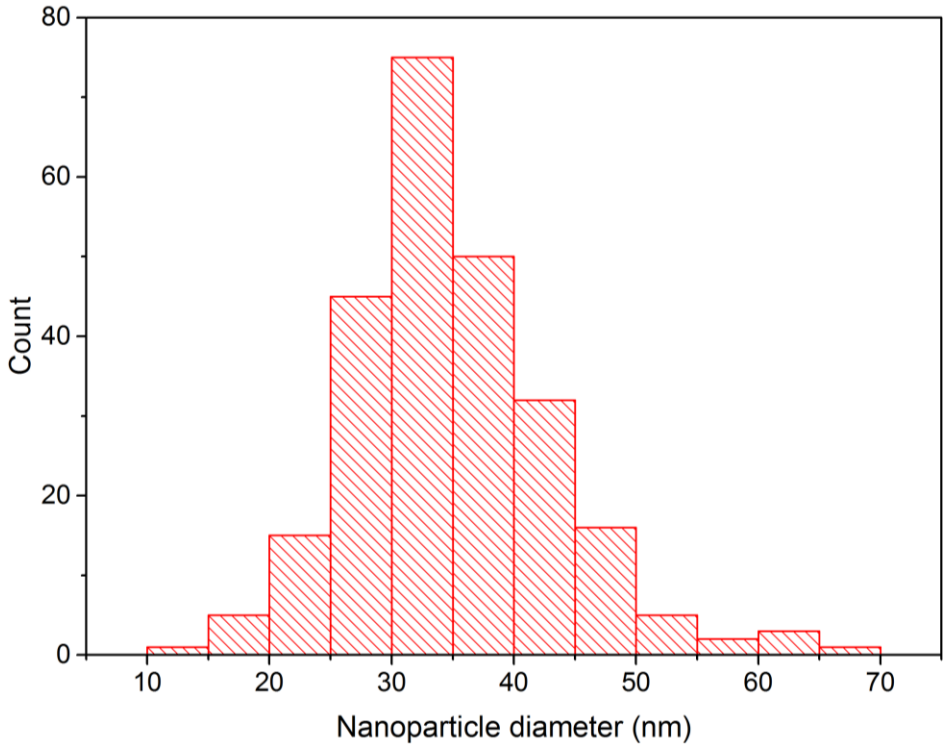

Figure 14 – Histogram of ITO nanoparticle diameters using figure 13 and the ImageJ 1.50i software.[57]

This indicated that a sizable portion of the incident light would be scattered, particularly by the larger particles. The larger particles would also have a larger effect in terms of both absorption and scattering indicated by the magnitude of the cross section. Therefore, as the larger particles scatter more than they absorb and have a larger effect than the smaller particles, it was likely that the scattering contribution to the extinction would be high. However, there were some limitations with the methods used as they only considered a single spherical nanoparticle and assumed the surrounding material was air. The film actually consisted of many nanoparticles which weren't perfectly spherical, and they were surrounded by the MPTS binder which had unknown optical properties. If the MPTS was well index matched to the ITO this could have significantly reduced the scattering. Mie theory also couldn't provide insight into the effects of the multiple scattering events that would occur within the film; this would have increased the optical path

length and could have increased the light absorption. Therefore, to scrutinise this further, a simple experiment was conducted to determine whether the scattering contribution to the extinction was significant.

A Kimmon IK 3552R-G HeCd laser beam (325 nm) was directed into a large area ThorLabs S120VC photodiode power sensor connected to a ThorLabs PM320E dual channel optical power and energy meter. The large area detector ensured that any scattered light was collected. A power reading of the uninterrupted beam was taken and bare Borofloat 33 substrate was then placed into the beam path and a second power reading recorded. Finally, the substrate was replaced with the ITO sample and the power was measured once again. This allowed transmittance values through the bare and coated substrate to be calculated, including any forward scattered light. This procedure was then repeated with an iris attached to the photodetector such that the iris clipped the very edge of the beam on all sides. In this case, any light that was scattered out of the beam path was not measured and the difference in the transmittance between the bare and coated substrate quantified the amount of light that was being scattered out of the beam path by the sample. A schematic of the experimental setup is shown in figure 15.

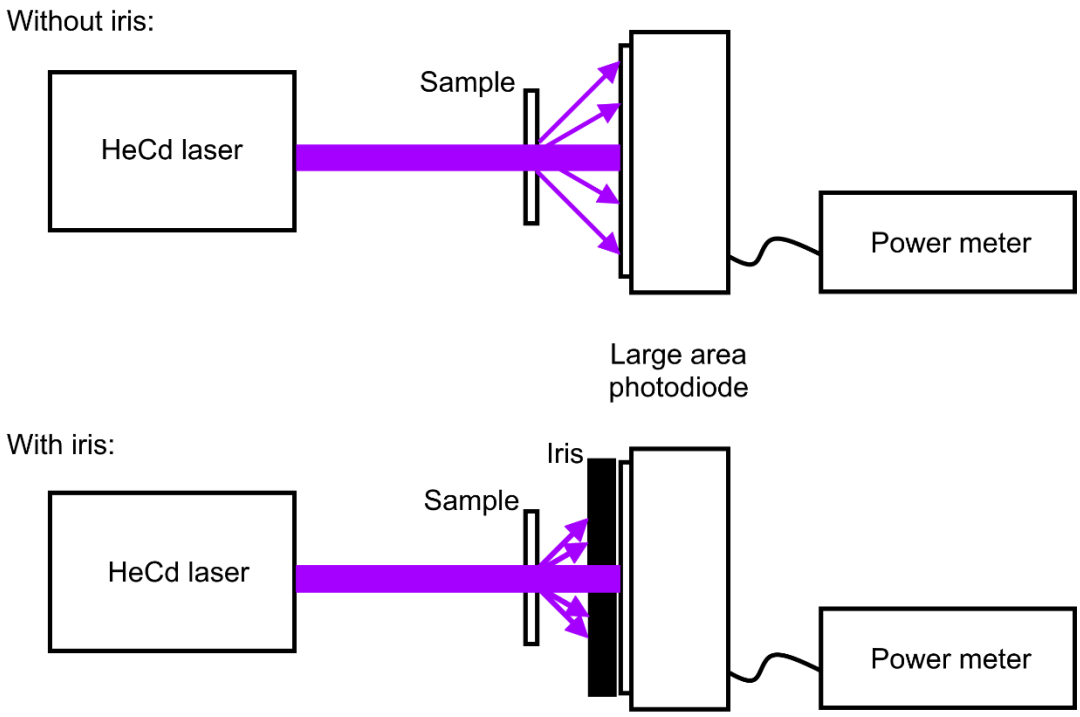

Figure 15 – Schematic of experimental setup to measure the degree of scattering of the HeCd laser by the ITO coated Borofloat sample. With the iris present, the scattered light is not measured by the large area ThorLabs S120VC photodiode power sensor.

The difference between the transmittance of the substrate and the sample was 30.3% for the uncovered photodetector and 30.8% with the iris in place. This slight difference was within the margin of error of the setup and it was clear that no significant amount of light was being scattered by the sample such that it deviated from the original beam path. This was not repeated at 308 nm, but no significant difference was expected over such a small wavelength change as confirmed by comparison of figure 9 with figure 10. Based on these measurements, it was determined that it was appropriate to assume that the absorption was approximately equal to the extinction.

Swanepoel also gave an equation to calculate (approximately) the imaginary part of the refractive index in the strongly absorbing regime where the interference fringes disappear.[52] This is given by equation 51.

$$k(\lambda) = -\frac{\lambda}{4\pi d}\ln\left(\frac{(n(\lambda)-1)^3\left(n(\lambda)+n_s(\lambda)^2\right)}{16\,n(\lambda)^2\,n_s(\lambda)}\right)T \qquad (51)$$

At 325 nm this equation gave a value of k=0.170, which corresponded to an internal transmission of 7.25%. This was smaller than was expected from transmission measurements performed which measured 54.95% overall transmission through both the ITO and substrate (figure 8). This could have been down to errors in the refractive index values used as both the refractive index of the film and substrate were extrapolated outside of the calculated/measured data range. For this reason, it was decided to calculate k using the transmission graph and the measured film thickness. It was most important that k was known accurately as this determined how much laser energy was being deposited into the film, whereas deviations in the real part of the refractive index only caused slight changes in the deposited energy due to slight changes in the reflectivity.

With the assumption of a Beer-Lambert absorption, the absorption coefficient was calculated by numerically solving equation 52 for α_f. [See erratum at the end of Appendix A for correction of equation 52.] The derivation of this equation is shown in Appendix A. It includes the effects of multiple reflections within the thin film but does not consider any interference effects and assumes that light scattering is negligible.

$$T = (1-R_3)\frac{(1-R_1)(1-R_2)\exp(-\alpha_f d_f)}{1-R_1 R_2 \exp(-3\alpha_f d_f)}\exp(-\alpha_s d_s) \qquad (52)$$

This was solved numerically by defining the reflectivities according to the Fresnel equation (equation 23) with the refractive index of the film described as by equation 53 where n_f is defined by the Sellmeier fit in figure 10.

$$\bar{n}_f = n_f + i\frac{\alpha_s \lambda}{4\pi} \quad (53)$$

At 308 nm a transmittance of 31.92% led to a calculated absorption coefficient of 2.37×10^6 m^{-1} and corresponding k value of 0.0581. At 325 nm, a transmittance of 54.95% led to a calculated absorption coefficient of 1.22×10^6 m^{-1} corresponding to a k value of 0.0299. These values were used in the laser induced heating models.

4.4.2. Thermal parameters

The thermal conductivity of the film was also unknown and difficult to measure for such small amounts of material so attempts to quantify it were based on the properties of bulk ITO. As the films were inhomogeneous and contained pores of air, models of effective thermal conductivities for composite materials were considered. These methods were simplified by not including the effects of the binder that surrounded the nanoparticles.

The packing density in the ITO films was observed to be quite high based on SEM image of the film surface shown previously (figure 13). With a low estimate of loose random packing, the volume fraction of ITO would be 0.601, which limited the models that could be used to accurately describe an effective thermal conductivity as most models were only valid for lower packing densities.[58] The most promising approach seemed to be the Bruggemann model, but this meant that the Kapitza resistance must be known between the ITO nanoparticles and the MPTS.[58] The Kapitza resistance describes the resistance to thermal flow that occurs at an interface between two different media but there is very little published data available for these values and no appropriate data could be found for any TCO materials. To measure the Kapitza resistance, the thermal

conductivity of the composite material must be measured which would in turn obviate the original problem of the unknown thermal conductivity.

Rather than using these simpler models of the thermal conductivity, it was decided to calculate the thermal conductivity by solving the steady state heat equation with finite element software for an assembly of nanoparticles. As it was not realistically possible to recreate the nanoparticle distribution within the films in the FEM software, it was assumed that the system composed of a densely packed face-centred-cubic lattice of monodisperse nanoparticles. A unit cell of 30 nm fcc-packed nanoparticles was created within COMSOL with the surrounding material defined as air as the thermal properties of the MPTS binder were unknown. Zero heat flux conditions were applied to the sides to define the symmetrical conditions. As it was not too computationally taxing, it was decided to expand the model in the vertical direction such that it was approximately as thick as the films under consideration by repeating the unit cell structure (figure 16).

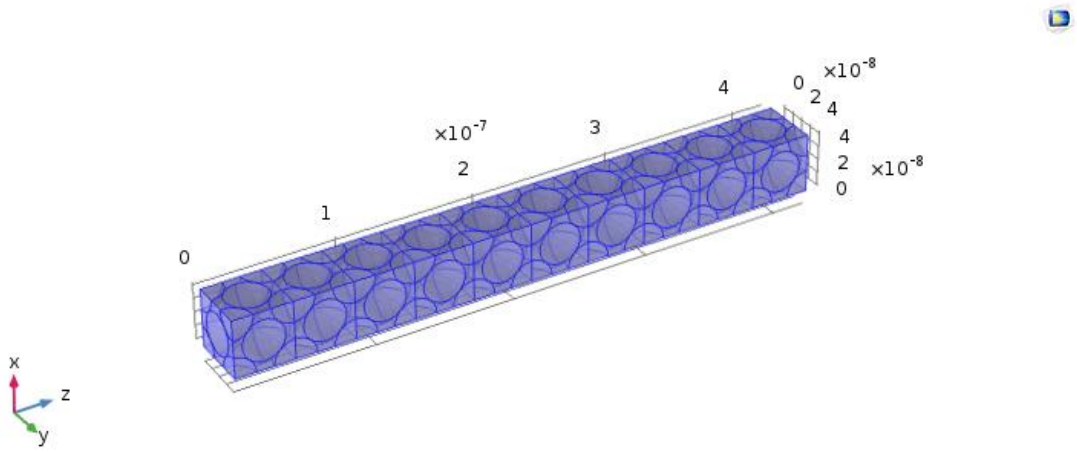

Figure 16 – Geometry of the repeating unit cell built in COMSOL 5.2a that was used to calculate the effective thermal conductivity of the nanoparticulate film. The unit cell consists of 30 nm fcc packed ITO nanoparticles surrounded by air.

On the upper and lowermost boundaries of the model, fixed temperature conditions were applied with a temperature difference of 5 K. The steady state heat transfer equation was then solved which gave the temperature distribution. Equation 54, which is equivalent to Fourier's law in 1D, was used to then calculate the thermal conductivity from the computed heat flux. As the heat flux in the x and y directions was many orders of magnitude smaller than in the z direction these terms were neglected. The heat flux in the z direction was averaged across the whole geometry.

$$\kappa = -\frac{q''_z \Delta z}{T_2 - T_1} \tag{54}$$

As the temperature dependence of the thermal conductivity of air was known, it was decided to repeat this calculation at 5 K intervals. The calculated thermal conductivity of the film as a function of temperature is shown in figure 17.

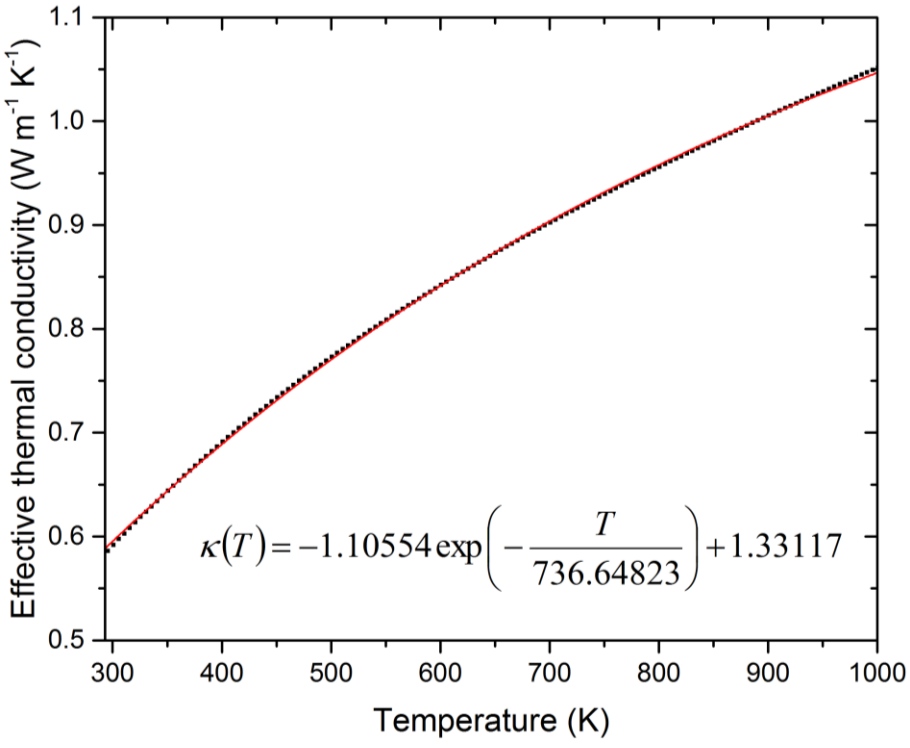

Figure 17 – Calculated effective thermal conductivity of ITO film based on 30 nm ITO nanoparticles with face-centred cubic packing in air.

An effective heat capacity and density also had to be considered, but this was not so simple to model. The approach taken here was to volumetrically weight the heat capacities and densities with the corresponding percentages of ITO and air within the films.[59,60] This is not a perfect method as it assumes that all the components of the film are in thermal equilibrium with each other but it was assumed to be a better estimate than using the bulk ITO properties. As with the calculations of the thermal conductivity, it was assumed that the volume fraction of ITO, ϕ, was equal to that for fcc packing given by equation 55 where r is the radius of the monodisperse nanoparticles.

$$\phi = \frac{\left(4 \times \frac{4}{3}\pi r^3\right)}{\left(2\sqrt{2}\, r\right)^3} = \frac{\pi}{3\sqrt{2}} = 0.74048... \tag{55}$$

The effective density and heat capacity were calculated via equations 56 and 57 respectively using the previously defined values (see tables 1 and 3 in section 4.5, below, for a summary of the properties of air and ITO respectively).[59,60]

$$\rho_{eff} = \phi \rho_{ITO} + (1-\phi)\rho_{air} \tag{56}$$

$$c_{eff} = \phi c_{ITO} + (1-\phi)c_{air} \tag{57}$$

4.4.3. Emissivity

The emissivity of the materials must be known to be able to model radiative losses and to validate the models via IR thermography. There are methods of determining the emissivity which require measuring the IR spectrum of the emitted light from the specimen across a range of temperatures, but this method is critically dependent on the spectrometer calibration over a wide wavelength range which may require multiple detection systems.

As an alternative method, a calibrated hot plate was used along with a FLIR A35 IR camera to estimate the emissivity of the ITO. As a proof of concept, a material of known emissivity was tested first. A 175 μm thick section of PET (polyethylene terephthalate) was coated with a thin layer of Nextel 2010 which has a known emissivity of 0.95.[61] The reverse side of the PET was coated with a thin layer of thermal paste and placed into thermal contact with the hotplate. The IR camera was setup such that it was as close to perpendicular to the hotplate as possible without its own reflection being visible on the camera image. The camera was then focussed onto the hotplate. A reflected temperature measurement was taken by replacing the hotplate with crumpled and reflattened aluminium foil (to act as a diffuse reflector) and taking an image with an emissivity of 1 for the foil. This is used by FLIR's ResearchIR 4.3 software to consider the reflections from other hot objects in the room which are reflecting their radiation into the camera. The room temperature was also recorded with a digital thermometer.

With this setup, thermal images of the Nextel paint were taken at 5°C intervals from 30-130°C allowing the temperature to reach equilibrium for one minute at each interval. The average temperature across the Nextel coated area was then recorded with an emissivity of 0.95 and this was plotted alongside the expected response (figure 18). The shaded areas indicate the uncertainty in the camera results as specified by the manufacturer.

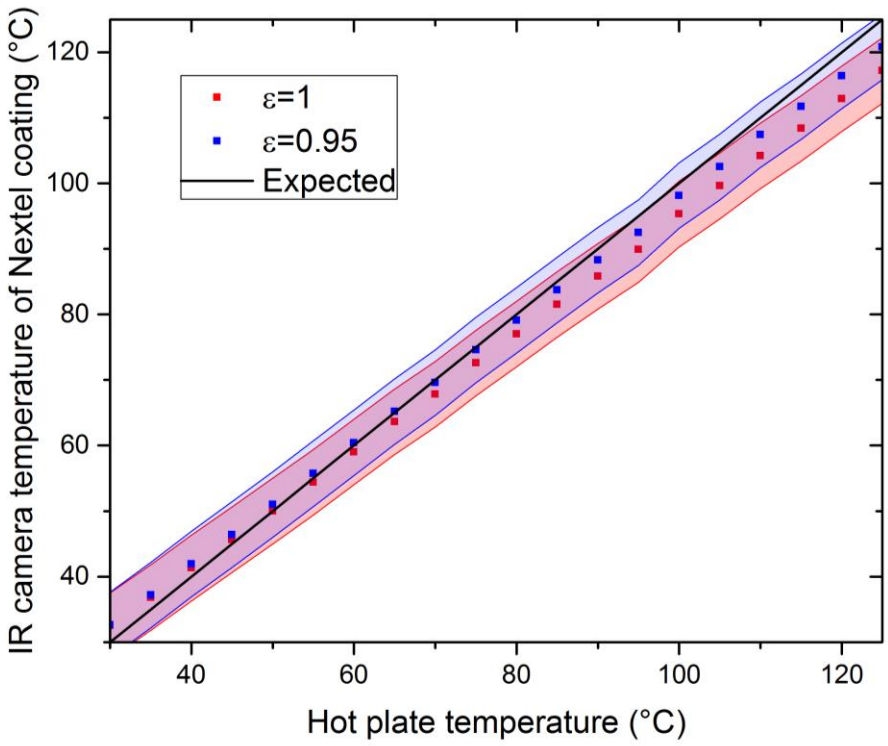

Figure 18 – The emissivity of Nextel 2010 was determined to be approximately 0.95 by measuring the temperature of Nextel 2010 with an IR camera and changing the emissivity until the IR temperature matched the hot plate temperature from 30 to 125 °C. This was in agreement with published data.[61] *The shaded areas indicate the uncertainty in the IR camera temperature measurements.*

This was used as a proof of concept for this method of estimating the emissivity and, as a result of this, the same method was used to estimate the emissivity of the ITO thin film. PET was used as a substrate for this measurement as it was much thinner than the glass substrates and ensured that the film temperature was as close to that of the hotplate as possible. An emissivity value of 0.6 was calculated for the ITO (figure 19).

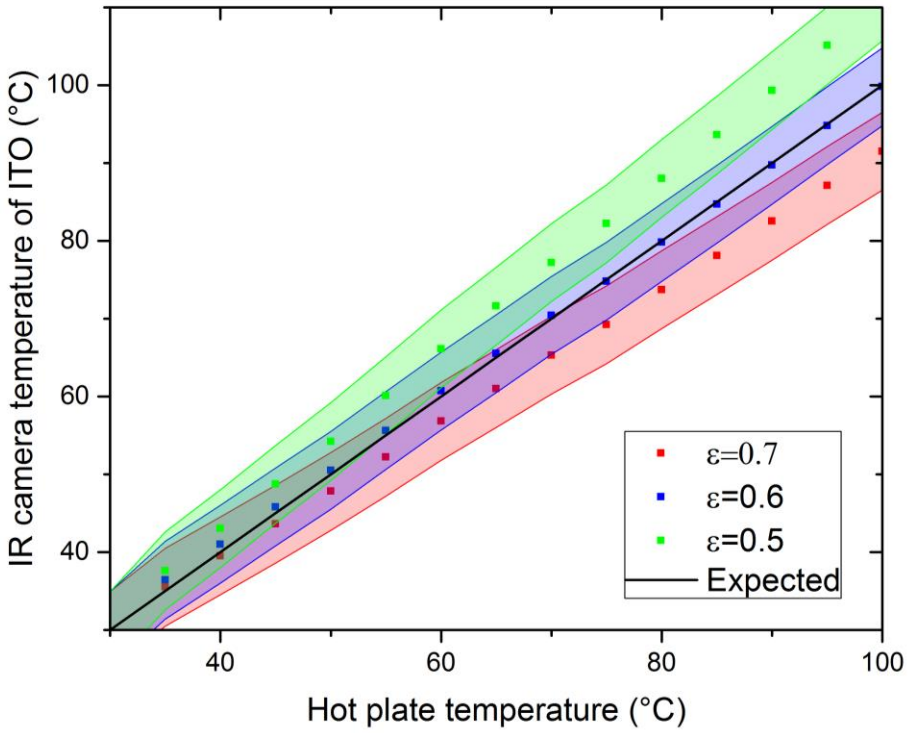

Figure 19 – The emissivity the ITO coating on a PET substrate was determined to be approximately 0.6 using the method that was validated with figure 18. The shaded areas indicate the uncertainty in the IR camera temperature measurements.

4.5. Summary

The material properties that are used within the laser heating models are summarised in tables 1-4. Refractive index values are extrapolated outside of the measured ranges down to 308 nm. For all other parameters, at temperatures outside of valid ranges indicated, the value at the temperature extremity is used.

Table 1 – Material properties of air as taken from the COMSOL 5.2a material library.[41]

Air	Value	Notes
Refractive index	1	
Thermal conductivity ($W \cdot m^{-1} \cdot K^{-1}$)	$A+BT+CT^2+DT^3+ET^4$ $A=-0.00227583562$ $B=1.15480022\times10^{-4}$ $C=-7.90252856\times10^{-8}$ $D=4.11702505\times10^{-11}$ $E=-7.43864331\times10^{-15}$	Valid from 200-1600 K
Heat capacity ($J \cdot kg^{-1} \cdot K^{-1}$)	$A+BT+CT^2+DT^3+ET^4$ $A=1047.63657$ $B=-0.372589265$ $C=9.45304214\times10^{-4}$ $D=-6.02409443\times10^{-7}$ $E=1.2858961\times10^{-10}$	Valid from 200-1600 K
Density ($kg \cdot m^{-3}$)	$\frac{101325\times0.02897}{8.314\,T}$	Utilises ideal gas law, no temperature range given
Dynamic viscosity ($Pa \cdot s$)	$A+BT+CT^2+DT^3+ET^4$ $A=-8.38278\times10^{-7}$ $B=8.35717342\times10^{-8}$ $C=-7.69429583\times10^{-11}$ $D=4.6437266\times10^{-14}$ $E=1.06585607\times10^{-17}$	Valid from 200-1600 K

Table 2 – Material properties of Borofloat 33. The imaginary part of the refractive index was measured experimentally (section 4.2), the emissivity was taken from published values for glass[43] *and the remaining properties were taken from the manufacturer's data.*[42] *All functions were fitted to the provided data with the refractive index extrapolated past the given range.*

Borofloat 33	Value	Notes
Refractive index (real)	$1.46001+\frac{3861.22695}{\lambda^2}$	Cauchy fit to data from 365-1015 nm
Refractive index (imaginary) at 308nm	1.37×10^{-6}	
Refractive index (imaginary) at 325nm	3.91×10^{-7}	
Thermal conductivity ($W\cdot m^{-1}\cdot K^{-1}$)	$0.0017T+0.57759$	Valid from 298.15-428.15 K
Heat capacity ($J\cdot kg^{-1}\cdot K^{-1}$)	$A\exp\left(-\frac{T}{D}\right)+B\exp\left(-\frac{T}{E}\right)+c_0$ $A=-2.4885\times10^{-6}$ $B=-1349.74004$ $D=30.53915$ $E=275.72294$ $c_0=1397.54837$	Valid from 293.15-773.15 K
Density ($kg\cdot m^{-3}$)	2230	
Emissivity	0.9	

Table 3 – Material properties of bulk ITO from published data.[44,47–49,51,55,56]

ITO (bulk)	Value	Notes
Refractive index at 308 nm	$2.30+0.084\,i$	
Refractive index at 325 nm	$2.22+0.0432\,i$	
Thermal conductivity ($W\cdot m^{-1}\cdot K^{-1}$)	4.42	
Heat capacity ($J\cdot kg^{-1}\cdot K^{-1}$)	$A\exp\left(-\frac{T}{D}\right)+B\exp\left(-\frac{T}{E}\right)+c_0$ $A=-2112.69755$ $B=-281.10845$ $D=69.31386$ $E=1093.63357$ $c_0=598.64591$	Heat capacity of In_2O_3 from 293.15-1000 K
Density ($kg\cdot m^{-3}$)	7120	Density of In_2O_3

Table 4 – Material properties of the ITO film determined using the methods discussed in section 4.4.

ITO film	Value	Notes
Refractive index (real)	$1+\frac{b1\lambda^2}{\lambda^2-c1}+\frac{b2\lambda^2}{\lambda^2-c2}+\frac{b3\lambda^2}{\lambda^2-c3}$ $b1=2067.82476$ $b2=-705.03242$ $b3=-2067.39872$ $c1=-29918.29207$ $c2=1.79938\times10^{10}$ $c3=-29931.61238$	Sellmeier fit from data obtained by Swanepoel method from 350-650 nm
Refractive index (imaginary) at 308nm	0.0581	
Refractive index (imaginary) at 325nm	0.0299	
Thermal conductivity ($W\cdot m^{-1}\cdot K^{-1}$)	$A\exp\left(-\frac{T}{B}\right)+C$ $A=-1.10554$ $B=736.64823$ $C=1.33117$	Calculated from 290.65-1000.65 K
Heat capacity ($J\cdot kg^{-1}\cdot K^{-1}$)	$\frac{\pi}{3\sqrt{2}}c_{ITO}+\left(1-\frac{\pi}{3\sqrt{2}}\right)c_{air}$	Heat capacity of In_2O_3 from 293.15-1000 K
Density ($kg\cdot m^{-3}$)	$\frac{\pi}{3\sqrt{2}}\rho_{ITO}+\left(1-\frac{\pi}{3\sqrt{2}}\right)\rho_{air}$	
Emissivity	0.6	

5. Comparison of models for laser heating

The models that were being validated in this work were compared to experimental measurements. Throughout these experiments, the same sample system was used. It consisted of a 400 nm layer of spin coated ITO ink on a 2 mm thick Borofloat 33 substrate. The film thickness was measured using a DektakXT surface profiler with a small scratch made through the film to the substrate. The sample was approximately 32x10 mm in the lateral dimensions. The sample was mounted to on a stage for all measurements such that 5 mm was stuck to the stage and the remaining 27 mm hung over the side so that there was air surrounding the sample. This was done as air had well characterised properties that could be used in the models which needed to be validated. Matt black cardboard was placed several centimetres beneath the sample so that the reflections of infrared light into the thermal camera from surrounding objects were minimized without affecting the thermal transport within the sample.

5.1. Stationary continuous wave HeCd laser

Continuous wave lasers were considered initially. A Kimmon IK3552R-G HeCd laser was used which produced a continuous wave, highly multimode, circular beam with a power of 40.5 mW after all the optical elements. The power was measured with a ThorLabs PM100D power meter and photodiode. The optical system for the HeCd laser was set up as shown in figure 20 with a stage allowing both moving and stationary samples to be processed. The beam propagated through a 2.5 mm diameter circular iris and was imaged onto the sample with a diameter of 300 μm. The beam size was measured by irradiating a piece of PET which was damaged by the laser and then measuring the size of this damage site with an optical microscope.

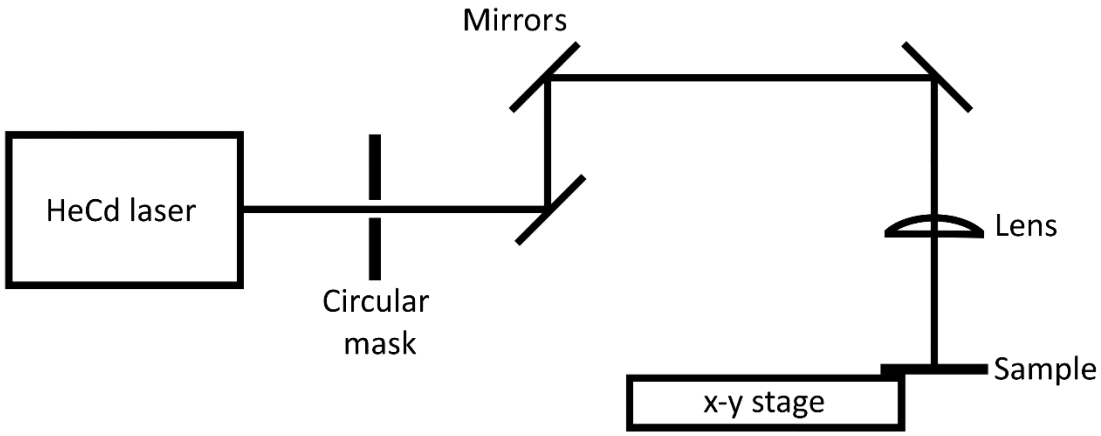

Figure 20 – Optical setup consisting of a Kimmon IK3552R-G highly multimode HeCd laser with a 2.5 mm circular iris, 3 UV-enhanced aluminium mirrors and a 125 mm focal length UV fused silica lens. This formed a 300 μm circular spot on the sample, which was mounted to the edge of an x-y translation stage.

With a stationary beam, the sample was irradiated for different dwell times: 1, 2, 5, 10, 15 and 30 seconds. This was controlled by a relay connected to a signal generator which opened and closed a mechanical shutter according to the

voltage pulse. The duration of the voltage pulse was measured on an Agilent DSO-X 3052A oscilloscope.

The resultant heating of the sample was measured using a FLIR A35 thermal imaging camera. The camera was placed as perpendicular as possible to the sample without being able to see the reflection of the camera from the sample. As the beam was quite small and the camera had a resolution of 320x256 pixels it was important to try and ensure that the camera was as close as possible to the sample without obstructing the laser. Unfortunately, this meant that there were only approximately 2-3 pixels across the beam diameter with each pixel corresponding to approximately 100 μm. The width per pixel was determined from the IR camera recording of the laser heating as the horizontal width from the edge of the stage to the edge of the sample was known to be 27 mm. The horizontal distance was selected to avoid the effects of foreshortening that were apparent in the vertical direction due to the slight angle between the camera and sample. The uncertainty in the width per pixel of was ±5 $\mu m \cdot px^{-1}$ due to the blurry edges of the sample in the recording.

As there were only a small number of pixels across the beam it was difficult to argue that the hottest pixel corresponded to the exact centre of the beam. Therefore, the average temperature over a 3×3 pixel area was calculated, with the hottest pixel at the centre. This average temperature change across this 3×3 area is shown in figure 21 for the different dwell times.

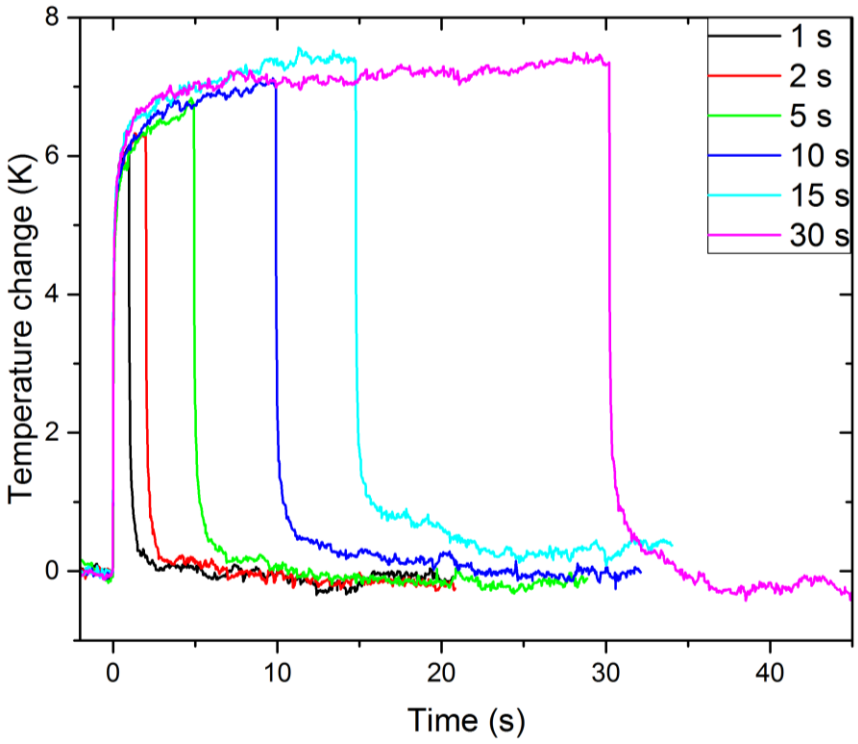

Figure 21 – Measured temperature change of the ITO film due to stationary HeCd laser irradiation at different dwell times. The incident power was 40.5 mW with a uniform 300 µm diameter circular spot.

These results showed quite a small temperature increase of less than 8 K over the beam and indicate that a steady state temperature was reached within a few seconds. After the shutter was closed, the sample rapidly cooled back to room temperature.

The heating and cooling of the sample due to the laser irradiation was investigated with the different models described earlier under the same operating conditions as the experiment. The simplest model was explored first, the El-Adawi semi-analytical model discussed previously. The equations were written into Wolfram Mathematica 10.2 with the material parameters defined as the values at 295.65 K. This model is a 1D description of a thin film on a semi-infinite substrate with no heat loss mechanisms other than conduction into the substrate. The light absorption (hence heat source) was defined as a surface absorption rather than

volumetric. The percentage of incident light absorbed throughout the film thickness was calculated from the complex refractive index and this was used to calculate the deposited energy. The results from this model are shown in figure 22 for different dwell times.

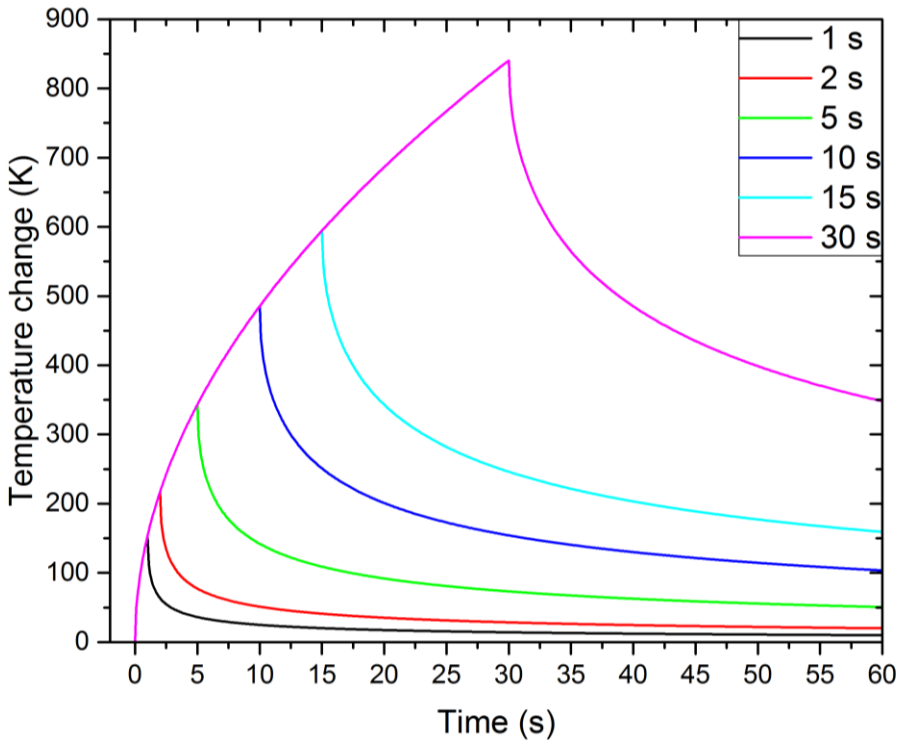

Figure 22 – Calculated temperature change of the ITO film surface (x=0) due to stationary 40.5 mW HeCd laser irradiation at different dwell times using the 1D El-Adawi et al. semi-analytical model.[36]

These results predicted a temperature rise over 100 times larger than was observed with the thermal camera. However, this was not too surprising as many of the assumptions that were made within this model are not strictly valid. This included the surface absorption, no convective or radiative cooling and heat flow being limited to only one dimension. There were no signs of the model approaching steady state conditions (as expected for a 1D model) and the temperature increase was over estimated.

To improve upon this model, another 1D model was tested. This was a numerical model built in COMSOL which had the advantage of using temperature dependent material parameters for all the materials involved. A distributed heat source was also used rather than a surface heat source, which more closely described the real energy loading into the system. Extra heat loss mechanisms were also included by using convective and radiative boundary conditions at the upper film surface and lower substrate surface. The temperature at the film surface calculated by the 1D model is shown in figure 23 as a function of time for different dwell times.

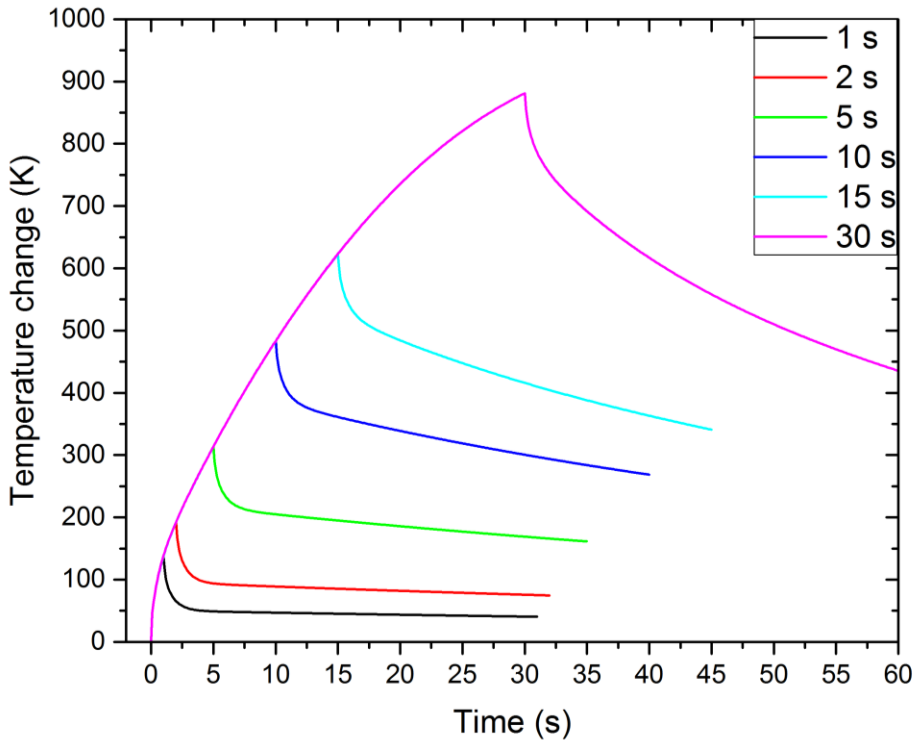

Figure 23 – Calculated temperature change of the ITO film surface due to stationary 40.5 mW HeCd laser irradiation at different dwell times using a 1D numerical model built in COMSOL 5.2a. The model included a distributed heat source and radiative & convective cooling from the upper and lower surfaces of the sample. The thermal parameters included temperature dependence where these were given in section 4.5.

These results looked quite similar to the semi-analytical HeCd model. Slightly lower peak temperatures were predicted by the numerical model than by semi-analytical model at short dwell times, however at longer dwell times the opposite was true. In order to see this more clearly, the 1 and 30 second dwell times are plotted in figures 24 and 25.

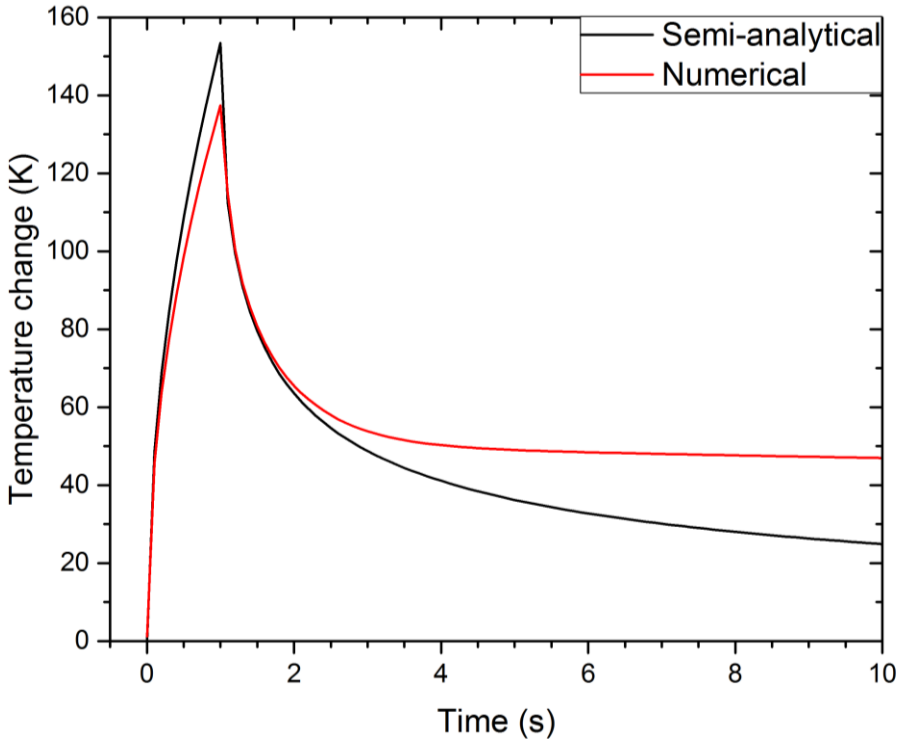

Figure 24 – Comparison of the temperature rises of the ITO film surface predicted using the 1D semi-analytical and numerical models for 40.5 mW HeCd irradiation with a dwell time of 1 second.

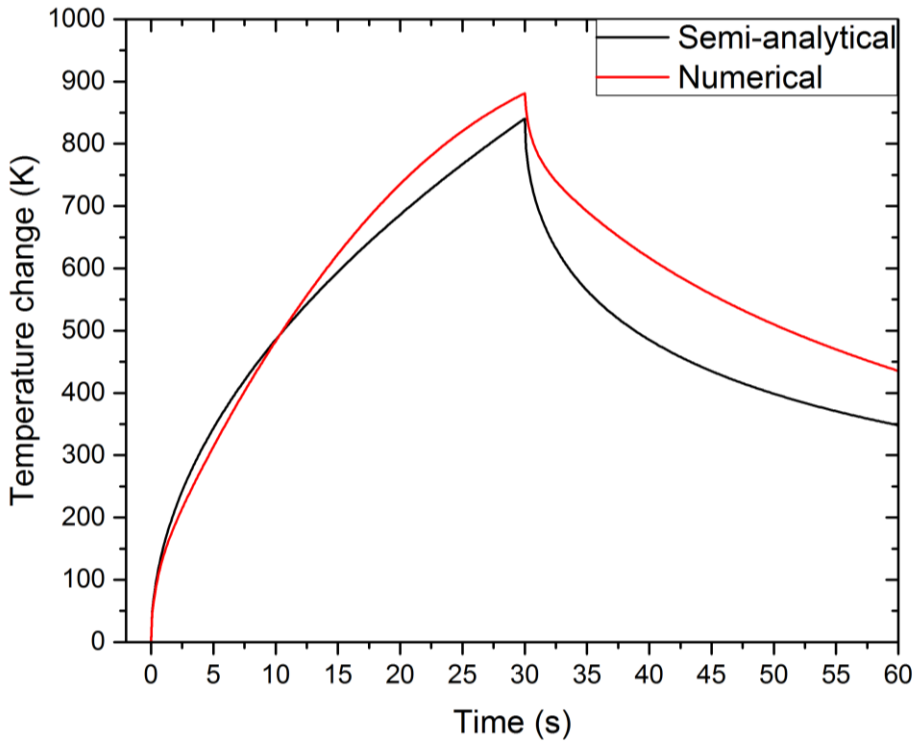

Figure 25 – Comparison of the temperature rises of the ITO film surface predicted using the 1D semi-analytical and numerical models for 40.5 mW HeCd irradiation with a dwell time of 30 seconds.

This could have been affected by both the energy loading within the models and the difference between the fixed and temperature dependent material parameters. By depositing all the energy at the surface (semi-analytical model) rather than throughout the film and substrate (numerical model), a higher temperature would be expected near the surface. To investigate this further, the numerical model was repeated with the temperature independent parameters as used in the semi-analytical model. The numerical model with temperature independent parameters predicted almost identical temperature rises to the semi-analytical model at short dwell times, but at longer dwell times, the numerical model predicted even higher temperature rises than previously. If the energy loading was responsible for the differences, it was expected that the temperature rises would always be lower in the numerical model. As this was not the case, the cooling mechanisms were explored.

The semi analytical model had only one cooling mechanism – conduction into a semi-infinite substrate. The numerical model had a finite substrate thickness but modelled cooling via convection and radiation from the upper and lower surfaces of the sample. The spatial temperature distribution was probed at different times within the models through the film and substrate. During heating, both models predicted large temperature gradients through the sample. The numerical model had slightly lower gradients at the upper surface due to the convective and radiative cooling which was not present in the semi-analytical model. After the laser beam was switched off, the heat source was zero and no energy was deposited into the sample and it began to cool. Within the semi-analytical model, there was an infinite heat sink present as the substrate was infinitely thick, so heat transfer via conduction into the substrate continued indefinitely until thermal equilibrium with the surroundings was reached. However, as the numerical model had finite dimensions, the entire sample had increased substantially in temperature and shortly after the laser beam was switched off, the whole sample reached approximately the same temperature. At this point conduction was minimal because the temperature gradient across the sample was so small. Small temperature gradients existed solely due to the convective and radiative cooling with the maximum temperature located near the centre (depth) of the sample. All the cooling from this point was being limited by convection and radiation compared to the purely conductive cooling within the semi-analytical model. This is illustrated in figure 26 for a 5 second dwell time with the solid lines showing the semi-analytical results and the dashed line showing the results of the numerical model.

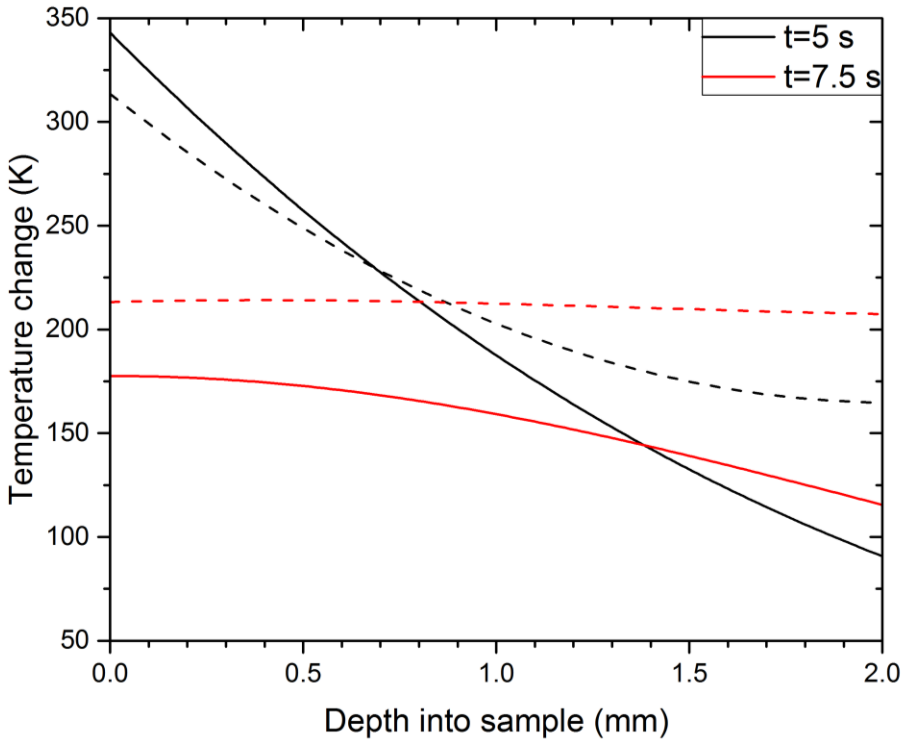

Figure 26 – Comparison of the spatial temperature profile between the 1D semi-analytical (solid lines) and numerical (dashed lines) models for 40.5 mW HeCd laser irradiation with a 5 second dwell time at the end of irradiation (t=5 s) and shortly after irradiation had finished (t=7.5 s).

Whilst there were some differences in the temperature rise between these 1D models, they were only very slight and both models were still two orders of magnitude away from the experimentally measured temperature rises. However, the causes of the subtle differences between the models were interesting and by expanding the numerical model to include more dimensions to allow conductive heat flow in more directions, it was hoped that the convergence between experiments and models would be improved. A 2D model was built next. If this proved to be sufficiently accurate, then various beam shapes and moving beams could be considered with the model.

The 2D model allowed heat flow through the film and substrate and in one of the lateral dimensions and effectively simulates a laser beam which is infinite in one

lateral dimension whilst being finite in the other. This model once again used a distributed heat source, temperature dependent thermal parameters and convective and radiative boundary conditions on the upper and lower surfaces. The lateral surfaces utilised thermally insulated boundary conditions and the model had a width of 5 mm from the beam centre, which corresponded to the shortest width of the sample used in the experimental measurements.

The average temperature across a radius of 150 μm from the beam centre was taken from the model as it was being compared to the 3×3 pixel average (diameter) with each pixel corresponding to 100 μm. Figure 27 shows the results from the 2D numerical model.

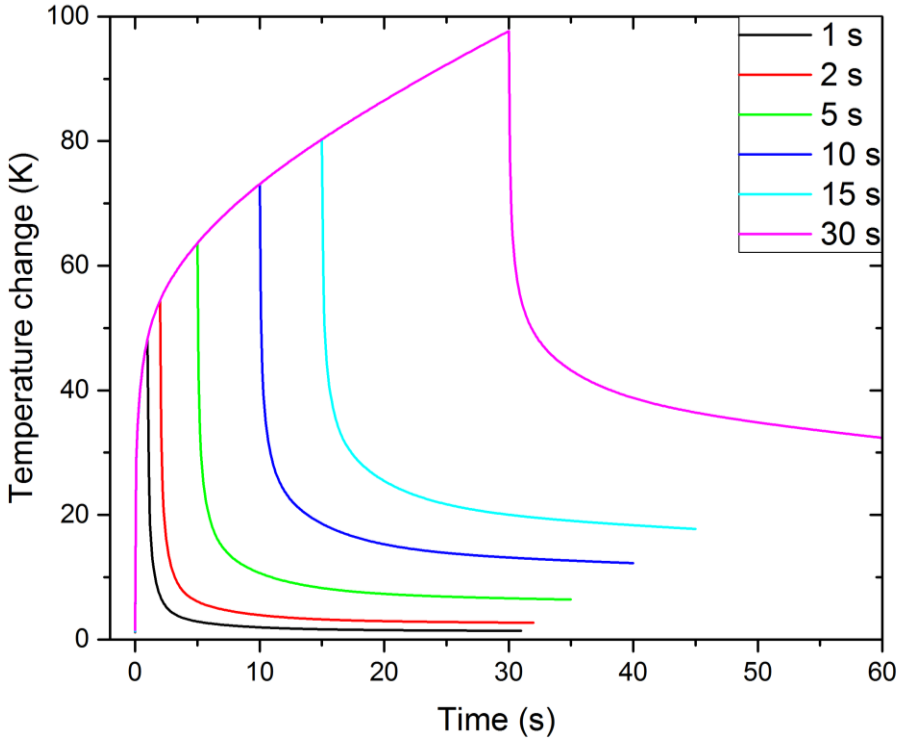

Figure 27 – Calculated temperature change of the ITO film surface due to stationary 40.5 mW HeCd laser irradiation at different dwell times using the 2D numerical model built in COMSOL 5.2a. The beam diameter was 300 μm and the model incorporated a distributed heat source, convective and radiative cooling and temperature dependent parameters where possible.

The 2D model predicted lower temperature rises compared to the previous 1D models but still did not appear to approach steady state conditions. The predicted temperature rises were still an order of magnitude higher than those measured with the IR camera. The 2D model faced the same issue that the temperature of the whole sample increased, and the cooling was then limited by the convective and radiative losses a short time after the laser was turned off. This is illustrated in figure 27 by the rapid rate of temperature decrease after the laser beam is switched off which then becomes very slow once the sample has reached approximately a constant temperature throughout. At the point where the rapidly decreasing temperature ends, the cooling is limited by radiative and convective losses.

One interesting thing about these results was that the difference between the peak temperature and the temperature at which cooling slows down significantly is approximately equal for all the different dwell times. This difference only increases by a few degrees as the dwell time is increased. This indicated that a large portion of the temperature increase at longer times (figure 27) was due to the increase in the overall temperature of the sample. This increase in the temperature of the whole sample could have been the reason that the model was not reaching a steady state temperature. This temperature increase of the whole sample was not observed experimentally and only a small volume around the beam was observed to change temperature.

Whilst the predicted temperature rises by the 2D model were around 90% lower than the 1D models predicted, there was still an order of magnitude of difference between the 2D model and the experimentally measured temperature rises. These were likely caused by the some of the same issues that the 1D models faced – most likely there are still insufficient dimensions to accurately model the

conduction losses. It was unfortunately not possible to solve a full 3D model as the beam size was much larger than the film thickness; small elements were required through the thickness of the film, but this resulted in a large number of lateral elements. This made meshing difficult as the large number of mesh elements that were required led to computational requirements which were too high to be able to solve these models. For this reason, a 2D-axisymmetric model was built which was essentially a 3D model. It utilised the symmetry of a circular beam and a cylindrical coordinate system to allow a 3D equation to be solved with much lower computation requirements. The equations are solved along the r and z coordinates and due to the cylindrical symmetry of the problem, the solution can be swept around the angle, θ. The model once again included temperature dependent thermal parameters, convective and radiative cooling from the upper and lower surfaces and a volumetric heat source. The model results were averaged in the same way as for the 2D model to consider the finite size of the pixels on the camera. The calculated temperature rise at the film surface is shown in figure 28.

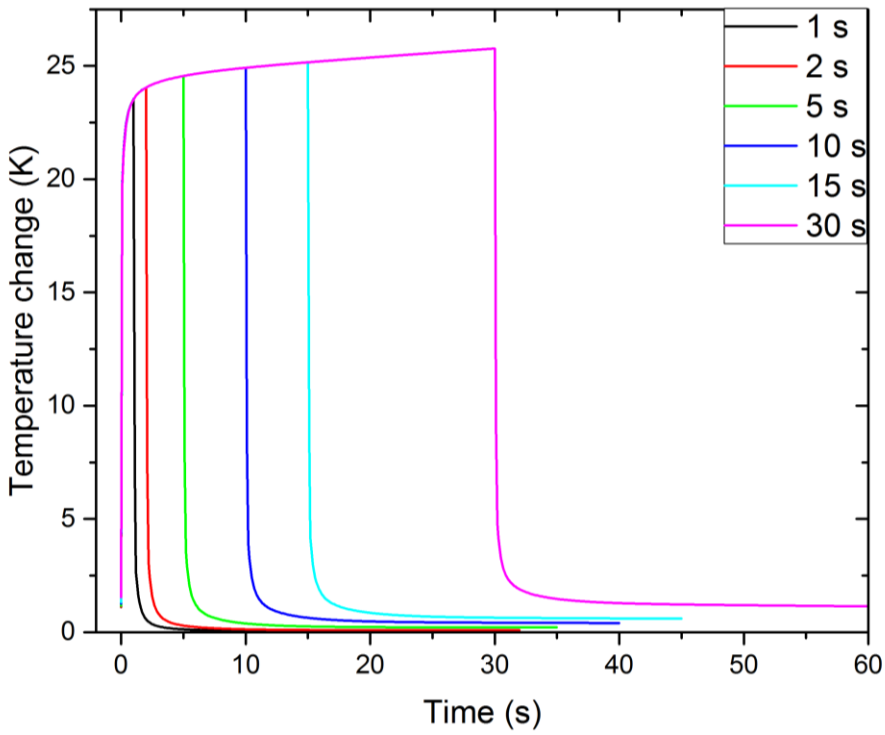

Figure 28 – Calculated temperature change of the ITO film due to stationary 40.5 mW HeCd laser irradiation at different dwell times using the 2D-axisymmetric numerical model built in COMSOL 5.2a. The beam diameter was 300 µm and the model incorporated a distributed heat source, convective and radiative cooling and temperature dependent parameters where possible.

The 2D-axisymmetric model predicted a much slower rate of temperature rise at longer times dwell, but there was still no steady state reached over the dwell times that were considered. To investigate whether a steady state temperature would ever be reached, a time independent model was created with continuous HeCd irradiation. A steady state temperature rise of 32.4 K averaged across 150 µm from the beam centre was calculated indicating that a steady state temperature would be reached. However, the temperature of the whole sample had increased by approximately 7.9 K in the steady state simulation.

The resemblance of the shape of the 2D-axisymmetric model to the thermal camera results appeared good, despite some disagreement between the

magnitudes of the temperature change. The 2D-axisymmetric result is shown alongside the thermal camera measurement in figure 29 for comparison.

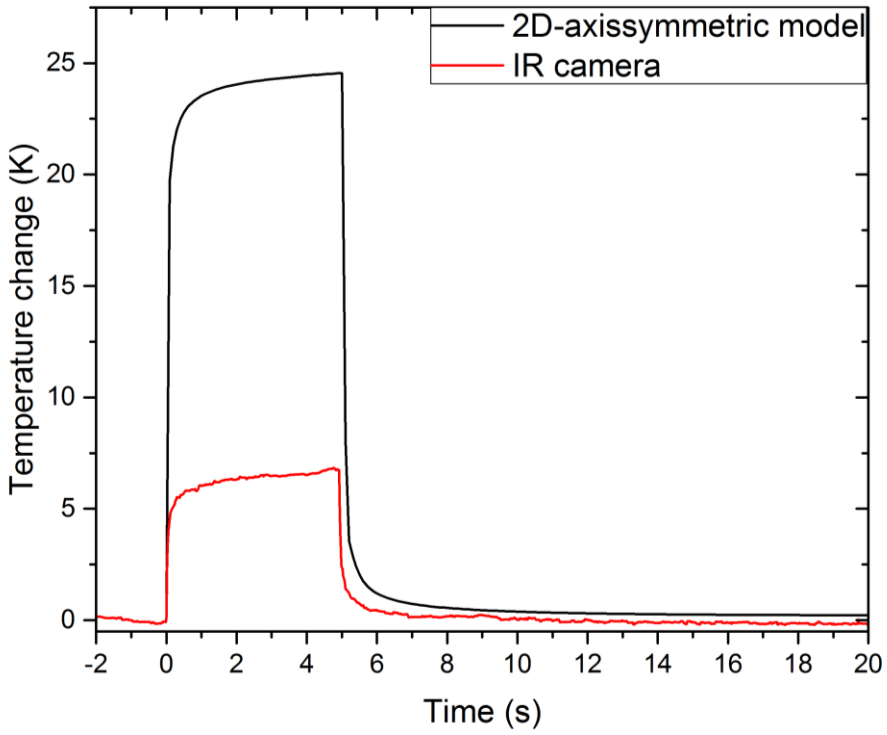

Figure 29 – Comparison of the temperature change of the ITO film predicted by the numerical 2D-axisymmetric model and that measured by the IR camera for 40.5 mW HeCd laser irradiation with a 300 μm diameter beam and a 5 second dwell time.

As the 2D-axisymmetric model was essentially a 3D model, the agreement between the model and the camera was expected to be an improvement on the 2D simulation. Whilst the shape of the heating and cooling appeared to have quite a good resemblance, the magnitude of the temperature change was inconsistent, so this was investigated further.

There were a few differences between the 2D-axisymmetric model and experimental conditions. The model assumed that the sample was cylindrical with a diameter of 10 mm (corresponding to the shortest width of the 10x32 mm sample). This meant that the sample within the model was smaller than in reality which could have limited the conductive heat flow. As previously, thermally

insulated boundary conditions were used on the lateral edges. It was particularly difficult when we assumed a cylindrical sample to estimate a heat transfer coefficient to replace these conditions with convective boundary conditions as the area to perimeter ratio was different to the real sample. It also was not appropriate to use convective or radiative boundary conditions on the lateral surfaces as the distance to the sample edge was not the same within the model as experiment. This was unfortunately a compromise that had to be made to be able to model an effectively 3D situation with feasible computational requirements. However as long as the duration of the model was shorter than the thermal diffusion time for the heat generated by the beam to reach the edge of the sample within the model (i.e.. travel 4.85 mm) then this shouldn't have been an issue. This time was calculated for both the film and substrate, the shortest of which was 45 seconds.

Whilst the model still seemed to predict a slight overall temperature increase of the whole sample that was not observed experimentally, it was minimal within this model. This appeared to be less than a 3 K average increase during a 30 second dwell time and was a maximum at 7.9 K in the stationary solution. So, whilst this increase in the temperature of the whole sample had an effect, it was unlikely to be the cause of such a large difference in the temperatures predicted by the model and those measured by the camera.

Some of the main uncertainties within the models arose from the thermal parameters that were estimated. To determine the effect of these estimated parameters, it was decided to explore this poorly defined parameter space. The uncertainties in this area arose from the fact that a packing density of around 74% was assumed because it allowed a simple model geometry to be used to estimate the thermal conductivity of the composite material. The ITO content was likely to be higher as the film consisted of nanoparticles of varying sizes which would allow

for better filling of voids within the film. This would also have affected the thermal conductivity and density that were calculated.

Initially, the thermal conductivity in the model was changed to that of a continuous ITO film rather than the nanoparticulate film to investigate the role that this played. The predicted temperature rise from the 2D-axisymmetric model for a 5 second dwell time using the bulk ITO thermal conductivity is shown in figure 30 alongside the original model results.

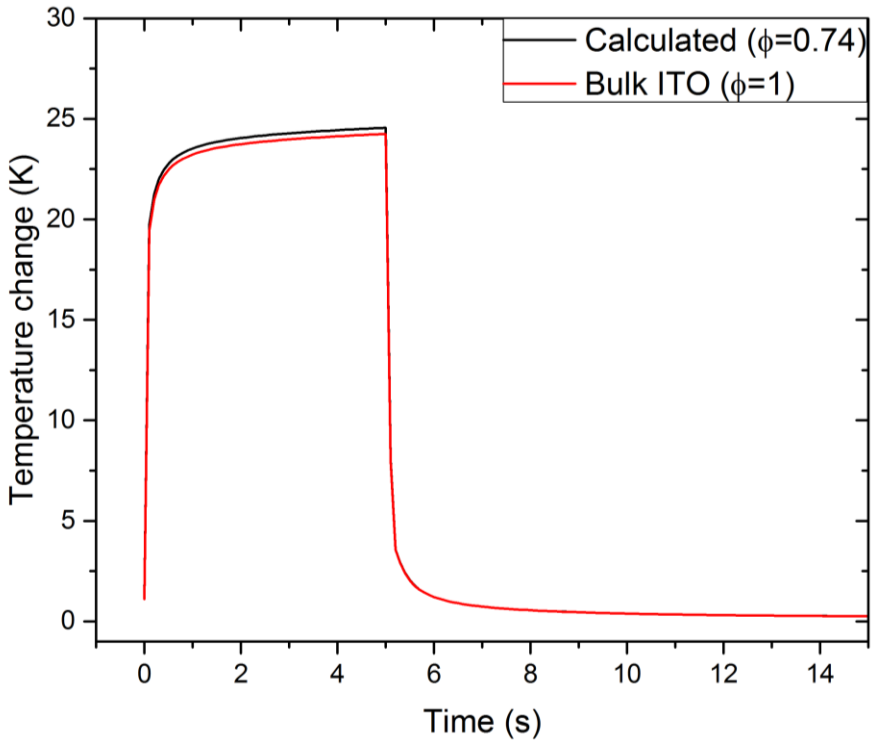

Figure 30 – Comparison of calculated temperature change of the ITO film surface due to 40.5 mW HeCd irradiation with a 300 μm diameter beam using the 2D-axisymmetric numerical model with the estimated composite thermal conductivity (ITO fraction, ϕ=0.74) and bulk ITO thermal conductivity (ϕ=1).

Whilst there was a very small reduction in the temperature of <1 K from adjusting the thermal conductivity, the temperature change was insignificant, so this was not explored further, and it was decided to probe the effects of the density and heat capacity.

It was unclear what percentage ITO content the film contained therefore different percentages were investigated: 80, 90 and 100%. These values were calculated using volumetric weighting of each parameter relative to the content of the sample. These results were plotted alongside the results from the original model and were almost identical and visually indistinguishable from the graphs. This showed that the model was insensitive to changes in the thermal properties tied to the ITO content over the ranges considered here.

It was surprising that the thermal parameters of the film had such a small effect. Rather than just tying the parameters to the ITO content it was decided to try changing these parameters by an order of magnitude larger or smaller to investigate the importance of these parameters further. Even making such drastic changes to the thermal properties of the film made very little change to the predicted temperatures changes. All the changes were comparable to those illustrated in figure 30 indicating that the thermal parameters of the film did not strongly impact the temperature rise in this case.

There were also some uncertainties associated with the optical properties of the ITO film. It may have been possible that the reflectivity was underestimated due to uncertainties in the real part of the refractive index. However, it was expected that these would not be too significant as the overall transmittance at 350 nm and above was high indicating quite a low reflectivity. Moving further into the UV led to small changes in the refractive index but it was unlikely that these would be large enough to alter the energy loading enough to account for the discrepancies with the experimental results. The energy loading was mainly associated with the imaginary part of the refractive index, k. However, it had been shown that light scattering was negligible, and we had confidence in the method used to calculate the absorption coefficient.

There were also uncertainties associated with the thermal camera measurements particularly as the temperature was close to ambient. The thermal sensitivity (defined as the noise equivalent temperature difference) on the camera was <0.05°C at 30°C which meant that operating at just above room temperature should not have been an issue. However, much of the time, the sample was below 30°C and no thermal sensitivity was provided within this region. The accuracy of the temperature measurements for the camera was given by the manufacturer as ±5 K or ±5% of the reading which was substantial compared to the measured values. This uncertainty was also doubled as the initial temperature was taken from the camera measurement to calculate the temperature change.

In addition to this, because the beam was so small, only 9 pixels were being used on the camera. Any issues with calibration relating to these pixels could have drastically affected the temperatures that were measured.

The emissivity of the sample was only measured confidently to 1 significant figure at 0.6. Slight changes in the emissivity changed the temperature that was calculated by the camera. A change in the emissivity of 0.1 led to a difference in the temperature change of a no greater than 5 K, however when working with such small temperature rises of <10 K, this is a significant percentage of the reading.

There were also other subtler issues associated with comparing the results of the models to the thermal camera measurements. It had been assumed that the temperature being measured by the camera was that at the surface of the sample. In reality, the IR radiation was coming from different depths within the sample including the substrate. This intensity of the radiation originating from different depths within the sample would depend on the absorption of the film and

substrate at the IR wavelengths being emitted. Unfortunately, this data was not available, and it was not possible to accurately measure these values for our materials at the wavelengths of interest. If it was possible to observe the temperature at the film surface with the camera, the measured temperature change would have been higher.

In the light of not finding agreement between calculated and measured temperature changes, the data was scaled to compare the shape of the temperature rise in time and space (figures 31 and 32). Both figures show remarkably good agreement.

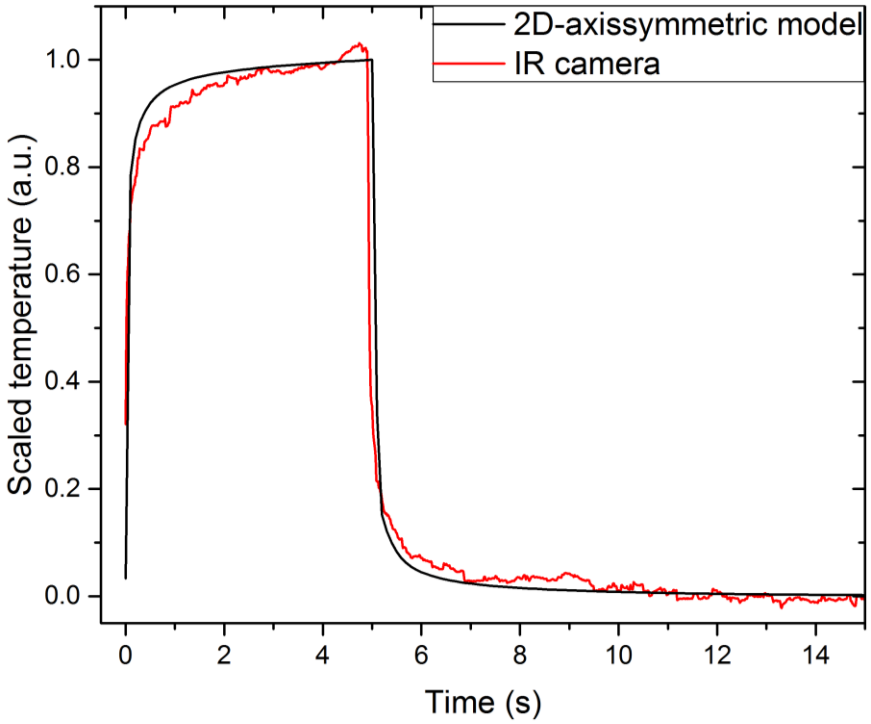

Figure 31 – Scaled temperature profiles for stationary 40.5 mW HeCd laser irradiation from the numerical 2D-axisymmetric model and IR camera measurements with a dwell time of 5 seconds.

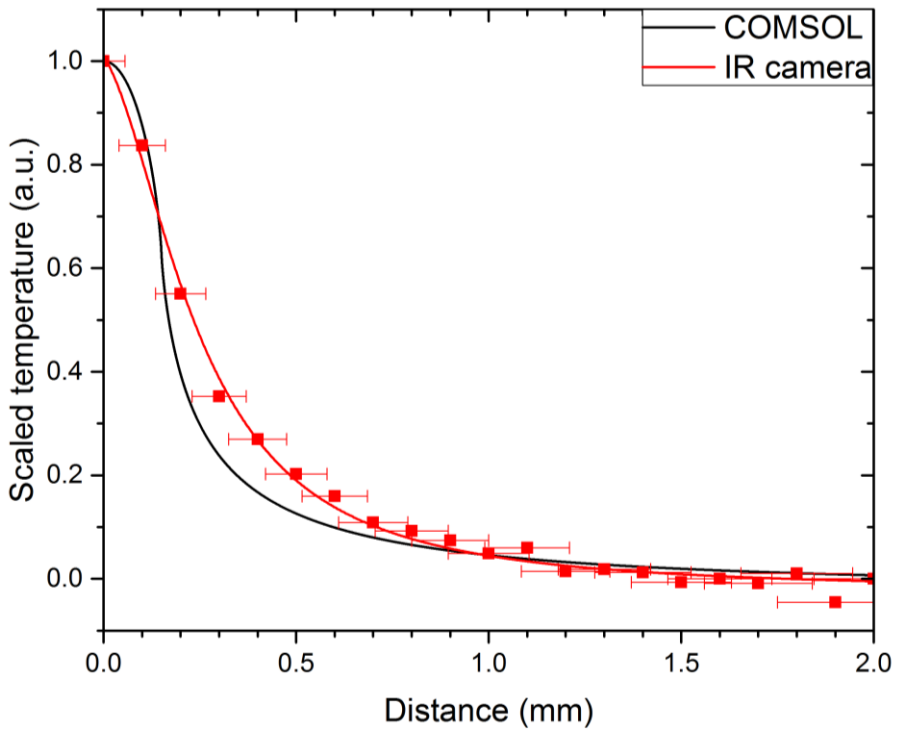

Figure 32 – Scaled spatial temperature profile for 40.5 mW HeCd laser irradiation from 2D-axisymmetric model and IR camera measurements at the end of the 5 second dwell time.

The sample length (27 mm) was used to calculate the distance per pixel on the camera. The uncertainty in the sample length and blurriness of the sample edges on the camera were used to determine the uncertainty in distance per pixel in figure 32 of ±5 μm·px^{-1}. An additional uncertainty arose because it was not possible to determine whether the centre of the beam was located in the centre or at the edge of the pixel leading to a total uncertainty of ±(5 μm·px^{-1} + 50 μm).

In summary, it was found that models with fewer dimensions (1D, 2D) failed to accurately model the conduction of heat away from the irradiated zone and this led to a large temperature build-up within sample exceeding that that was observed experimentally by a factor of over 100 in the worst cases. At long irradiation times (i.e. when the irradiation time exceeds the time for heat to diffuse away from where it was generated (the heat affected zone)), conductive cooling

rates become more important. At much shorter times, not much conduction occurs so they have less of an impact. The thermal diffusion time for the generated heat to travel one beam radius was calculated using equation 41 and found to be 100 ms in the film and 40 ms in the substrate. As dwell times were at least 10 times longer than this, accurate conductive cooling rates were vital in determining the peak temperature rise. Lower dimensional models had much lower cooling rates, primarily due to the reduced dimensions in which conduction could occur, hence the temperature rises were vastly overestimated.

The 2D-axissymmetric model had much more realistic cooling, allowing for conduction in three dimensions, and showed a good resemblance to the profile of the temperature rise but the magnitude of the rise was over 4 times higher than was measured experimentally. This was an overestimation of around 18 K. It was demonstrated that the thermal properties of the ITO film, which were relatively uncertain, had a negligible effect on the predicted temperature rise. However, there were relatively large uncertainties for the experimentally determined temperature rise. An uncertainty of 10 K arose from the manufacturer's specifications of the IR camera alone, with additional uncertainties arising from the emissivity calculations, the small size of the laser spot and the depth from within the sample that the detected IR irradiation originated; although it was difficult to quantify some of these. Consequently, it was determined that the 2D-axissymmetric model showed the most promise in being able to accurately predict the laser-induced temperature rise for heating of a thin film system with continuous wave irradiation with excellent agreement of the shape of the temperature rise. A laser with a higher output power to generate larger temperature rises and allow for a larger spot size would allow the percentage uncertainties in the experimentally measured temperature rises to be drastically

reduced and could provide more confidence in the magnitude of the predicted temperature rise.

5.2. Moving continuous wave HeCd laser

Moving beams were investigated with all experimental conditions identical to that for the stationary beam. Three different velocities were investigated: 1.0, 1.5 and 2.0 mm·s^{-1}, with the beam travelling a total distance of 15 mm. Experimentally, moving the beam was achieved by moving the sample with a translation stage but it was easier within the modelling to work in the reference frame of the sample. The 1D semi-analytical, and the 1D & 2D-axisymmetric numerical models could not model moving beams as the symmetry of the system is broken, so only the 2D model was used.

The temperature across a 3×3 pixel area measured by the IR camera is shown in figure 33.

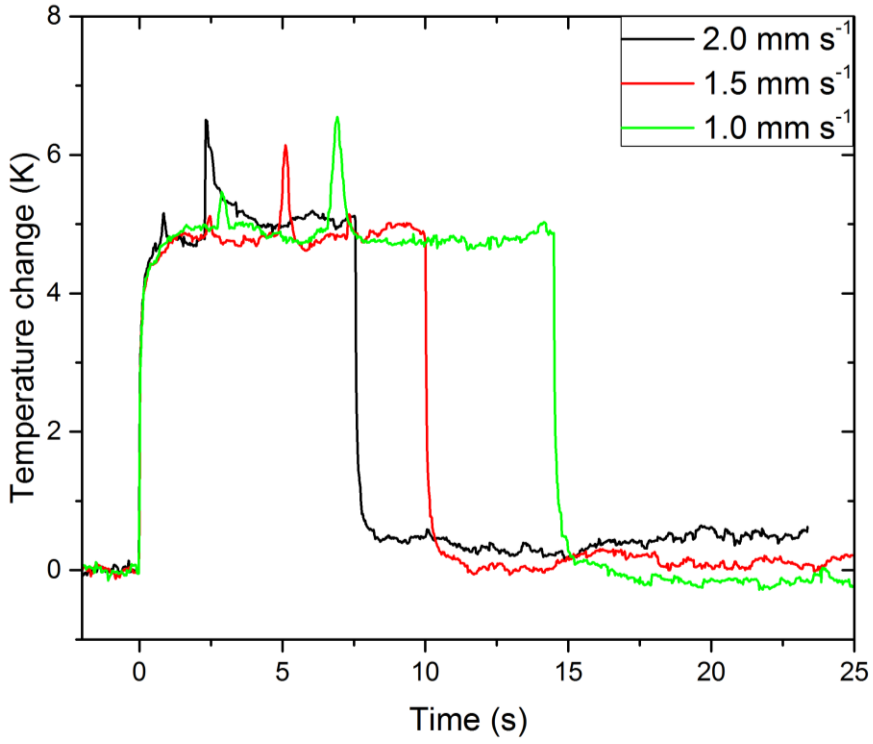

Figure 33 – Measured temperature change of the ITO film due a moving HeCd laser. The incident power was 40.5 mW with a 300 μm diameter uniform circular beam. The sample was translated at different velocities and moved a total distance of 15 mm throughout. The large spikes were associated with contaminants on the sample.

After processing the results, it was observed that a spike in the temperature occurred at two points along the beam path. These spikes occurred at consistent places in space (approximately 2.5 and 7.0 mm across the sample) and it was therefore determined that they were likely associated with contaminants on the sample and the effects could be ignored. The thermal camera showed that the temperature rise of sample with the moving beam was slightly lower than that of the stationary beam as expected. A steady state temperature was reached quite within 2 seconds, followed by a rapid cooling of the sample once the laser beam was switched off. A snapshot from the IR camera during the 2 $mm \cdot s^{-1}$ measurement is shown in figure 34 with the inset showing the temperature profile along the blue line. The beam is moving towards the right-hand side of the figure.

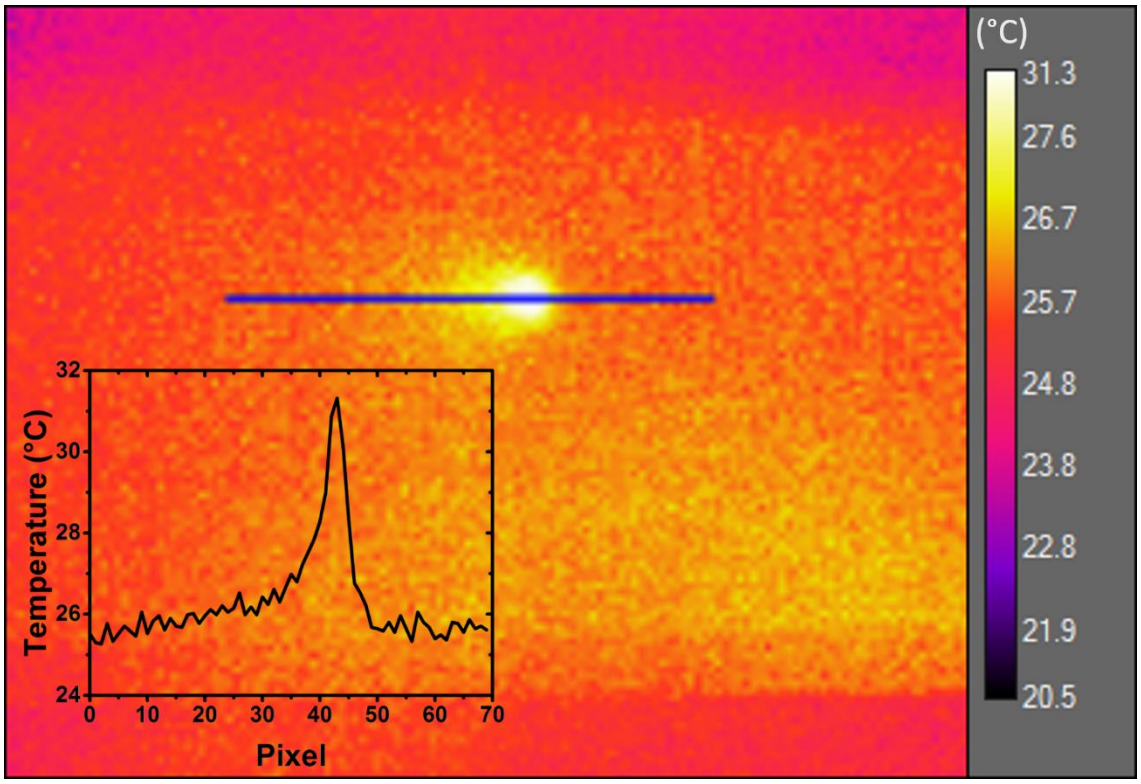

Figure 34 – 2D map of the temperature measured by IR camera during 40.5 mW HeCd irradiation of the ITO sample with a 300 µm diameter circular spot moving across the sample at a velocity of 2.0 $mm \cdot s^{-1}$ to the right. The inset shows the spatial profile across the blue line.

The temperature predicted by the model was once again averaged across the beam diameter for comparison with the thermal camera measurements. As this was a moving beam and the temperature rise was not symmetrical along the direction of travel, a 300 μm spatial average was taken across the beam diameter rather than averaging across the beam radius. It was not easily possible within the software to calculate this average exactly at every time step due to the beam having different coordinates throughout the simulation. Therefore, the temperature change was sampled at 5 μm intervals across the whole sample surface at each time step and exported. A script was written in Wolfram Mathematica 10.2 to select the coordinates corresponding to the beam location and average across these points for each time step. After the beam had stopped moving, the averages were calculated at the beam's end point.

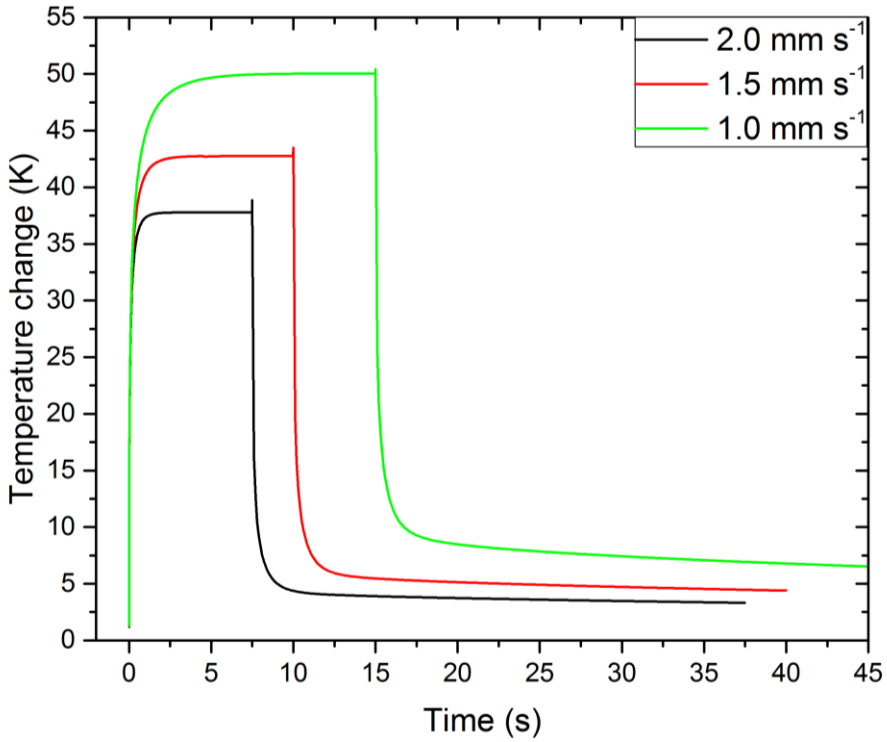

Figure 35 – Temperature change of the ITO film surface due to a moving HeCd laser calculated using the 2D numerical model at three different velocities across a distance of 15 mm. A power of 40.5 mW was used with a 300 µm diameter uniform circular beam. The model included a distributed heat source and radiative and convective cooling. Temperature dependent thermal parameters were used were possible (see section 4.5).

Once again, the 2D model predicted temperature rises an order of magnitude larger than the thermal camera measured (figure 35). However, unlike for the 2D model of the stationary beam, the temperature did not keep on rising indefinitely and a steady state temperature was reached. It is worth noting that the sample within the model was larger than previous models at 30 mm wide (corresponding to the longer side of the sample) whereas the previous models used a 10 mm wide sample (corresponding to the shorter edge). The longer side was used in this model as the beam was travelling in this direction hence a larger geometry was required to allow for this beam translation to be incorporated. This meant that compared to previous models for the stationary beam there was a larger area for the heat to diffuse into. This likely also contributed to the much smaller

temperature increase of the whole sample compared to the 2D model of the stationary beam. The sample size was therefore believed to be at least partly responsible for the model approaching steady state conditions as most of the temperature increase at long dwell times for the stationary beam had been due to the temperature increase of the whole sample.

Nevertheless, the model was overestimating the temperature by an order of magnitude when compared to the thermal camera measurements. This could not be explained by the uncertainties discussed for the stationary beam as the magnitude of difference between the model and experiment was much larger in this case than between the 2D-axisymmetric model and the IR camera for the stationary beam. It had been shown that the 2D model was insufficient to accurately estimate the temperature rise within the sample for the stationary beam due to the limited dimensions in which the conduction was modelled. For this reason and with such a large difference between the camera and model results, it was determined that the 2D model could not be used to accurately predict temperature rises for the moving continuous wave laser. Whilst the overall increase in the sample was much smaller within this model, the lack of conduction in three dimensions would still have affected the heat transport away from the beam and this was likely to be the cause of such a large overestimation of the temperature rise. Unfortunately, a 3D model could not be built for the moving beam as the computational requirements were too high and a 2D-axisymmetric model could not be used due to the loss of symmetry associated with the movement.

5.3. Stationary pulsed XeCl laser

As one of the main interests within this work was to utilise pulsed lasers to modify the thin film coatings without damaging the underlying substrate, models incorporating a 308 nm XeCl excimer laser were investigated. As previously, the results of the models were compared to thermal camera measurements. To take these measurements the sample was mounted to the stage as before and the laser beam was directed through a circular mask and imaged onto a stage to form a 1 mm, top-hat circular beam. The full setup is shown in figure 36. The beam shape and size were measured by irradiating thermal paper with several pulses and measuring the resultant mark under an optical microscope.

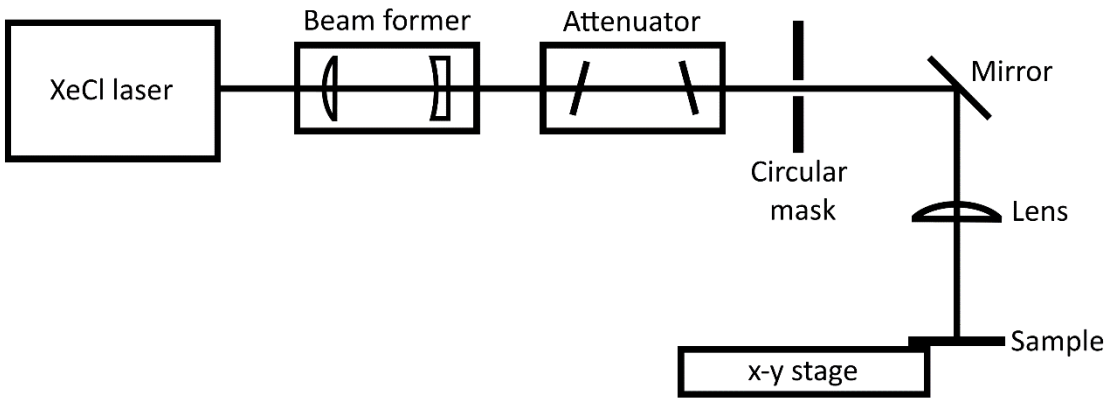

Figure 36 – Optical setup consisting of a Lumonics 500 series excimer XeCl laser, a beam former with two cylindrical UV fused silica lenses, an attenuator with two CaF windows, a 1 mm circular mask, a dielectric mirror and a 150 mm focal length UV fused silica lens. This formed a 1 mm diameter circular spot on the sample which was mounted to the edge of an x-y translation stage.

The temporal profile of the laser beam intensity was measured using an FND100Q photodetector with a bandwidth of 300 MHz and corresponding rise time of approximately 1 ns. This was connected with a 50 Ω termination into an Agilent DSO-X 3052A 500 MHz bandwidth oscilloscope. To avoid saturation, the

light from the laser was scattered into the detector and the response of a single pulse was measured (figure 37). This exact temporal pulse shape was incorporated into the COMSOL models, but for the simpler semi-analytical model a rectangular pulse with a 4.125 ns duration was used instead – corresponding to the full width at half maximum of the real pulse shape.

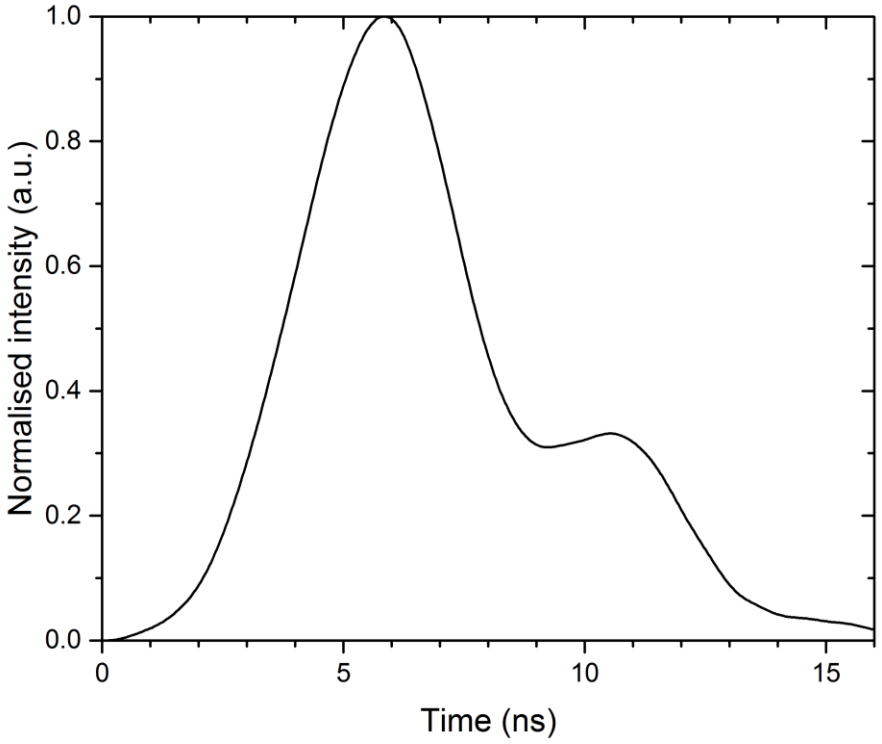

Figure 37 – Temporal shape of XeCl laser pulse intensity measured by scattering the laser light into a 1 ns rise time FND100Q photodetector with a 50 Ω termination into a 500 MHz Agilent DSO-X 3052A oscilloscope.

An attenuator, consisting of two angled CaF windows, was used to control the fluence of the laser pulses. Damage was observed to occur to the films at fluences above approximately 75 $mJ \cdot cm^{-2}$, so a lower fluence of 50 $mJ \cdot cm^{-2}$ was selected for these experiments.

The issue with validating the model for such a short pulse length is that it is not possible to resolve these timescales with the thermal camera. Because of this, rather than investigating the peak temperature it was decided to compare the

residual temperature that builds up during repetitive pulsed irradiation with the temperature that is measured by the thermal camera.

The sample was irradiated with a stationary 1 mm diameter circular beam with a fluence of 50 $mJ \cdot cm^{-2}$ per pulse and a pulse repetition frequency of 50 Hz for three different durations of 2, 5 and 10 seconds. There were issues modelling the longer durations as the time steps during the pulse had to be very small to properly resolve the shape (0.1 ns steps during the pulse). This meant that a large number of time steps were required which increased the computational time required to solve the models to the point where it was impractical (estimated to be over 50 days for the 2D-axisymmetric model for 10 seconds of irradiation). For this reason, only the two second duration was modelled.

The thermal camera measurements showed that the XeCl laser irradiation produced very small temperature increases within the sample (figure 38). This small temperature rise was expected from the camera as the frame rate of the camera was limited to 60 Hz and the rapid heating from the laser pulses was expected to occur on much shorter timescales.

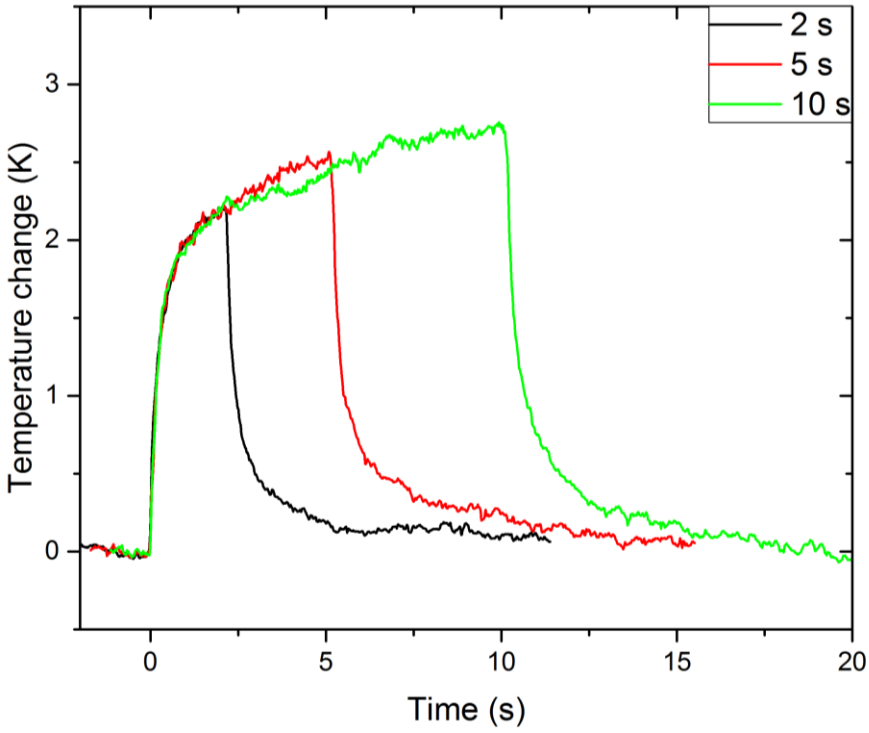

Figure 38 – Measured temperature change of the ITO film due to XeCl irradiation at 50 Hz with a fluence of 50 mJ·cm^{-2} and 1 mm diameter uniform circular beam. The sample was exposed for different durations of 2, 5 and 10 seconds after which the cooling was observed.

As previously, the simplest model was considered first: the 1D semi-analytical model. This model only had rectangular pulses implemented into it, so the FWHM of the experimentally measured pulse was used initially with a length of 4.125 ns. Only a single pulse could be considered with this model. The results are shown in figure 39.

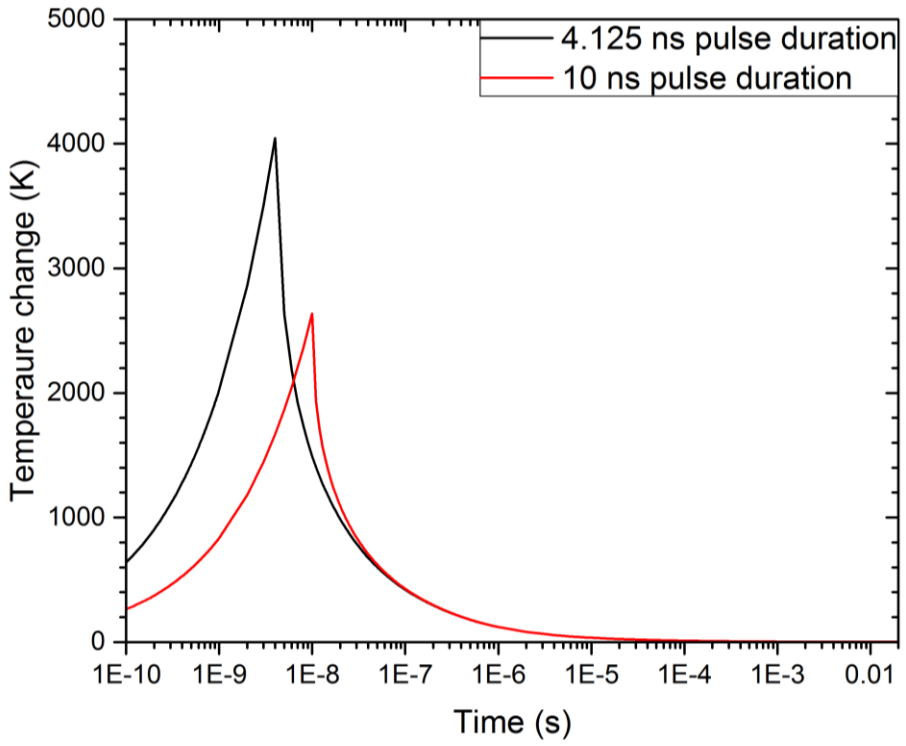

Figure 39 – Temperature change of the ITO film surface due to a single 50 mJ·cm^{-2} XeCl laser pulse calculated using the 1D semi-analytical model of El-Adawi et al.[36] *The laser pulse was rectangular in time two pulse lengths of 4.125 ns and 10 ns were corresponding to the FWHM of the real pulse shape and a longer duration for comparison as discussed below. A logarithmic horizontal axis has been used as the heating is very rapid (nanosecond time scales) whereas the cooling occurs over microseconds.*

As the temperature increase was much larger than was realistic (over 4000 K), it was decided to also consider the effect of a longer duration pulse as the FWHM only included the first part of the pulse and did not take into account the shoulder (figure 37). However, even with a 10 ns pulse length, the temperature rise that was predicted was still unrealistic and would have led to melting or evaporation of the material which was not observed experimentally. For these reasons, this model was determined not to be reliable for predicting the temperature rise under these conditions.

The numerical 1D model was considered next. The model was setup as previously described for the HeCd system but with the real XeCl pulse shape

incorporated. The laser pulse train had a repetition rate of 50 Hz and the sample was exposed for 2 seconds. The subsequent cooling was followed in the model for a further 28 seconds.

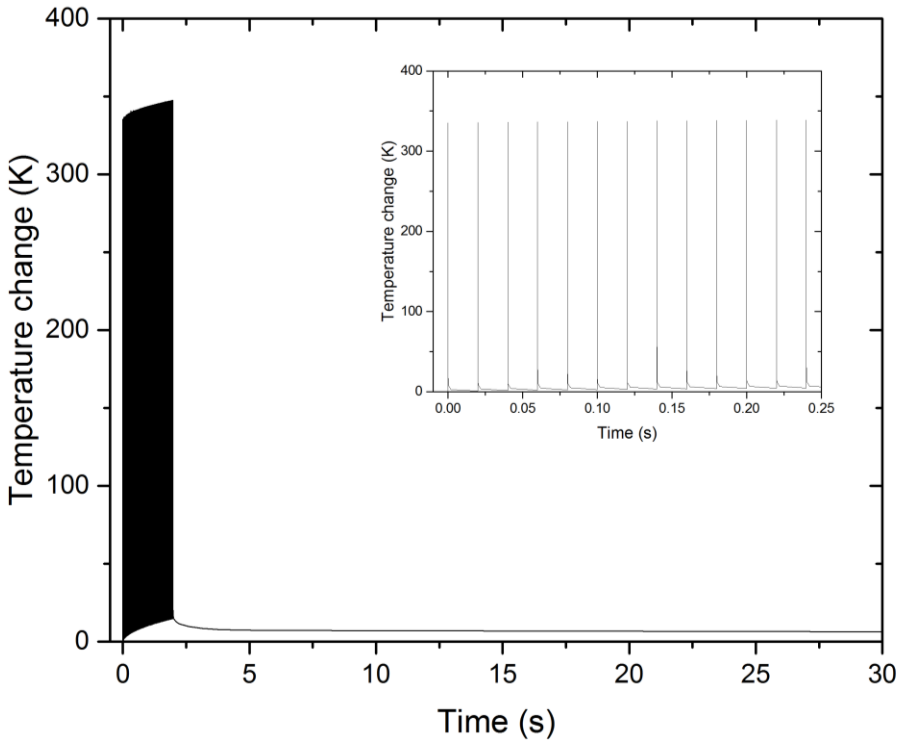

Figure 40 – Temperature change of the ITO film surface due to 2 seconds of XeCl laser irradiation using the 1D numerical model built in COMSOL 5.2a. The pulse repetition rate was 50 Hz with a fluence of 50 mJ·cm^{-2} per pulse. The model incorporated the real pulse shape and included a distributed heat source and radiative and convective losses. Temperature dependent parameters were used where possible. The inset shows the first 0.25 seconds of irradiation.

The results shown in figure 40 predict a temperature rise of just over 330 K per pulse. The solid black area on the graph contains 100 individual pulses. The peak temperature slowly built up over time indicating that that sample did not fully cool between each pulse according to this model. This agrees with the thermal camera results but to fully explore this, the temperature just before each new pulse (the residual temperature) was plotted for comparison with the thermal camera data.

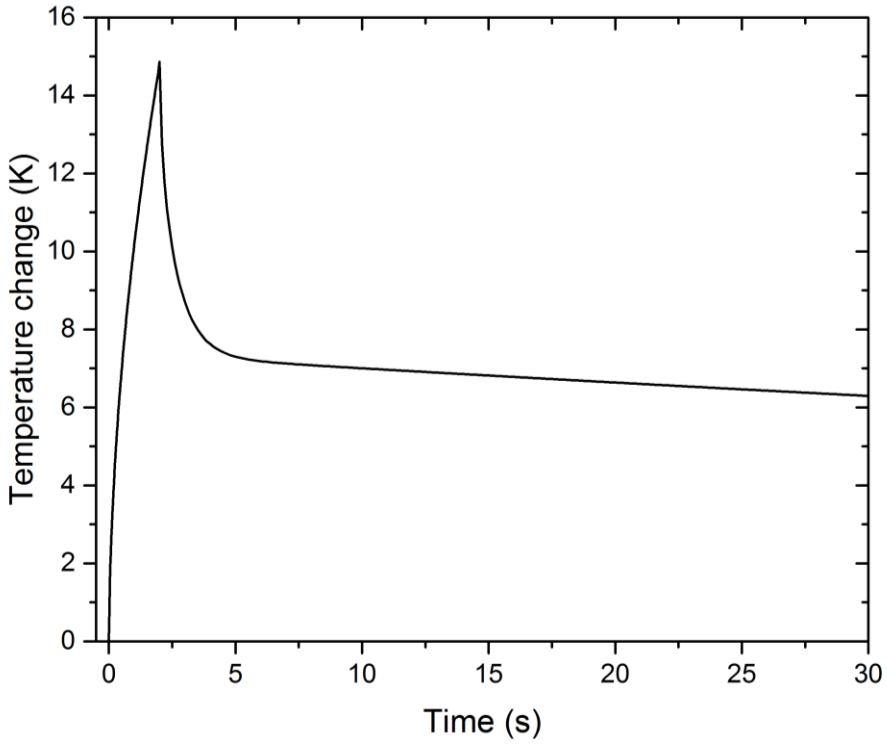

Figure 41 – Residual temperature change of the ITO film surface due to 2 seconds of XeCl laser irradiation calculated using the 1D numerical model built in COMSOL 5.2a. The conditions are identical to those in figure 40.

This predicted a significantly higher residual temperature than was measured experimentally however the difference in the order of magnitude was not as large as observed for the 1D CW laser model, so it was possible that this was associated with some of the previously discussed issues including the various uncertainties within the thermo-mechanical properties and issues relating to the thermal camera measurements. The sample cooling was however once again limited by convection and radiation shortly after the heating stopped and the sample had reached an approximately constant temperature throughout of around 7 K. This indicated that further dimensions were likely necessary as was the case for the continuous wave stationary HeCd models discussed previously.

A numerical 2D model was therefore explored next with the results shown in figure 42.

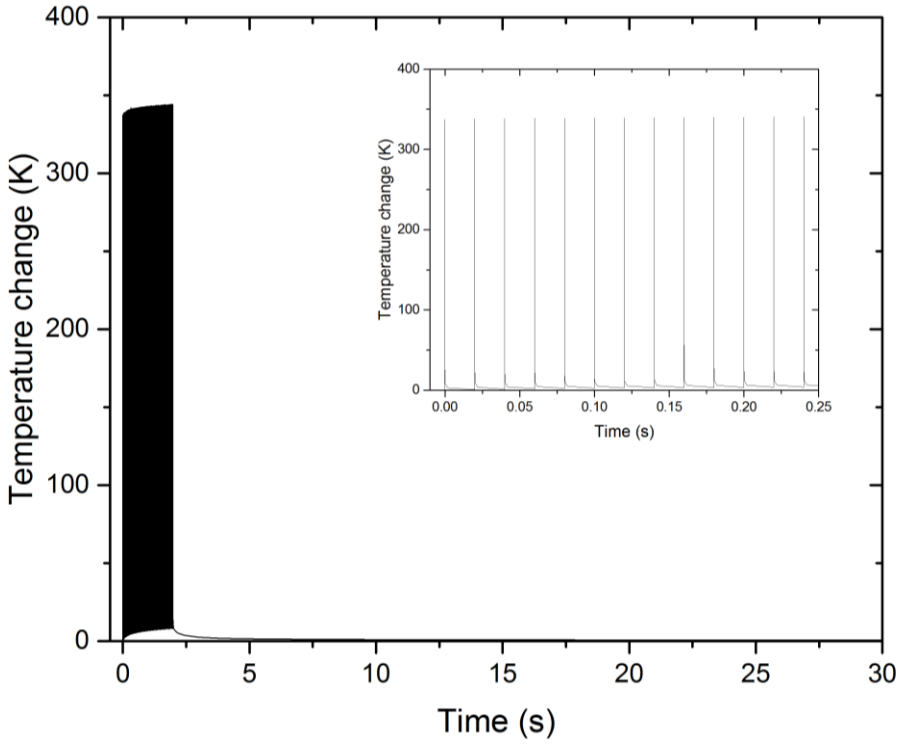

Figure 42 – Temperature change of the ITO film surface due to 2 seconds of XeCl laser irradiation using the 2D numerical model built in COMSOL 5.2a. The pulse repetition rate was 50 Hz with a fluence of 50 mJ·cm^{-2} per pulse and 1 mm diameter uniform circular beam. The model incorporated the real pulse shape and included a distributed heat source and radiative and convective losses. Temperature dependent parameters were used where possible. The inset shows the first 0.25 seconds of irradiation.

In contrast to what was observed with the continuous wave stationary HeCd laser model, there was no significant difference observed in the peak temperature rise that was predicted by the 2D model and the 1D model. The temperature increase of the whole sample was reduced indicating that the additional cooling via lateral conduction did contribute to the results. The residual temperature increase for the 2D model was smaller than that predicted by the 1D model and is shown in figure 43.

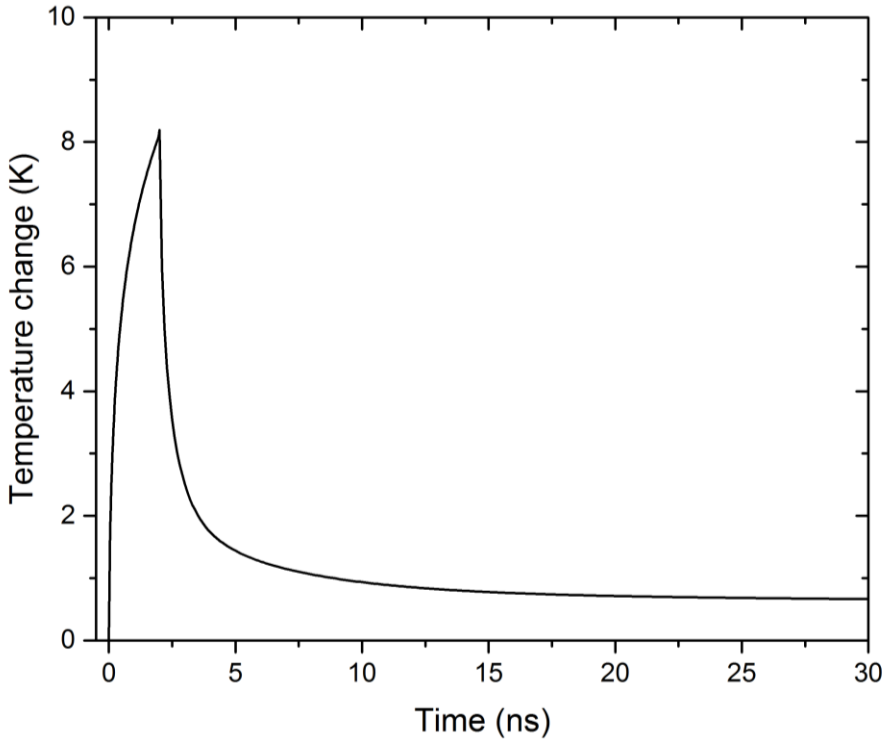

Figure 43 – Residual temperature change of the ITO film surface due to 2 seconds of XeCl laser irradiation calculated using the 2D numerical model built in COMSOL 5.2a. The conditions are identical to those in figure 42.

To get a complete picture, a 2D-axisymmetric model was also plotted (figure 45). Once again, the temperature rise from each pulse was almost identical to the two previous numerical models. As expected, the 2D-axisymmetric model predicted a further reduced temperature build up between the pulses. This led to an overall smaller residual temperature rise and the temperature increase across the whole sample was significantly lower. This was attributed to the more realistic modelling of the conduction. The 2D-axissymmetric model allowed for conduction in three dimensions rather than being limited to one or two in the case of the 1D and 2D models. This led to an increased rate of heat dissipation which allowed the sample to cool more between pulses.

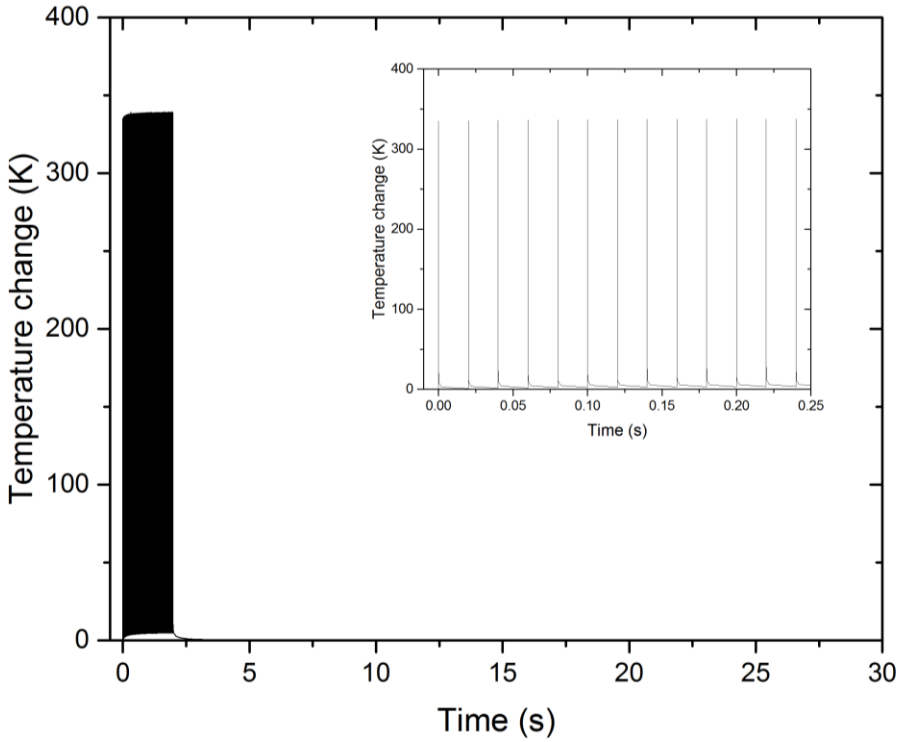

Figure 44 – Temperature change of the ITO film surface due to 2 seconds of XeCl laser irradiation using the 2D-axisymmetric numerical model built in COMSOL 5.2a. The pulse repetition rate was 50 Hz with a fluence of 50 mJ·cm^{-2} per pulse and 1 mm diameter uniform circular beam. The model incorporated the real pulse shape and included a distributed heat source and radiative and convective losses. Temperature dependent parameters were used where possible. The inset shows the first 0.25 seconds of irradiation.

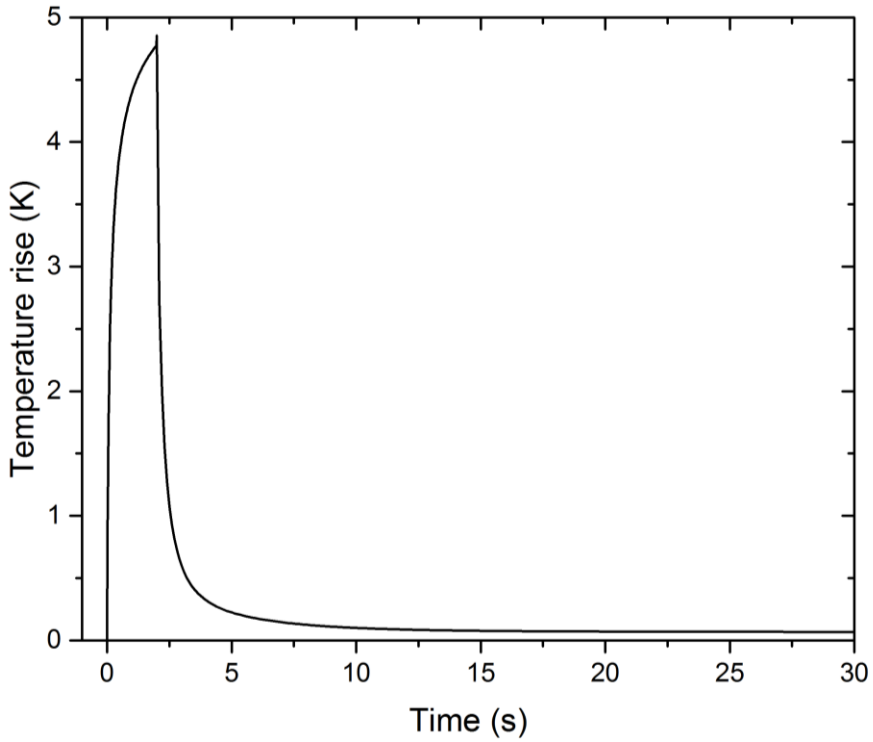

Figure 45 – Residual temperature change of the ITO film surface due to 2 seconds of XeCl laser irradiation calculated using the 2D-axisymmetric numerical model built in COMSOL 5.2a. The conditions are identical to those in figure 44.

For a full comparison between the different models, the temperature rise due to a single pulse was plotted for each of the numerical models (figure 46). The semi-analytical model was not included due to the unrealistic nature of the results.

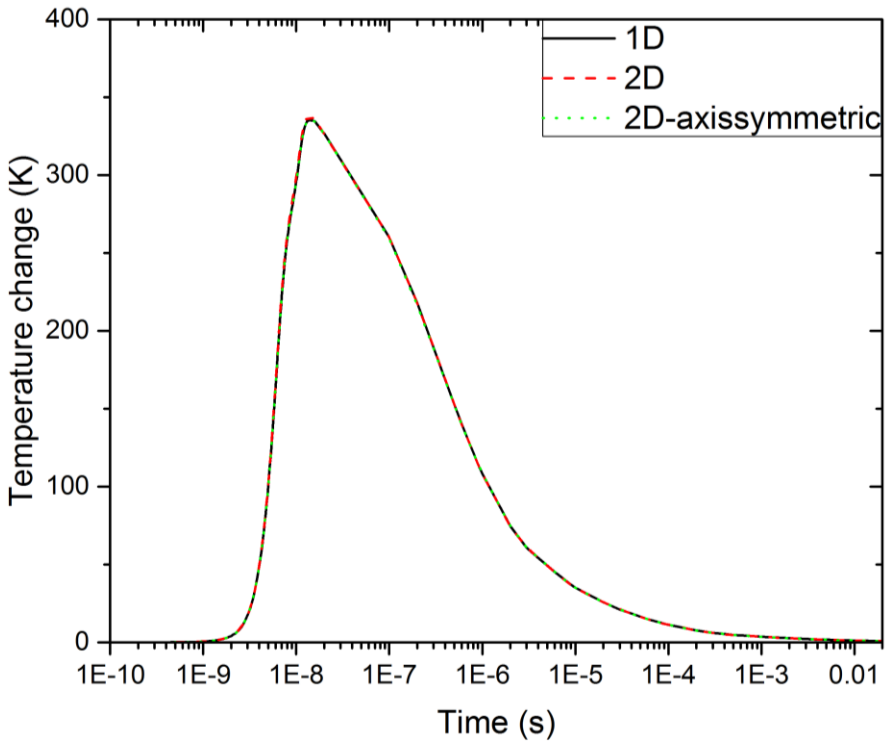

Figure 46 – Comparison of the calculated temperature changes of the ITO film surface due to a single XeCl pulse using the different numerical models built in COMSOL 5.2a. A 50 mJ·cm^{-2} pulse was used with a 1 mm diameter uniform circular beam and the real temporal pulse shape.

These predicted temperature rises due to a single pulse show almost exact agreement for the numerical models. This was remarkable when compared to the results from the continuous wave laser, where all of the numerical models predicted substantially different temperature rises, and seemed to indicate that the models were equally valid at predicting the temperature rise within the sample due to a single pulse. Whether the magnitude of the values predicted by the models is correct is still uncertain however, but this is due to the uncertainty in the parameters used within the models and some issues with the thermal camera measurements as discussed previously.

To determine whether the models were valid for multiple pulses, the residual temperatures were all plotted together alongside the IR camera results (figure 47).

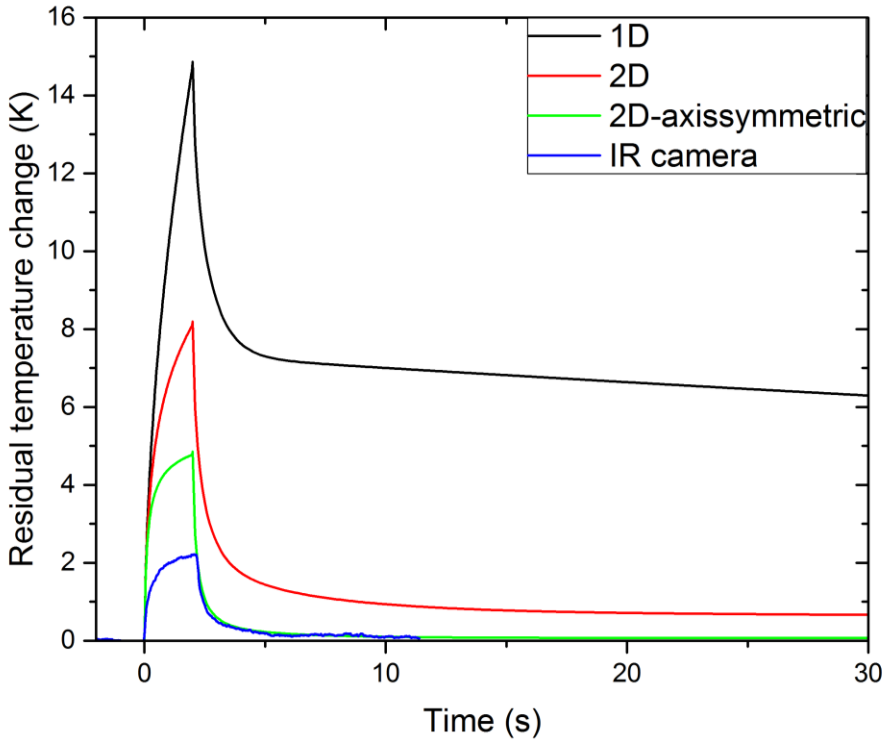

Figure 47 – Comparison of the residual temperature rises due to 2 seconds of XeCl irradiation using the different numerical models built in COMSOL 5.2a. The pulse repetition rate was 50 Hz with a fluence of 50 mJ·cm^{-2} per pulse and 1 mm diameter uniform circular beam and the real temporal pulse shape. The IR camera measurements are included for comparison.

Figure 47 illustrates that all the models overestimated the residual temperature increase. Based on the previous results this was not unexpected and was attributed to the same issues discussed previously and was largely associated to the uncertainties within both the material parameters and the thermal camera measurements. However, it once again demonstrated that the 2D axis-symmetric model predicted the closest results to the thermal camera due to the increased conductive heat flow.

The effects of the thermal parameters were explored once again in the same way as they were for the HeCd model by changing each parameter individually by 0.1 and 10 times. In the case of the XeCl laser, this produced considerable changes in the predicted temperature rise. This indicated that knowing the thermal parameters of the film accurately was vital for predicting the temperature rise with short pulsed lasers as well as knowing the optical parameters accurately.

Whilst the residual temperature provides the insight necessary to validate the models, for a pulsed laser like this, it is unlikely to be really of interest with regards to the processing of materials unless it becomes large. The parameter that controls the process the most is the peak temperature and the duration of the temperature rise. It is important to be able to predict this accurately, and all these models give approximately the same temperature rise for a single pulse at this repetition rate. Therefore, it could be argued that if the pulse repetition frequency is low enough that the residual temperature rise is insignificant, the simplest 1D model would sufficiently predict the temperature rise whilst being much quicker than the more complex models. This is likely to change depending on the pulse length and material of interest, but by running a simple numerical 1D model first for the duration of the pulse period the suitability of the 1D model could be determined. If the temperature rise at the end of the model is insignificant, the 1D model will likely suffice to predict the temperature rise within the thin film system.

6. Conclusions

Models have been constructed to predict the laser-induced temperature rise within a nanoparticulate film on a substrate for continuous wave and nanosecond pulsed lasers. These models were compared to experimental thermal camera measurements to determine the validity of the different models. Four different model geometries were compared, a semi-analytical 1D model and 1D, 2D and 2D-axisymmetric finite element numerical models. The thermal properties used within these models for the nanoparticulate film were approximated with volumetric weighting used to calculate the density and heat capacity. The optical properties were calculated from the transmission spectrum of the ITO coated substrate. The Swanepoel method was used to determine the real part of the refractive index and the Beer-Lambert absorption considering multiple reflections was used to calculate the imaginary component. It was also demonstrated that the films didn't significantly scatter the light in the UV region of the spectrum (325 nm). A finite element simulation was built to calculate an effective thermal conductivity.

When considering the continuous wave laser sources, heat flow out of the laser irradiated volume has a significant effect on the predicted temperature rise. This has been illustrated by noting the gradual convergence of the calculated temperature rise to experimental data as the number of dimensions of the model was increased. As the film is very thin compared to the substrate, it is the thermal properties of the glass that dominate the interaction when long timescales are considered. To estimate what duration of interaction would need to be exceeded for this to be the case, the time required for heat flow to extend the heat affected zone by one beam radius can be considered. This was done with both the

substrate and the film parameters and found to be approximately 40 and 100 ms respectively. Consequently, more complex models are required for continuous wave laser heating and for predicting cumulative residual temperature rise from repetitively pulsed lasers. In the case of a single nanosecond pulse, heat flow during heating is minimal as the pulse length is of the order of 10^6 times shorter than the thermal diffusion time and all models converge to the same predicted peak temperature. Thus, rapid heating on poorly conducting substrates can be described by greatly simplified models.

An accurate description of the energy loading into the sample has been shown to be vital for both the pulsed and continuous wave models; both require knowledge of the incident laser energy and the optical parameters of the sample. However, the importance of the thermal parameters varies. For continuous wave irradiation of a thin film on a thick substrate, the 2D-axisyymetric model is insensitive to changes in the thermal parameters of the film over the timescales of interest (100's of milliseconds and longer), whereas the substrate parameters play a significant role. For the nanosecond pulsed laser models, the thermal properties of the film drastically affect the peak temperature rise whilst the substrate properties have very little effect. The substrate parameters are however still important during the cooling stage. This is also linked to how the heat flows out of the laser irradiated volume and the rates of heating associated with each laser system.

Within the continuous wave models, the rate of energy deposition is low and the heat that is generated diffuses throughout the sample whilst energy is being continuously deposited. On sub-millisecond timescales, this heat diffuses into the substrate and temperature gradients are setup which control the rate of conductive cooling. As the temperature begins to increase within the film, the

rates of convective and radiative cooling also increase. These cooling rates are all dictated by temperature gradients in various forms. The film reaches a steady state temperature once the temperature gradients have been established and the rate of cooling has reached equilibrium with the heating rate. At this point no further temperature rise is observed. For this reason, it is largely the cooling mechanisms which dictate the maximum temperature. This explains why the thermal parameters of the substrate affect the peak temperature because they control the conductive cooling rate. However, as the film is so thin, the effect that the film has on the maximum temperature is small and its thermal parameters are not so significant. It is important to consider that with higher power laser systems this could change because the rate of energy deposition can exceed the rates of the various cooling mechanisms and steady state conditions may not be reached so quickly.

In contrast, within the models of nanosecond pulsed irradiation, the rate of energy deposition is much larger and occurs over a very short duration. In this case, the heat that is generated within the film at the start of the laser pulse has not diffused into the substrate by the time the pulse has finished. Using the parameters of the ITO film, the thermal diffusion length over a duration of 15 ns is less than 60 nm. This means that all the heating occurs within a very confined volume in the film. Therefore, during the heating stage, there is no time for steady-state temperature gradients to be established and the rate of energy deposition far exceeds that of the cooling processes. Because of this, the thermal properties of the film play a large role in determining the temperature rise as all the energy is concentrated within this small volume located in the film. Only at longer times do the parameters of the substrate become important when the cooling begins to have a dominant effect.

There are still some areas that could be explored further. One of the issues that was observed was the disagreement between the magnitudes of the experimentally measured temperature rises and those predicted by the models. A challenge of the experimental setups used throughout this work was that the operating conditions for the IR camera measurements were not ideal. The temperature rises that were generated were only slightly above the ambient temperature meaning that the relative uncertainties of these measurements were quite large. Further, as only 9 of the 83200 pixels on the camera were being used to characterise the laser-induced temperature rise, due to the small heated spot size, any variations in the calibration of these pixels could have significantly perturbed the temperature readings. It would be interesting to investigate a larger area, higher power, beam to try and minimise many of these uncertainties and improve confidence in the experimentally measured temperature rises.

References

1. Ellmer, K. Past achievements and future challenges in the development of optically transparent electrodes. *Nat. Photonics* **6,** 809–817 (2012).

2. Exarhos, G. J. & Zhou, X.-D. Discovery-based design of transparent conducting oxide films. *Thin Solid Films* **515,** 7025–7052 (2007).

3. Ellmer, K. & Mientus, R. Carrier transport in polycrystalline transparent conductive oxides: A comparative study of zinc oxide and indium oxide. *Thin Solid Films* **516,** 4620–4627 (2008).

4. Duan, H., Wang, J., Liu, L., Huang, Q. & Li, J. Rethinking China's strategic mineral policy on indium: implication for the flat screens and photovoltaic industries. *Prog. PHOTOVOLTAICS Res. Appl.* **24,** 83–93 (2016).

5. Ylä-Mella, J. & Pongrácz, E. Drivers and Constraints of Critical Materials Recycling: The Case of Indium. *Resources* **5,** 34 (2016).

6. Hong, H. S., Jung, H. & Hong, S. J. Recycling of the indium scrap from ITO sputtering waste. *Res. Chem. Intermed.* **36,** 761–766 (2010).

7. Gillispie, M. a., van Hest, M. F. a. M., Dabney, M. S., Perkins, J. D. & Ginley, D. S. Sputtered Nb- and Ta-doped TiO2 transparent conducting oxide films on glass. *J. Mater. Res.* **22,** 2832–2837 (2007).

8. Dabney, M. S. *et al.* Pulsed laser deposited Nb doped TiO2 as a transparent conducting oxide. *Thin Solid Films* **516,** 4133–4138 (2008).

9. Furubayashi, Y. *et al.* A transparent metal: Nb-doped anatase TiO2. *Appl. Phys. Lett.* **86,** 252101 (2005).

10. Gopinadhan, K. *et al.* Effect of Nb and Ta Substitution on Donor Electron Transport and Ultrafast Carrier Dynamics in Anatase TiO2 Thin Films. *J. Mater. Chem. C* **3,** 6329–6333 (2015).

11. Gillispie, M. A., Van Hest, M. F. A. M., Dabney, M. S., Perkins, J. D. & Ginley, D. S. RF magnetron sputter deposition of transparent conducting Nb-doped TiO2 films on SrTiO3. *J. Appl. Phys.* **101,** 33125 (2007).

12. Zhang, S. X. *et al.* Niobium doped TiO2: Intrinsic transparent metallic anatase versus highly resistive rutile phase. *J. Appl. Phys.* **102,** 13701 (2007).

13. Yamada, N. *et al.* Fabrication of low resistivity Nb-doped TIO2 transparent conductive polycrystalline films on glass by reactive sputtering. *Japanese J. Appl. Physics, Part 1 Regul. Pap. Short Notes Rev. Pap.* **46,** 5275–5277 (2007).

14. Minami, T., Sato, H., Nanto, H. & Takata, S. Highly Conductive and Transparent Silicon Doped Zinc Oxide Thin Films Prepared by RF Magnetron Sputtering. *Jpn. J. Appl. Phys.* **25,** L776–L779 (1986).

15. Hirotoshi, S., Minami, T. & Takata, S. Highly transparent and conductive group IV impurity-doped ZnO thin films prepared by radio frequency magnetron sputtering. *J. Vac. Sci. Technol. A* **11,** 2975–2979 (1993).

16. Clatot, J., Nistor, M. & Rougier, A. Influence of Si concentration on electrical and optical properties of room temperature ZnO:Si thin films. *Thin Solid Films* **531,** 197–202 (2013).

17. Luo, J. T., Zhu, X. Y., Chen, G., Zeng, F. & Pan, F. The electrical, optical and magnetic properties of Si-doped ZnO films. *Appl. Surf. Sci.* **258,** 2177–2181 (2012).

18. Das, A. K., Misra, P. & Kukreja, L. M. Effect of Si doping on electrical and optical properties of ZnO thin films grown by sequential pulsed laser deposition. *J. Phys. D. Appl. Phys.* **42,** 165405 (2009).

19. Clatot, J. *et al.* Low temperature Si doped ZnO thin films for transparent conducting oxides. *Sol. Energy Mater. Sol. Cells* **95,** 2357–2362 (2011).

20. Rashidi, N. *et al.* Highly conducting and optically transparent Si-doped ZnO thin films prepared by spray pyrolysis. *J. Mater. Chem. C* **1,** 6960–6969 (2013).

21. Qin, H., Liu, H. F. & Yuan, Y. Z. Si doped ZnO thin films for transparent conducting oxides. *Surf. Eng.* **29,** 70–77 (2013).

22. Faghri, A., Zhang, Y. & Howell, J. *Advanced Heat and Mass Transfer*. (Global Digital Press, 2010).

23. Incropera, F. P., Dewitt, D. P., Bergman, T. L. & Lavine, A. S. *Fundamentals of Heat and Mass Transfer*. (John Wiley & Sons, 2006).

24. Bejan, A. *Heat Transfer*. (John Wiley & Sons, 1993).

25. Lienhard, J. H. I. & Lienhard, J. H. V. *A Heat Transfer Textbook*. (Plogiston Press, 2002).

26. COMSOL. Heat Transfer Module User's Guide 5.2a. 215–238 (2016).

27. Duley, W. W. *CO2 Lasers: Effects and Applications*. (Academic Press, 1976).

28. Von Allmen, M. & Blatter, A. *Laser-Beam Interactions with Materials*. (Springer, 1995).

29. Bäuerle, D. W. *Laser Processing and Chemistry*. (Springer, 1996).

30. Carslaw, H. & Jaeger, J. *Conduction of heat in solids*. (Clarendon Press, 1959).

31. Ready, J. F. *Effects of High-Power Laser Radiation*. (Academic Press, 1971).

32. Ready, J. F. Effects Due to Absorption of Laser Radiation. *J. Appl. Phys.* **36,** 462–468 (1965).

33. Bechtel, J. H. Heating of solid targets with laser pulses. *J. Appl. Phys.* **46,** 1585–1593 (1975).

34. Lax, M. Temperature rise induced by a laser beam. *J. Appl. Phys.* **48,** 3919–3924 (1977).

35. Lax, M. Temperature rise induced by a laser beam II. The nonlinear case. *Appl. Phys. Lett.* **33,** 786–788 (1978).

36. El-Adawi, M. K. & Shalaby, S. A. Laser heating of a two-layer system with temperature dependent front surface absorptance. *Vacuum* **46,** 37–42 (1995).

37. Burnett, D. S. *Finite Element Analysis: From Concepts to Applications*. (Addison Wesley, 1987).

38. Wait, R. & Mitchell, A. R. *Finite element analysis and applications*. (Wiley,

1985).

39. Szabo, B. A. & Babuska, I. *Finite element analysis*. (Wiley, 1991).

40. Fagan, M. J. *Finite element analysis: theory and practice*. (Pearson Education Limited, 1992).

41. COMSOL. COMSOL Multiphysics 5.2a. (2016).

42. SCHOTT. Schott Borofloat 33. 1–32 (2009).

43. Brewster, M. Q. *Thermal Radiative Transfer and Properties*. (John Wiley & Sons, 1992).

44. Ashida, T. *et al.* Thermal transport properties of polycrystalline tin-doped indium oxide films. *J. Appl. Phys.* **105,** 73709 (2009).

45. Pichanusakorn, P. & Bandaru, P. Nanostructured thermoelectrics. *Mater. Sci. Eng. R Reports* **67,** 19–63 (2010).

46. Minnich, A. J., Dresselhaus, M. S., Ren, Z. F. & Chen, G. Bulk nanostructured thermoelectric materials: current research and future prospects. *Energy Environ. Sci.* **2,** 466–479 (2009).

47. Al-dahoudi, N. Wet chemical deposition of transparent conducting coatings made of redispersable crystalline ITO nanoparticles on glass and polymeric substrates. (Saarland University, 2003).

48. Szörényi, T., Laude, L. D., Bertóti, I., Kántor, Z. & Geretovszky, Z. Excimer laser processing of indium-tin-oxide films: An optical investigation. *J. Appl. Phys.* **78,** 6211 (1995).

49. Harrison, P. M., Hay, N. & Hand, D. P. A study of stitch line formation during high speed laser patterning of thin film indium tin oxide transparent electrodes. *Appl. Surf. Sci.* **256,** 7276–7284 (2010).

50. Xiao, S. Picosecond Laser Ablation of Indium Tin Oxide Thin Film. (Ruhr University Bochum, 2012).

51. Cordfunke, E. H. P. & Westrum Jr, E. F. The Heat Capacity and Derived Thermophysical Properties of In2O3 from 0 to 1000K. *J. Phys. Chem. Solids* **53,** 361–365 (1992).

52. Swanepoel, R. Determination of the thickness and optical constants of amorphous silicon. *J. Phys. E.* **16,** 1214–1222 (1983).

53. Manifacier, J. C., Gasiot, J. & Fillard, J. P. A simple method for the determination of the optical constants n, k and the thickness of a weakly absorbing thin film. *J. Phys. E.* **9,** 1002–1004 (1976).

54. Laven, P. MiePlot. (2015).

55. Konig, T. A. *et al.* Electrically Tunable Plasmonic Behavior of Nanocube-Polymer Nanomaterials Induced by a Redox Active Electrochromic Polymer (Supporting Information). *ACS Nano* **8,** 6182–6192 (2014).

56. Polyanskiy, M. Refractive index of In2O3-SnO2 (Indium tin oxide, ITO) - Konig. Available at: https://refractiveindex.info/?shelf=other&book=In2O3-SnO2&page=Konig. (Accessed: 22nd June 2017)

57. Schneider, C. A., Rasband, W. S. & Eliceiri, K. W. NIH Image to ImageJ: 25 years of image analysis. *Nat Meth* **9,** 671–675 (2012).

58. Pietrak, K. & Winiewski, T. S. A review of models for effective thermal conductivity of composite materials. *J. Power Technol.* **95,** 14–24 (2015).

59. Guo, W., Lim, C. J., Bi, X., Sokhansanj, S. & Melin, S. Determination of effective thermal conductivity and specific heat capacity of wood pellets. *Fuel* **103,** 347–355 (2013).

60. Nield, D. A. & Bejan, A. *Convection in porous media*. (Springer, 2006).

61. Janssen, D. & Lohrengel, J. *Investigation and development of a method for the measurement of the emissivity of glass (EUR 13487)*. (1991).

Appendix A: Beer-Lambert absorption with multiple reflections

An expression was required for the intensity profile of light which was incident on a thin film on a substrate, surrounded by air. It was assumed that no light was absorbed in the air. First the intensity profile of the light through the film was considered, taking into account multiple reflections assuming a Beer-Lambert absorption of the form described by equation A1.

$$I(x) = I_0 \exp(-\alpha x) \tag{A1}$$

Figure A1 shows a schematic of the laser light that was considered to contribute towards the laser intensity within the sample and is intended to aid the reader to understand the following equations.

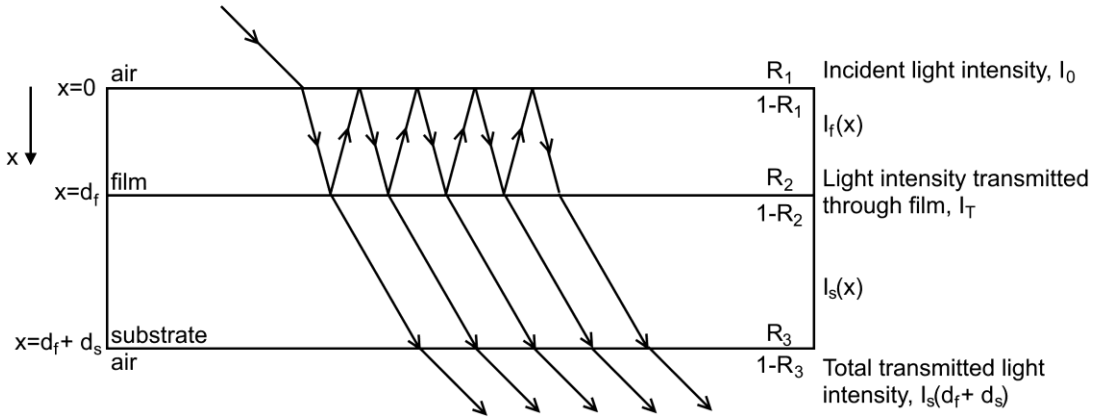

Figure A1 – Schematic showing the last light that was considered to contribute towards the overall laser intensity within the sample in the numerical simulations. Multiple reflections were considered within the thin film. Reflections from the substrate-air interface were not considered to contribute towards the intensity within the sample.

At each interface, the fraction of reflected light is given by R and the amount of transmitted light by *(1-R)*. By adding the contribution from each successive reflection within the film an equation with an infinite number of terms was reached; the first four terms are shown in equation A2. [See erratum at the end of Appendix A for correction of equations A2, A5-A7 and A9-A12.]

$$\begin{aligned} I_f(x) = {} & I_0(1-R_1)\exp(-\alpha_f\, x) + I_0(1-R_1)\exp(-\alpha_f\, d_f)R_2\exp(\alpha_f(x-2d_f)) \\ & + I_0(1-R_1)\exp(-\alpha_f\, d_f)R_2\exp(-\alpha_f 2d_f)R_1\exp(-\alpha_f x) \\ & + I_0(1-R_1)\exp(-\alpha_f\, d_f)R_2\exp(-\alpha_f 2d_f)R_1\exp(-\alpha_f d_f) \\ & R_2\exp(\alpha_f(x-2d_f)) + \ldots \end{aligned} \tag{A2}$$

This equation described the intensity of light within the film, negating any interference effects. It consists of an infinite number of terms but could be simplified by separating it into two geometric series and then calculating the sum to infinity for each series. A general geometric series is defined by equation A3.

$$a + ar + ar^2 + ar^3 \tag{A3}$$

For the first series in equation A2, a and r were given by equations A4 and A5.

$$a = I_0(1-R_1)\exp(-\alpha_f x) \tag{A4}$$

$$r = R_1R_2\exp(-3\alpha_f d_f) \tag{A5}$$

For the second series a and r were given by equations A6 and A7.

$$a = I_0(1-R_1)R_2\exp(\alpha_f(x-3d_f)) \tag{A6}$$

$$r = R_1R_2\exp(-3\alpha_f d_f) \tag{A7}$$

The sum to infinity of a geometric series is given by equation A8 for $|r|<1$.

$$S_\infty = \frac{a}{1-r} \tag{A8}$$

Combining and simplifying the sum to infinity of both geometric series leads to equation A9 which describes the overall intensity of light within the film neglecting interference effects.

$$I_f(x) = I_0 \frac{\exp(-\alpha_f x)(1-R_1)(\exp(3\alpha_f d_f) + R_2 \exp(2\alpha_f x)}{\exp(3\alpha_f d_f) + R_1 R_2} \tag{A9}$$

The amount of light transmitted through the film and into the substrate was calculated using the same procedure and is defined by equation A10.

$$\begin{aligned} I_T &= I_0(1-R_1)\exp(-\alpha_f d_f)(1-R_2) \\ &\quad + I_0(1-R_1)\exp(-\alpha_f d_f)R_2 \exp(-2\alpha_f d_f)R_1 \exp(-\alpha_f d_f)(1-R_2) + \ldots \end{aligned} \tag{A10}$$

The sum to infinity of this series leads to equation A11.

$$I_T = I_0 \frac{(1-R_1)(1-R_2)\exp(-\alpha_f d_f)}{1-R_1 R_2 \exp(-3\alpha_f d_f)} \tag{A11}$$

Now assuming a Beer-Lambert absorption within the substrate with no reflections or interference considered, the intensity profile through the substrate was given by equation A12.

$$I_s(x) = I_0 \frac{(1-R_1)(1-R_2)\exp(-\alpha_f d_f)}{1-R_1 R_2 \exp(-3\alpha_f d_f)} \exp(-\alpha_s (x - d_f)) \tag{A12}$$

By taking into account the transmittance through the final substrate-air interface, the total transmittance through the thin film and substrate was given by equation A13.

$$T = \frac{I_s(d_f + d_s)}{I_0}(1-R_3) \tag{A13}$$

Erratum:

Regrettably there was a mistake made during the derivation of equation A2 which was propagated into equations A5-A7, A9-A12 and equations 22, 24 and 52 in the main text. The corrected equations are listed below.

Equation A2, which describes the intensity of light within the thin film due to multiple reflections, is corrected as equation A14.

$$\begin{aligned} I_f(x) = {} & I_0(1-R_1)\exp(-\alpha_f x) + I_0(1-R_1)\exp(-\alpha_f d_f)R_2\exp(-\alpha_f(d_f - x)) \\ & + I_0(1-R_1)\exp(-\alpha_f d_f)R_2\exp(-\alpha_f d_f)R_1\exp(-\alpha_f x) \\ & + I_0(1-R_1)\exp(-\alpha_f d_f)R_2\exp(-\alpha_f d_f)R_1\exp(-\alpha_f d_f) \\ & R_2\exp(-\alpha_f(d_f - x)) + \ldots \end{aligned} \tag{A14}$$

Hence equations A5-A7 are also incorrect and the corrected forms are listed as equations A15-A17.

$$r = R_1 R_2 \exp(-2\alpha_f d_f) \tag{A15}$$

$$a = I_0(1-R_1)\exp(-\alpha_f d_f)R_2\exp(-\alpha_f(d_f - x)) \tag{A16}$$

$$r = R_1 R_2 \exp(-2\alpha_f d_f) \tag{A17}$$

Combining the sum to infinity of these geometric series leads to equation A18 which is the corrected version of equation A9. This describes the laser light intensity throughout the film considering multiple reflections.

$$\begin{aligned} I_f(x) &= I_0 \frac{(1-R_1)\exp(-\alpha_f x) + (1-R_1)\exp(-\alpha_f d_f)R_2\exp(-\alpha_f(d_f - x))}{1 - R_1 R_2 \exp(-2\alpha_f d_f)} \\ &= I_0 \frac{(1-R_1)(\exp(2\alpha_f d_f - \alpha_f x) + R_2\exp(\alpha_f x))}{\exp(2\alpha_f d_f) - R_1 R_2} \end{aligned} \tag{A18}$$

Similarly, there was a mistake in equation A10 with the corrected form being equation A19.

$$I_T = I_0(1-R_1)\exp(-\alpha_f d_f)(1-R_2) + I_0(1-R_1)\exp(-\alpha_f d_f)R_2\exp(-\alpha_f d_f)R_1\exp(-\alpha_f d_f)(1-R_2)+... \quad \text{(A19)}$$

The corrected sum to infinity of this series leads to equation A20 rather than A11.

$$I_T = I_0\frac{(1-R_1)(1-R_2)\exp(-\alpha_f d_f)}{1-R_1R_2\exp(-2\alpha_f d_f)} \quad \text{(A20)}$$

Hence the intensity profile through the substrate is given by equation A21 rather than A12.

$$I_s(x) = I_0\frac{(1-R_1)(1-R_2)\exp(-\alpha_f d_f)}{1-R_1R_2\exp(-2\alpha_f d_f)}\exp(-\alpha_s(x-d_f)) \quad \text{(A21)}$$

Because of this, equations 22, 24 and 52 in the main text should also be corrected. The corrected forms are listed as equations A22, A23 and A24 respectively.

$$I_f(z) = I_0\frac{(1-R_1)(\exp(2\alpha_f d_f - \alpha_f z) + R_2\exp(\alpha_f z))}{\exp(2\alpha_f d_f) - R_1R_2} \quad \text{(A22)}$$

$$I_s(z) = I_0\frac{(1-R_1)(1-R_2)\exp(-\alpha_f d_f)}{1-R_1R_2\exp(-2\alpha_f d_f)}\exp(-\alpha_s(z-d_f)) \quad \text{(A23)}$$

$$T = (1-R_3)\frac{(1-R_1)(1-R_2)\exp(-\alpha_f d_f)}{1-R_1R_2\exp(-2\alpha_f d_f)}\exp(-\alpha_s d_s) \quad \text{(A24)}$$

These errors have several implications throughout this work. The first issue is that the imaginary components of the refractive index of the Borofloat substrate and ITO film were calculated incorrectly due to the error in equation A11 and A13 (which was affected by the error in A12). However, when using the corrected equations, the values remain the same as those used in this work to 3 significant figures. Hence, the use of the incorrect equations had no impact on the validity of these values.

Additionally, in the numerical models the heat source throughout the film and substrate was incorrect. A plot of the original and corrected laser intensity

throughout the irradiated sample is shown in figures A2 and A3 for the HeCd and XeCl laser respectively. The percentage difference between the original equations, that were used throughout this work, and the corrected versions is also shown.

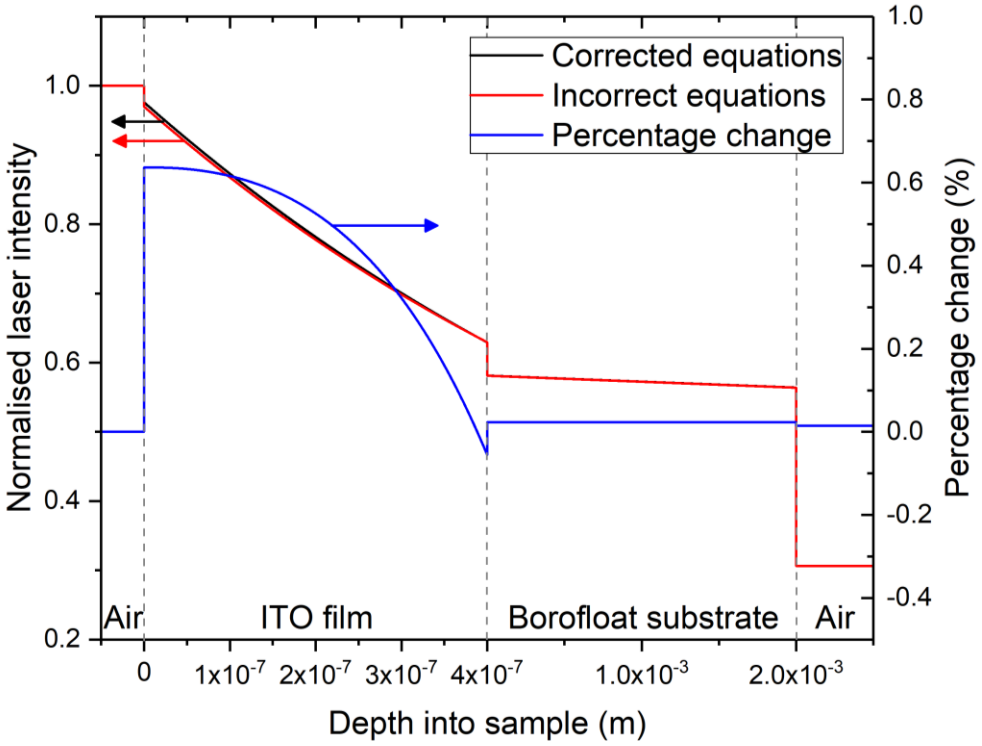

Figure A2 – Normalised laser intensity throughout the depth of the ITO coated Borofloat sample for HeCd laser. The incorrect equations are shown in red and the corrected versions shown in black. The percentage difference in the laser intensity throughout the sample depth is shown in blue and remains below 0.64% throughout the entire sample.

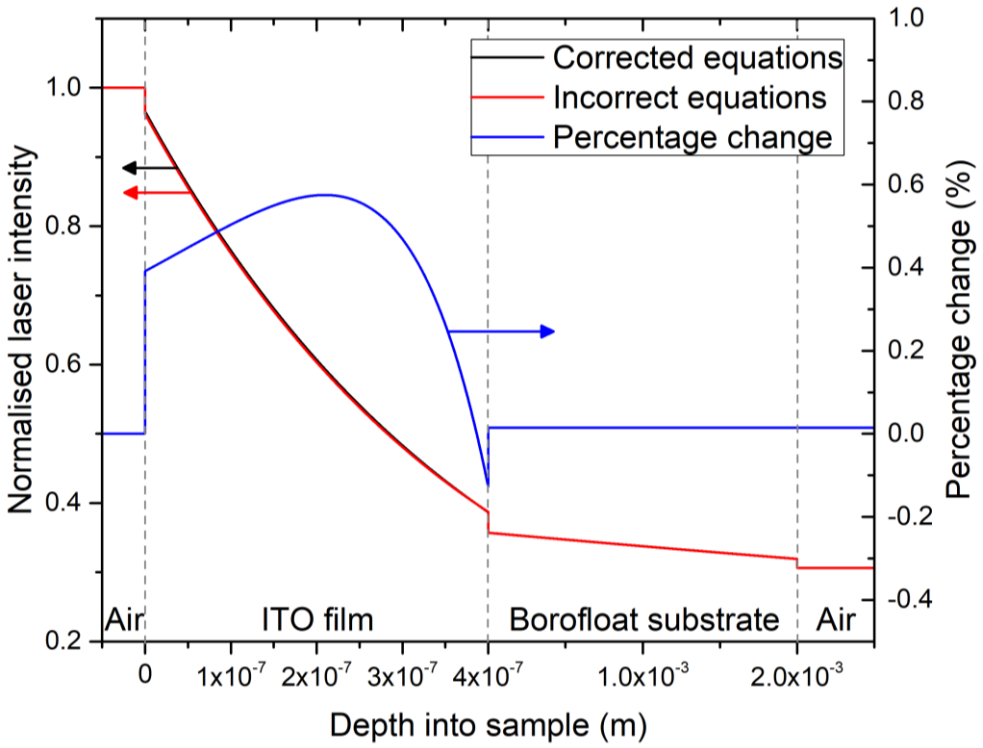

Figure A3 – Normalised laser intensity throughout the depth of the ITO coated Borofloat sample for XeCl laser. The incorrect equations are shown in red and the corrected versions shown in black. The percentage difference in the laser intensity throughout the sample depth is shown in blue and remains below 0.6% throughout the entire sample.

The magnitude of the percentage change in laser intensity is less than 0.64% across the whole sample for both the HeCd and XeCl lasers.

To calculate the percentage change in the energy deposited into the sample between the incorrect and corrected equations, the heat source can be integrated over the irradiated volume. Based on equation 27, the heat source can be represented as a combination of several terms. This equation is reformulated in equation A25 below with the I_0 term separated from the $h(z)$ term to aid this explanation.

$$Q = I_0\,\alpha(z)\,f(x,y)\,g(t)\,h(z) \qquad \text{(A25)}$$

As the absorption coefficients of the film and substrate were not affected by the previously discussed errors, $\alpha(z)$, $f(x,y)$ and $g(t)$ are the same in the incorrect and

corrected heat sources. Hence, the percentage difference in energy deposited is equal to the percentage difference in the integral of $h(z)$ over the sample depth of interest. In this case, $h(z)$ is described by equation A9 or A18 in the film and equation A12 or A21 in the substrate for the incorrect and corrected equations respectively.

These percentage differences were calculated individually for the film and substrate for each laser system. It was found that there is a 0.46% increase in the amount of energy deposited into the film and a 0.015% increase in energy deposited into the substrate during irradiation with the XeCl laser when using the corrected equations. In the case of the HeCd laser, the corrected equations result in a 0.47% increase in the energy deposited into the film and a 0.023% increase in energy deposited into the substrate.

In summary, the errors made during the derivation of the equations listed above (i) did not affect the calculated absorption coefficients, (ii) only had a very small effect on the energy distribution (<0.64% difference across whole sample in all cases) and (iii) resulted in a difference in the energy deposited of less than 0.5% for the film and less than 0.025% for the substrate for all cases. Hence, whilst these mistakes are acknowledged, it has been determined that the impact of these mistakes on the results presented within this work are likely to be minimal. The use of the corrected equations is not expected to alter any of the conclusions made within this work and it has therefore been decided that it is not necessary to recalculate the results from the models.